



**UNIVERSITY** *of the*  
**WESTERN CAPE**

---

**AN HI STUDY OF THE NEARBY DWARF GALAXY**  
**IC 4710**

---

**Getrude Thando Mothogoane**

Supervisors: Dr. E. Elson and Dr. M. Glowacki

**Faculty of Natural Sciences**

Department of Physics and Astronomy

A thesis submitted for the Masters degree of  
Astrophysics

December 2021

<http://etd.uwc.ac.za/>

## Declaration

I, **Getrude Thando Mothogoane**, declare that, '**An HI study of the nearby dwarf galaxy IC 4710**' is my own work, that it has not been submitted before for any degree or assessment in any other University, and that all the sources I have used or quoted have been indicated and acknowledged by means of complete references.



UNIVERSITY *of the*  
WESTERN CAPE

## Acknowledgements

I want to start by thanking the Center for Radio Cosmology (CRC) for funding my work. I would also like to deeply express my special thanks to my supervisor Dr. E. Elson. When we started working together, I was faced with a personal situation that could have led me to dragging my feet or even dropping out. Still, I made it through because of his patience and support, and he made me believe that hard work and determination are the important elements for achievement. Although the journey was not easy, he managed to make it exciting and informative, and I am grateful for that. To my co-supervisor Dr. M. Glowacki, thank you for responding to my hundreds of skype messages on a daily basis and helping me out whenever I needed you. You really helped me a lot with data analysis, problem-solving, and breaking down complex problems for me to understand; I will forever be grateful for your patience. Both my supervisors always made constructive comment suggestions on my thesis, which inspired me to improve the quality of the thesis.

Thank you to the Department of Physics and Astronomy for the weekly research meetings and the journal club meetings, they were helpful, and I have learned a lot from them. I would also like to thank Xola Ndaliso, Narusha Isaacs, and Malebo Moloko for always being there when I needed their help; I appreciate your efforts. Xola, thank you for explaining the project in simple terms for me to understand. To my peers, thank you for cheering me up when I needed to laugh. How can I forget my beautiful family? Thank you for your support and motivation; you made me push even on my lazy days because I did not want to let you down. Lastly, to my husband and son, thank you for keeping my sanity throughout; thanks for the love and prayers; you contributed a lot to this research work.

# Table of Contents

<b>Declaration</b>	<b>i</b>
<b>Acknowledgements</b>	<b>ii</b>
<b>List of figures</b>	<b>vii</b>
<b>List of tables</b>	<b>viii</b>
<b>Abstract</b>	<b>x</b>
<b>Chapter 1</b>	<b>1</b>
<b>1 Introduction</b>	<b>1</b>
1.1 Galaxies . . . . .	1
1.2 Dwarf galaxies . . . . .	3
1.3 Dark matter . . . . .	5
1.4 Rotation curves . . . . .	6
1.5 IC 4710 . . . . .	10
1.6 Thesis outline . . . . .	13
<b>Chapter 2</b>	<b>14</b>
<b>2 HI imaging of IC 4710</b>	<b>14</b>
2.1 Channel maps . . . . .	14
2.2 Distribution of noise in a line-free channel . . . . .	16
2.3 HI total intensity map . . . . .	17
2.4 HI intensity-weighted-mean velocity field map . . . . .	20
2.5 Velocity dispersion map . . . . .	22
2.6 HI global profile . . . . .	24
2.7 Mass estimates . . . . .	26
2.8 Mass-size and baryonic Tully-Fisher relations . . . . .	27
<b>Chapter 3</b>	<b>31</b>

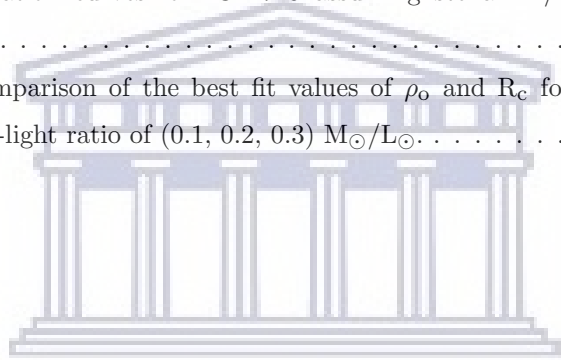
<b>3 Energetics of the neutral interstellar medium</b>	<b>31</b>
3.1 The role that HI plays in star formation . . . . .	31
3.2 Galactic fountain scheme . . . . .	32
3.2.1 Gas outflows in dwarf galaxies . . . . .	33
3.3 The central depression of HI in IC 4710 . . . . .	36
3.4 Escape velocity . . . . .	40
 <b>Chapter 4</b>	 <b>42</b>
<b>4 Dynamical modeling</b>	<b>42</b>
4.1 Tilted ring model . . . . .	42
4.2 <sup>3D</sup> BAROLO . . . . .	44
4.2.1 High resolution data . . . . .	47
4.2.2 Mid-low resolution data . . . . .	50
4.2.3 Very low resolution data . . . . .	51
4.3 Fitting procedure for IC 4710 . . . . .	54
4.4 Rotation curve . . . . .	63
4.5 Model and data comparison . . . . .	63
4.6 Asymmetric drift correction . . . . .	72
4.7 Mass modeling . . . . .	74
4.7.1 Gas distribution . . . . .	75
4.7.2 Stellar distribution . . . . .	79
4.7.3 Dark matter distribution . . . . .	83
4.8 Mass models . . . . .	84
4.9 Comparison to literature . . . . .	92
 <b>Chapter 5</b>	 <b>94</b>
 <b>Summary</b>	 <b>94</b>
 <b>Conclusion</b>	 <b>100</b>

## List of Figures

1	A Hubble Tuning fork diagram showing the morphological classification of galaxies (Kormendy et al., 1996). . . . .	2
2	Comparison between spiral galaxies and irregular galaxies (Roberts et al., 1969). . . . .	2
3	The HI rotation curve of a spiral galaxy UGC 5721 from Kamada et al. (2017). . . . .	8
4	The HI rotation curve of a dwarf galaxy DDO 154 from Iorio et al. (2016). . . . .	9
5	Various images of IC 4710 in different bands derived by Daigle et al. (2006) . . . . .	12
6	HI channel maps of IC 4710 based on the ATCA data cube. . . . .	15
7	The distribution of noise in a line-free channel of IC 4710 ATCA data cube. . . . .	16
8	The HI total intensity map obtained from the masked ATCA data cube of IC 4710. . . . .	18
9	Infrared image of IC 4710 produced from <i>Spitzer</i> 3.6 $\mu\text{m}$ imaging. . . . .	19
10	The HI intensity-weighted-mean velocity field map obtained from masked ATCA data cube. . . . .	21
11	The velocity dispersion map obtained from the masked ATCA data cube. . . . .	23
12	The HI global profile of IC 4710 based on the ATCA data cube. . . . .	25
13	HI mass-size relation. . . . .	28
14	Baryonic Tully-Fisher relation. . . . .	30
15	The galactic fountain scenario from Spitoni (2010). . . . .	34
16	The HI total intensity map obtained from the masked ATCA data cube of IC 4710. . . . .	36
17	B-band image of IC 4710, with HI contours overlaid. . . . .	39
18	The flowchart taken from Teodoro et al. (2015) which shows how $^3\text{D}$ Barolo operates. . . . .	46

19	The channel maps from <a href="#">Teodoro et al. (2015)</a> . . . . .	49
20	The parameters determined by <sup>3D</sup> BAROLO with the input data cube of galaxy NGC 5055 from the THINGS survey. . . . .	50
21	Rotation curves of the 30 dwarf late-type galaxies selected from the WHISP sample. . . . .	53
22	Results for the first iteration from <sup>3D</sup> BAROLO. . . . .	57
23	Results for the second iteration from <sup>3D</sup> BAROLO. . . . .	58
24	[Results for the third iteration from <sup>3D</sup> BAROLO. . . . .	59
25	Results for the fourth iteration from <sup>3D</sup> BAROLO. . . . .	60
26	Results for the fifth iteration from <sup>3D</sup> BAROLO. . . . .	61
27	Results for the sixth iteration from <sup>3D</sup> BAROLO. . . . .	62
28	Model channel maps from <sup>3D</sup> BAROLO. . . . .	64
29	Model-data comparison . . . . .	66
30	Fig. 28 continued. . . . .	67
31	Fig. 28 continued. . . . .	67
32	Fig. 28 continued. . . . .	68
33	Fig. 28 continued. . . . .	68
34	Fig. 28 continued. . . . .	69
35	Fig. 28 continued. . . . .	69
36	Fig. 28 continued. . . . .	70
37	A plot of standard deviation of the residuals obtained from subtracting the <sup>3D</sup> BAROLO model from ATCA cube. . . . .	71
38	Comparison between the observed rotation curve from <sup>3D</sup> BAROLO and the derived circular velocities . . . . .	74
39	The azimuthally-averaged HI surface density as a function of radius. . . . .	76
40	The HI cumulative mass curve of IC 4710 derived from the HI surface densities. . . . .	76
41	The rotation velocities of HI components in IC 4710. . . . .	77
42	The gas surface density profile (left) and the gas rotation curve(right) of dwarf galaxy CVnIdwA from LITTLE THINGS derived by <a href="#">Oh et al. (2015)</a> . . . . .	78

43	The stellar surface density profiles of IC 4710. . . . .	80
44	The cumulative stellar mass curves of IC 4710. . . . .	81
45	The stellar rotation curves of IC 4710. . . . .	82
46	The pseudo isothermal sphere density profiles of IC 4710. . . . .	86
47	The rotation curves for IC 4710 assuming stellar $M/L = 0.1$ $M_{\odot}/L_{\odot}$ . . . . .	87
48	The rotation curves for IC 4710 assuming stellar $M/L = 0.2$ $M_{\odot}/L_{\odot}$ . . . . .	88
49	The rotation curves for IC 4710 assuming stellar $M/L = 0.3$ $M_{\odot}/L_{\odot}$ . . . . .	89
50	The comparison of the best fit values of $\rho_0$ and $R_c$ for stellar mass-to-light ratio of (0.1, 0.2, 0.3) $M_{\odot}/L_{\odot}$ . . . . .	93



UNIVERSITY *of the*  
WESTERN CAPE



## List of Tables

1	Initial <sup>3D</sup> BAROLO parameters for IC 4710. . . . .	56
2	Parameters of dark matter in IC 4710. . . . .	85



UNIVERSITY *of the*  
WESTERN CAPE

I dedicate this thesis to my late parents Leah Mthogoane and Elias  
Mthogoane.



UNIVERSITY *of the*  
WESTERN CAPE

## Abstract

This work aims to study the dark matter content of the nearby (7.38 Mpc) dwarf galaxy IC 4710 using the HI line observations from the Australia Telescope Compact Array (ATCA). We produce the first interferometric maps of the galaxy HI distribution and dynamics and use these maps to measure important quantities such as total HI mass, velocity width, and size. We create a dynamical model of the galaxy using a three-dimensional modeling technique. The rotation curve was obtained by fitting a 3D tilted ring model to the HI data cube of galaxy IC 4710. The dynamical modeling of IC 4710 is being done for the first time. We compare the model to the data cube to check for accuracy and found that they are in good agreement; this shows that the results are reliable. The obtained rotation curve is rising steeply until it reaches the maximum rotation velocity of  $24.6 \text{ km s}^{-1}$  at a radius of 100 arcsec. To calculate the contribution of HI to the observed rotation curve, we used azimuthally-averaged gas surface densities from <sup>3D</sup>BAROLO to derive the gas rotation velocities. To quantify the gravitational contribution of stars to the measured rotation curve of IC 4710, we adopted the far-infrared luminosity ( $L_* = 10^{8.16} L_{\odot}$ ) of IC 4710 and assumed three stellar mass-to-light ratios to derive the stellar rotation velocities. We used a pseudo-isothermal sphere (ISO) to model the dark matter halo mass distribution. This model produced a good fit for the observed rotation curve of IC 4710. The mass model results show that IC 4710 does not have its total potential dominated by dark matter. Rather, roughly equal contributions are made by the baryons and the dark matter. The ISO parameters ( $\rho_0$  and  $r_c$ ) of IC 4710 were compared to literature results, and the parameters of IC 4710 fall within the range of the results obtained for other galaxies.

# Chapter 1

## 1 Introduction

### 1.1 Galaxies

A galaxy is a celestial object in the Universe made up of dust, gas, and stars, bound together by gravity. There are different kinds of galaxies classified in terms of their morphology in the Universe (Hubble et al., 1926), such as spiral galaxies (dynamical mass  $\sim 10^{11} M_{\odot}$ ; Rubin et al., 1978; Al-Baidhany et al., 2020), irregular galaxies (dynamical mass  $\sim 10^8$  to  $10^{10} M_{\odot}$ ; Gallagher et al., 1984), dwarf galaxies (dynamical mass  $\sim 10^8$  to  $10^9 M_{\odot}$ ; Oh et al., 2015), etc. Most galaxies have a size ranging from a few kpc to a few tens of kpc (Henry et al., 1998). Galaxies can interact with each other and merge to form larger galaxies, a process known as hierarchical growth. There are different types of galaxies classified in terms of their morphology, as presented in Fig. 1 (Hubble et al., 1926). Hubble et al. (1926) grouped galaxies as ellipticals and spirals and sorted them as early and late types based on the central bulge size and the structure of spiral arms they have. Hubble then split the spiral galaxies into barred (SB) and unbarred (S) galaxies. These two classes of galaxies are occupied mostly ( $\sim 90\%$ ) by luminous galaxies ( $> 10^5 L_{\odot}$ ) (Abraham et al., 2001). Less luminous galaxies ( $< 10^5 L_{\odot}$ ) are called dwarf galaxies. Abraham et al. (2001) mentioned that dwarf galaxies are not included in the Hubble sequence; these dwarf galaxies are more numerous than the luminous galaxies explained by the Hubble sequence. However, the contribution of dwarf galaxies to the total mass content in the galaxy population is less than the luminous galaxies. Roberts et al. (1969) made some comparisons between spiral galaxies and irregular galaxies in terms of their total masses and luminosities, and found that the mass and luminosity of irregular galaxies are less than spiral galaxies by 1 magnitude (presented in Fig. 2).

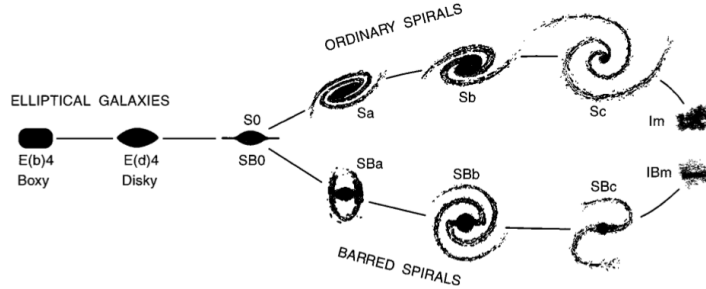


Figure 1: A Hubble Tuning fork diagram showing the morphological classification of galaxies (Kormendy et al., 1996). Elliptical galaxies presented on the left side, followed by lenticulars (SO), barred spirals presented at the bottom right side, unbarred spirals shown at the top right side, and irregulars presented as Im and IBm at the far end.

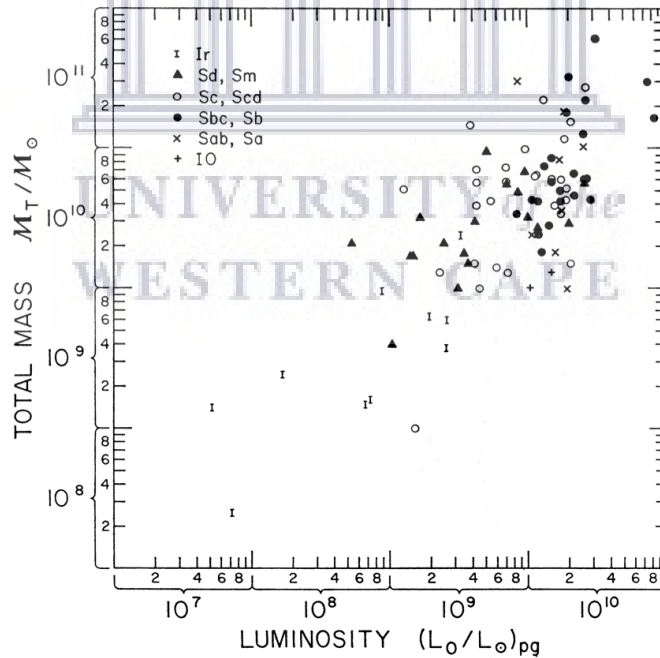


Figure 2: Comparison between spiral galaxies (shapes and crosses) and irregular galaxies ('I' symbols) in terms of their total mass and luminosity (Roberts et al., 1969).

## 1.2 Dwarf galaxies

Dwarf galaxies have smaller sizes (diameter  $< 3$  kpc; Gerola et al., 1980), smaller absolute magnitude (around -15 mag; Hodge et al., 1971), and lower surface brightness ( $\gtrsim 1$  mag arcsec $^{-2}$  fainter than luminous galaxies; De Blok et al., 2001). Dwarf galaxies exist in large quantities in the Universe (Mateo et al., 1998). The exact number could not be found as most literature mentions that they dominate, but they do not quantify their statements. Still, it is difficult to detect them due to their low surface brightness, smaller size, and smaller mass. Dwarf galaxies are grouped into three different types: dwarf elliptical galaxies, dwarf spheroidal galaxies, and dwarf irregular galaxies (Mateo et al., 1998). De Blok et al. (2001) mentioned that dwarf galaxies have not fully evolved and are dominated by dark matter. Since they have low surface brightness, it implies that they have low stellar density, making the baryonic contribution less than other galaxy types. They further mentioned that dark matter is the major contributor to the dynamics of dwarf galaxies (Iorio et al., 2016).

Low mass dwarf galaxies are cosmologically important since they help in studying or solving the cusp/core problem (Oh et al., 2015). The cusp/core problem is the variation of dark matter distributions at the innermost radii of galaxies (Oh et al., 2008). Dark matter and baryons in dwarf galaxies can interact through gas outflows to form new dwarf galaxies with no bulge. They can flatten the central cusps from dark matter only Cold Dark Matter (CDM) cosmological constant ( $\Lambda$ CDM) simulations. Low mass dwarf galaxies are cosmologically important because if there is the presence of cusps at the centre, it means that there is CDM in the Universe (Oh et al., 2015).

Nearby ( $< 11$  Mpc) late-type dwarf galaxies with no presence of bulge and spiral features are used to describe dark matter distributions at the centre of galaxies because dark matter is usually dominant in them (Oh et al., 2015). Their dark matter distributions can easily be derived. Recently some high-

resolution ( $\sim 6''$ ; [Oh et al., 2015](#)) HI surveys of nearby galaxies that use radio interferometers such as The HI Nearby Galaxy Survey (THINGS; [De Blok et al., 2008](#)), Local Irregulars That Trace Luminosity Extremes THINGS (LITTLE THINGS; [Oh et al., 2015](#)), etc., allow for derivation of HI rotation curves of galaxies. From these rotation curves, the central mass distributions can be derived. Dwarf galaxies with no presence of a bulge and spiral features help in reducing uncertainties originating from the decomposition of rotation curves into baryonic and non-baryonic matter ([Oh et al., 2015](#)).

Dwarf galaxies are usually found to be satellites to larger galaxies ([Geha et al., 2006](#)). [Carignan et al. \(1997\)](#) discovered eight dwarf galaxies that are orbiting the large lenticular galaxy NGC 5084. [Ibata et al. \(2013\)](#) found thirteen dwarf galaxies that are orbiting a large spiral Andromeda (M31) galaxy. A satellite galaxy and a large galaxy can interact and merge and result in the increase of the bulge of a larger galaxy ([Gutiérrez et al., 2002](#)).

There are different types of dwarf galaxies, and the difference is based on morphology. Examples of these dwarf galaxies are dwarf spheroidal (dSph), dwarf early-type (dE), blue compact dwarf galaxies (BCDs), dwarf irregulars (dIrs), etc. The dSph and the dE are located in groups and clusters; they are referred to as the oldest dwarf galaxies. The BCDs and dIrs are located in environments that are less dense and have continuous star formation ([Paudel et al., 2018](#)). Local Group (LG) dwarf galaxies are the most studied dwarf galaxies. The focus is usually on understanding the formation and evolution of these galaxies. The LG is a dense environment where interactions between galaxies are likely to happen ([Weisz et al., 2011](#)). Various studies show that while dSph galaxies have evolved from dIrs galaxies whose gas has been lost, dSph galaxies are a member of the dE family of galaxies ([Lin et al., 1983](#); [Grebel, 2001](#)).

### 1.3 Dark matter

Dark matter is cosmologically important because it plays a significant role in the formation and evolution of galaxies and also in shaping the large-scale structure in the Universe (Oh et al., 2015). De Blok et al. (2010) referred to dark matter as the major ingredient of the Universe. Studies have shown the dominant mass components of the Universe to be CDM and dark energy (in the form of a Cosmological Constant,  $\Lambda$ ; De Blok et al., 2008). Particles in  $\Lambda$ CDM are non-baryonic, and they interact with baryons through gravitational forces; again, they are collisionless and undetectable. The  $\Lambda$ CDM model of the Universe offers better explanations of large-scale observations than it does at smaller scales (such as galaxies) that are dominated by gravitation (De Blok et al., 2008).

Simulations and observations differ in dark matter distributions around the centre of galaxies. Simulations predict a cusp-like dark matter distribution around the centre of galaxies (Navarro et al., 1996; Moore et al., 1994). In contrast, dark matter distribution in nearby dwarf galaxies shows that the velocity increases linearly around the centre of galaxies, resulting in a constant density core (Oh et al., 2015; Gnedin et al., 2002). The discrepancy is referred to as the cusp or core problem, which is the small scale crisis (Oh et al., 2015). De Blok et al. (2010) mentioned that cosmological interactions between dark matter and baryons have the potential of solving the cusp-core problem.

Dark matter distributions can be studied using different models such as Navarro-Frank-White (NFW; Navarro et al., 1996) and the pseudo-isothermal (ISO; Begeman et al., 1991) halo. The NFW model was determined from the CDM simulations. A cuspy density dominates these simulations, and the universal density profile describes them. This universal density profile is mostly used in accounting for dark matter distributions that show a steep rise towards the central halo region. The distributions are described by  $\rho \sim R^\alpha$ , where  $\alpha \propto -1$ . The ISO halo model contains the constant density at the core of the galaxy (Oh et al., 2008). The distributions are described by  $\rho \sim R^\alpha$ , where  $\alpha \propto 0$ .



Baryonic contribution to the mass budget is less dominant in dwarf galaxies, and this is due to fewer stars. Dwarf galaxies, therefore, serve as useful laboratories to study the distribution of DM. Their central gravitational potential is not dominated by stellar gravity; this makes the gas the biggest contributor to the baryons. [De Blok et al. \(2008\)](#) aimed to derive the rotation curves and mass models of the THINGS galaxies, and from their study, they found their dwarf galaxies to be dominated by dark matter. [Elson et al. \(2011a\)](#) studied the HI kinematics of dwarf galaxy NGC 2915, and they discovered that their galaxy is dominated by dark matter. In latter years, [Simon \(2019\)](#) studied the dwarf galaxies from the Sloan Digital Sky Survey and found that they are dark matter dominated.

#### 1.4 Rotation curves

The distributions of mass within a galaxy determines the manner in which it rotates. If the main mass contributor is luminous, then the shape of the rotation curve will more closely trace the distribution of luminous matter ([Swaters et al., 2009](#)). The connection between dark matter and luminous matter is significant to study since it gives a clear understanding of galaxy formation history. There are many studies done to understand how the luminous components in galaxies and the rotation curves are linked ([Catinella et al. \(2006\)](#), [Roberts et al. \(1994\)](#)). These studies focused mainly on spiral galaxies, but recent studies are focusing on dwarf galaxies. They mainly wanted to understand the shape of rotation curves of galaxies at smaller radii because central regions give a good understanding of galaxy formation in a  $\Lambda$ CDM Universe. These early studies were based on the  $H\alpha$  emission line, which is only detected in the optical disk, but more recent studies use the HI emission-line which extends to greater distances than the optical disk, of greater importance in dwarf galaxies lacking stellar content compared to larger galaxies ([Swaters et al., 2009](#)).

In most cases, a tilted ring model is fitted to the velocity field to obtain the rotation curves (Begeman et al., 1989). This technique breaks the disk of the galaxy into concentric rings and models each one based on its own set of defining parameters (De Blok et al., 2008). A newly developed tilted ring modeling package is <sup>3D</sup>BAROLO (Teodoro et al., 2015). <sup>3D</sup>BAROLO is a code that generates rotation curves from using emission line data cubes as an input. Previously 2D algorithms such as ROTCUR were used, but were affected by factors such as beam smearing, while with <sup>3D</sup>BAROLO, that is not the case (Teodoro et al., 2015).

Some studies have focused on understanding the connection between the rotation curve shapes of galaxies and their luminous mass distributions (Swaters et al., 2009). Rotation curves are different for each type of galaxies; for example, the rotation curves of dwarf galaxies differ from the rotation curves of spiral galaxies. Previous studies have confirmed that rotation curves of dwarf galaxies have low amplitude, and they rise slowly up to the outermost radii. In comparison, the rotation curves of the spiral galaxies rise steeply at the innermost radii and become flat at the outermost radii (Swaters et al., 2009).

Kamada et al. (2017) modeled the HI rotation curve of a spiral galaxy UGC 5721, presented in Fig. 3. There is an increase in rotation velocity at smaller radii, and the rotation curve becomes flat at larger radii ( $\sim 3$  kpc). Iorio et al. (2016) studied the HI kinematics of 17 galaxies from LITTLE THINGS, with DDO 154 being one of the galaxies in a sample. The HI rotation curve of a dwarf galaxy DDO 154 is presented in Fig. 4, which shows that its rotational velocity constantly increases from small radii to higher radii.

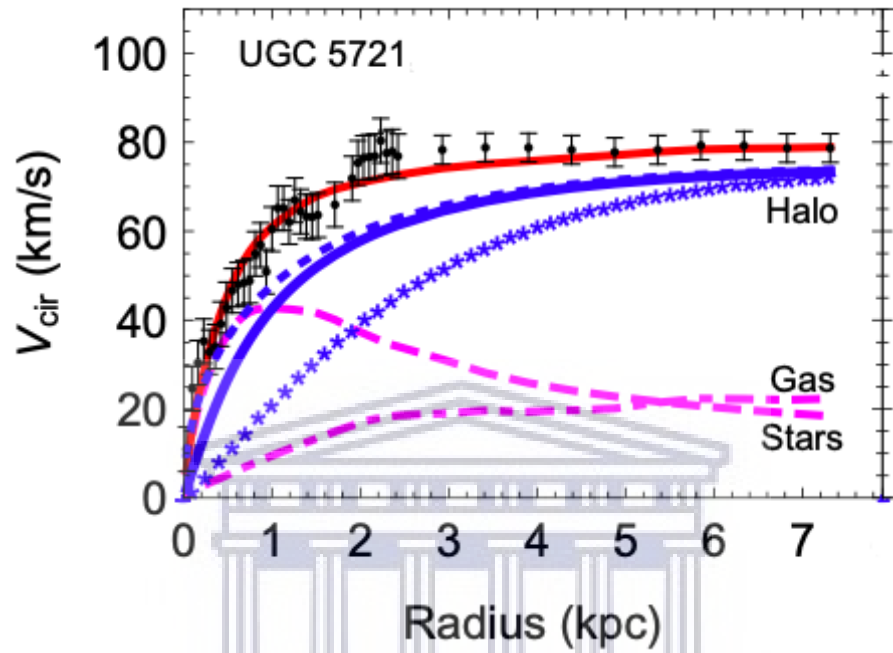


Figure 3: The HI rotation curve of a spiral galaxy UGC 5721 from Kamada et al. (2017). The black dots represent the observed rotation curve, and the solid red line represents the mass modelling fits from different components. The magenta dashed and dotted dashed lines represent the contribution of the star and gas to the rotation curve, respectively. The solid blue curve is the dark matter contributions, the blue dashes represent the corresponding CDM halo, and the blue asterisks represent the observed rotation curve when baryons are neglected.

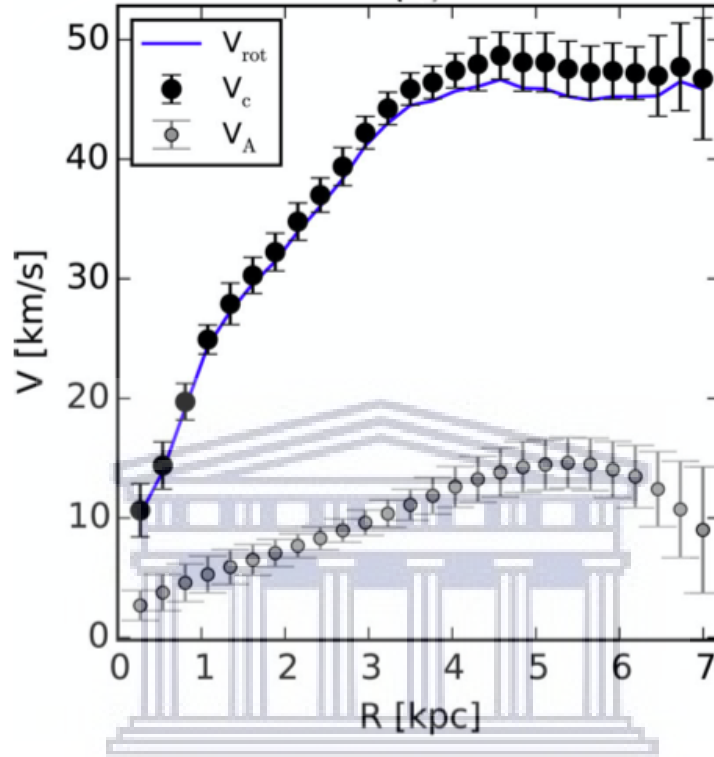


Figure 4: The HI rotation curve of a dwarf galaxy DDO 154 from [Iorio et al. \(2016\)](#). The blue curve ( $V_{rot}$ ) represent the rotation velocity from  $3^D$ BAROLO, the grey circles ( $V_A$ ) represent the asymmetric-drift correction, and the black circles ( $V_c$ ) represents the final corrected circular velocity.

Evidence that there is dark matter in galaxies comes from their rotation curves. This dark matter was also referred to as the “missing” matter, and it has now become an important and exciting cosmological study. In most cases, velocity fields are used to derive rotation curves because they provide accurate details of the dynamics of galaxies ([De Blok et al., 2008](#)). Previous studies revealed that most matter in the Universe is dark matter, while only  $\sim 5\%$  of the Universe is known to be made of baryonic content ([Chavanis et al., 2012](#)).

## 1.5 IC 4710

IC 4710 is a barred spiral dwarf galaxy that has a Hubble classification of SB(s)m and is dominated by a bar (Daigle et al., 2006; Peng et al., 2010, ;). Galaxy IC 4710 is located in the Pavo constellation, which is in the southern hemisphere. The right ascension of this galaxy is  $18^{\text{h}}28^{\text{m}}38^{\text{s}}$  and declination is  $-66^{\circ} 58' 54''$  (Ryder et al., 1993). The absolute magnitude of IC 4710 in the B-band is  $M_{\text{B}} = -18$  mag (Moustakas et al., 2010).

IC 4710 is found in a field packed with galaxies similar to IC 4710, and that makes it difficult for it to be identified (Ryder et al., 1993). Karachentsev et al. (2020) mentioned that IC 4710 is a satellite galaxy of a spiral galaxy NGC 6744, which is a southern Sb galaxy. It contains several HII regions. Ryder et al. (1993) mentioned that IC 4710 is almost similar to the Large Magellanic Cloud; they are both dominated by a bar. The HII regions are found on the bar, and the star-forming regions are found at the outer regions of the galaxy (Ryder et al., 1993).

Moustakas et al. (2010) used optical (3600 - 6900 Å) emission line to classify galaxies and found galaxy IC 4710 to be a star forming galaxy. Calzetti et al. (2010) used the *Spitzer* data of 189 nearby star forming galaxies, with galaxy IC 4710 being one of the studied galaxies. The study found that IC 4710 is a star forming dwarf galaxy with mean star formation rate surface density of  $10^{-2.823} M_{\odot} \text{ year}^{-1} \text{ kpc}^{-2}$  (Calzetti et al., 2010). Ryder et al. (1994) used the H $\alpha$  emission line and found IC 4710 to have the total star formation rate of  $1.3 M_{\odot} \text{ year}^{-1}$ .

Daigle et al. (2006) studied the H $\alpha$  kinematics of the Spitzer Infrared Nearby Galaxies Survey (SINGS) galaxies, with IC 4710 being one of the galaxies. They observed the galaxies using three telescopes. They used a 2D algorithm ROTCUR to fit the tilted ring model to the data to obtain the kinematical parameters. They obtained a positional angle of 5 degrees and an inclination

angle of 39 degrees for IC 4710. From their analysis, they found this galaxy to be dominated by HII. Figure 5 presents different images derived by [Daigle et al. \(2006\)](#) in different bands, and the velocity field.



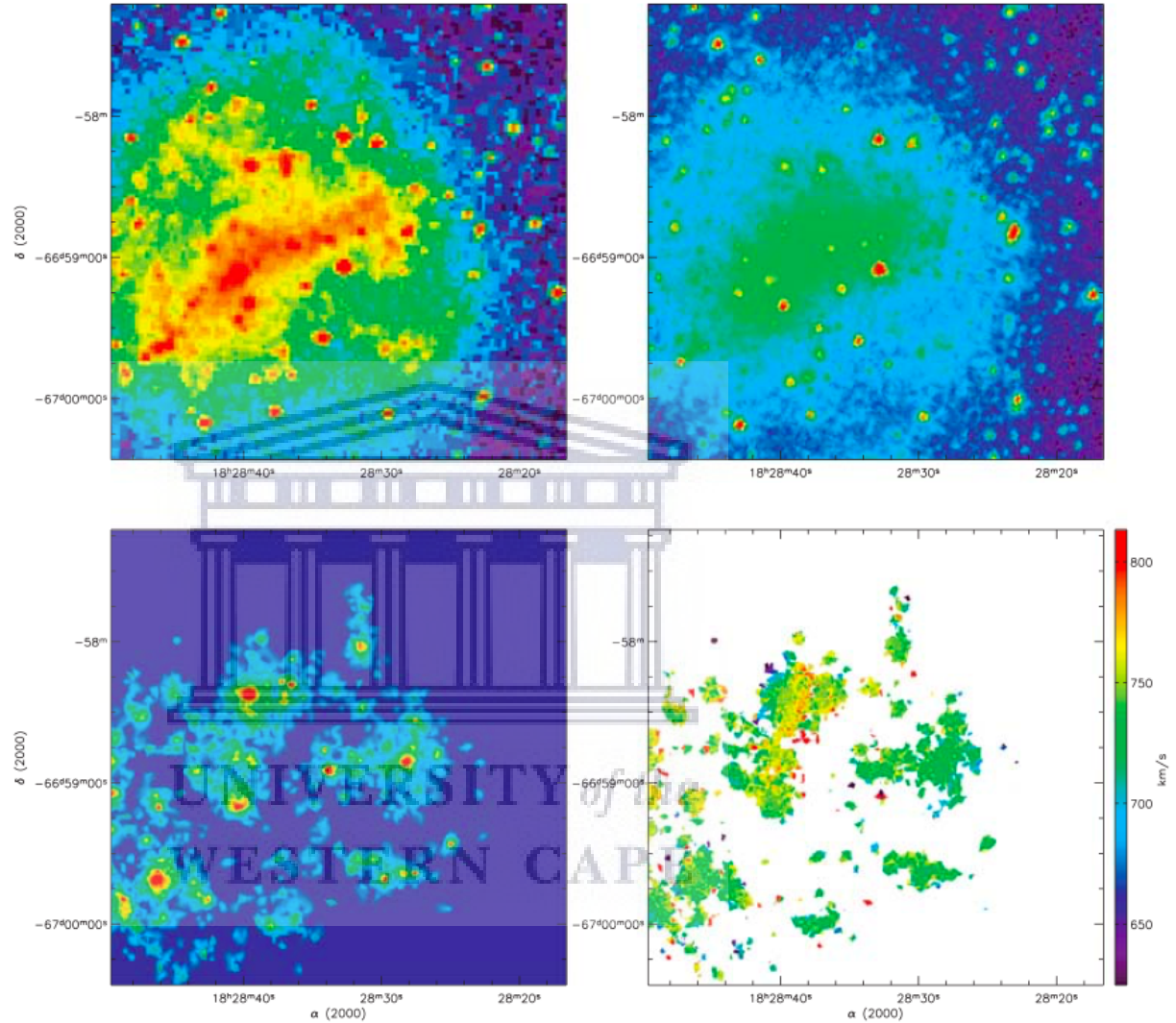


Figure 5: Various images of IC 4710 in different bands derived by Daigle et al. (2006). The top left panel is the X-DSS image obtained in blue band, top right panel is the *Spitzer* IRAC 3.6  $\mu\text{m}$  image, bottom left panel is the  $\text{H}\alpha$  monochromatic image, and the bottom right panel is the  $\text{H}\alpha$  velocity field.

The HI interferometric studies for this galaxy have never been done before. This study would allow a mass modelling study to be done for this dwarf

galaxy, using the greater extent of the HI content. In this thesis, we study the nearby (7.38 Mpc; Tully et al., 2013a) dwarf galaxy IC 4710 using the HI line observations from the Australia Telescope Compact Array (ATCA). We produce the first interferometric maps of the galaxy's HI distribution and dynamics and use these maps to measure important quantities such as total HI mass, velocity width, and size. We create a dynamical model of the galaxy using <sup>3D</sup>BAROLO. The rotation curve was obtained by fitting a 3D tilted ring model to the HI data cube of galaxy IC 4710. Dynamical modelling of IC 4710 is presented for the first time. We compare its measured rotation curve to other dwarf galaxies and models. We use our derived rotation curve to generate various mass models for the galaxy, in order to study the distribution of its DM.

## 1.6 Thesis outline

- Chapter 2 - Presents the HI data products we use in this study and the steps followed to produce them.
- Chapter 3 - Presents the energetics of the neutral interstellar medium of galaxy IC 4710 and all the steps followed in obtaining the results.
- Chapter 4 - All the procedures of modeling the dynamics of IC 4710. The channel maps showing that the model and the data are in good agreement are presented in this chapter. It also presents the mass models and the steps followed in obtaining them.
- Chapter 5 - Presents the summary of results and the conclusion.



## Chapter 2

### 2 HI imaging of IC 4710

In this work, we use the HI emission line data cube of IC 4710 from the Australia Telescope Compact Array (ATCA). The resolution of the data cube is  $26.9 \text{ arcsec} \times 25.7 \text{ arcsec}$ , with a pixel scale of  $2.5 \text{ arcsec}$  and the velocity width of  $3.5 \text{ km s}^{-1}$ . The data were acquired as part of the southern hemisphere extension of The HI Nearby Galaxy Survey. The ATCA visibility data were reduced by E. Elson, yet never published. Given that these data constitute the only known interferometric data set for the galaxy, the products generated in this thesis serve as the most accurate measures of the galaxy's HI properties.

#### 2.1 Channel maps

Figure 6 shows selected channel maps of IC 4710 ATCA data cube. The data cube consists of 85 channels, but only 16 of them show the galactic HI emission as seen in Fig. 6, between velocities  $\sim 722.0 \text{ km s}^{-1}$  to  $\sim 749.9 \text{ km s}^{-1}$ . The galactic HI emission shows that the galaxy is rotating, but further kinematics investigations will be done in Chapter 4 to understand the HI emission seen in these channel maps.

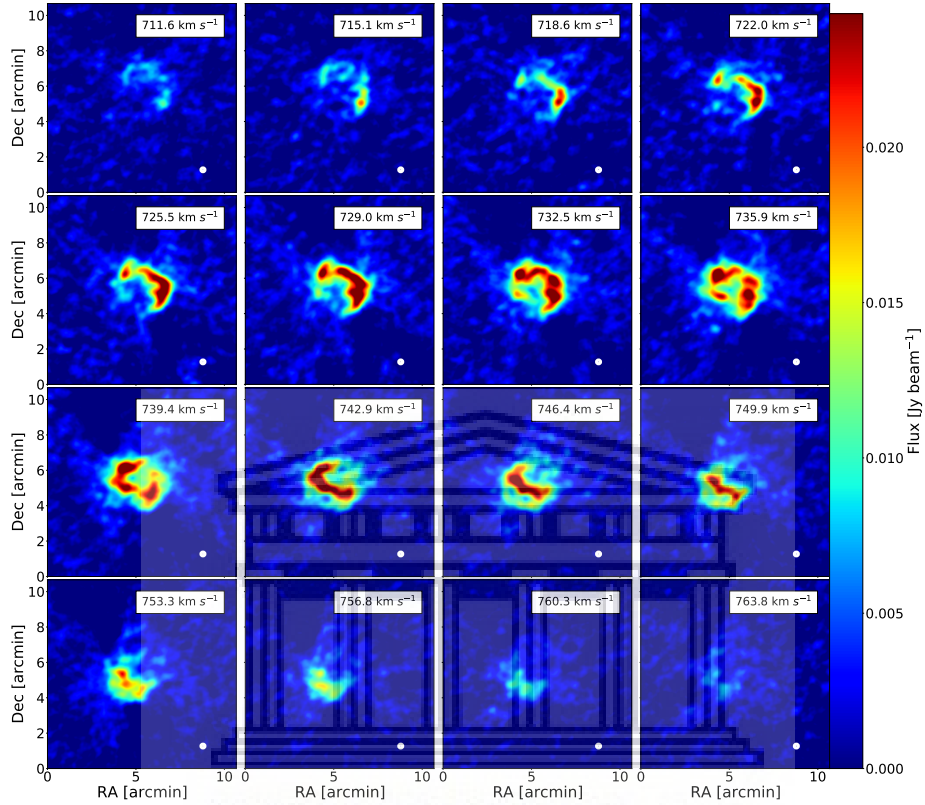


Figure 6: HI channel maps of IC 4710 based on the ATCA data cube (jet scale ranges from 0 to  $27\sigma$ , where  $\sigma = 0.909 \text{ mJy beam}^{-1}$ ). This  $\sigma$  was obtained from the line-free channel. The velocity width of each channel is  $3.5 \text{ km s}^{-1}$ , and the velocity for each channel is at the top right corner of each panel. The synthesized beam of  $26.9 \text{ arcsec} \times 25.7 \text{ arcsec}$  is shown in white at the bottom right corner of each panel.

## 2.2 Distribution of noise in a line-free channel

The distribution of noise in a line-free channel is shown in Fig. 7 with the fitted Gaussian profile. The distribution of noise in a line-free channel was generated from the second channel, and there are Gaussian parameters shown in the figure, where  $\sigma = 0.909 \text{ mJy beam}^{-1}$  and  $\mu = 1.479 \text{ mJy beam}^{-1}$ . This  $\sigma$  is the standard deviation of the noise in that line-free channel.

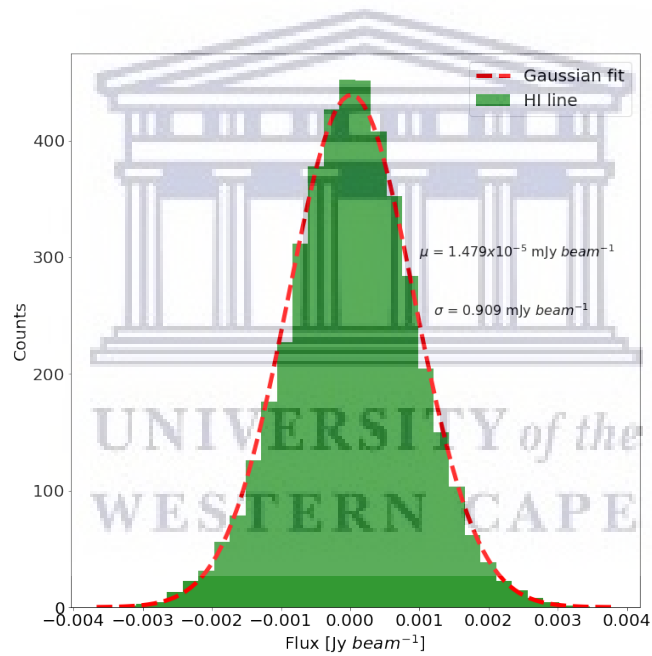


Figure 7: The distribution of noise in a line-free channel of IC 4710 ATCA data cube. The green histogram represent the HI data cube and the red dashed line is the Gaussian fit. The Gaussian parameters ( $\sigma$  and  $\mu$ ) are shown in the figure.

### 2.3 HI total intensity map

The HI total intensity map of IC 4710 obtained from the masked HI ATCA data cube is presented in Fig. 8. The data cube was masked by applying a  $3\sigma$  cut to it. There is a clear HI depression at the centre of IC 4710, where the HI surface density is only around  $3 M_{\odot} \text{ pc}^{-2}$ . Further out from the centre, there is a surrounding annulus of higher HI surface density of about  $6.5 M_{\odot} \text{ pc}^{-2}$ . In Chapter 3, we investigate possible causes of this observed HI depression. The infrared image of IC 4710 at  $3.6 \mu\text{m}$  from the *Spitzer* telescope is presented in Fig. 9. Figure 9 includes the HI contours shown in Fig. 8 for comparison, indicating that the HI extends further out than the distribution of stars within the galaxy. We placed an ellipse (with semi-major axis = 96.5 arcsec and semi-minor axis = 76.5 arcsec) on the HI total intensity map as the means of approximately measuring the extent of the HI distribution. The ellipse was placed at a surface density level of  $1 M_{\odot} \text{ pc}^{-2}$ , it was often seen in literature that they use the same surface density level to measure the extent of the HI distribution.

The HI total intensity map gives the amount of gas at each pixel. The units of the HI total intensity map were converted from  $\text{Jy km s}^{-1}$  to  $M_{\odot} \text{ pc}^{-2}$ . We used the ellipse overlaid on the HI total intensity map to determine the inclination angle of the disk through Eqn. 1:

$$i = \arccos\left(\frac{b}{a}\right), \quad (1)$$

where  $i$  refers to the inclination angle, which tells how much the galaxy is inclined relative to us, where  $b$  is the minor axis length, and  $a$  is the major axis length of a fitted ellipse. We found the inclination angle to be  $i = 37.6$  degrees.

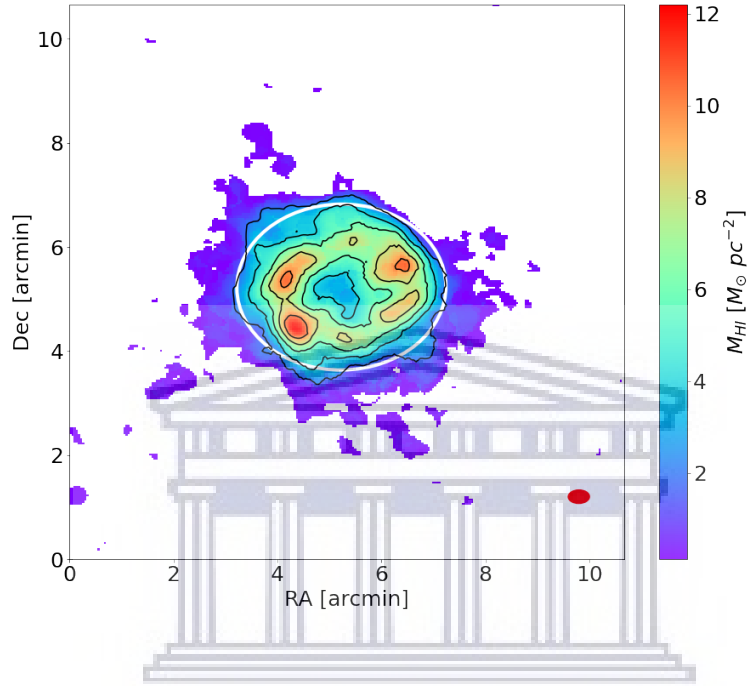


Figure 8: The HI total intensity map was obtained from the masked ATCA data cube of IC 4710. The HI flux density contours are overlaid in black at levels of 2 to  $10 M_{\odot} \text{ pc}^{-2}$  in steps of  $2 M_{\odot} \text{ pc}^{-2}$ . The white ellipse has a semi-major axis length of 96.5 arcsec and the semi-minor axis length of 76.5 arcsec. The synthesized beam of  $26.9 \text{ arcsec} \times 25.7 \text{ arcsec}$  is shown in red at the bottom right corner.

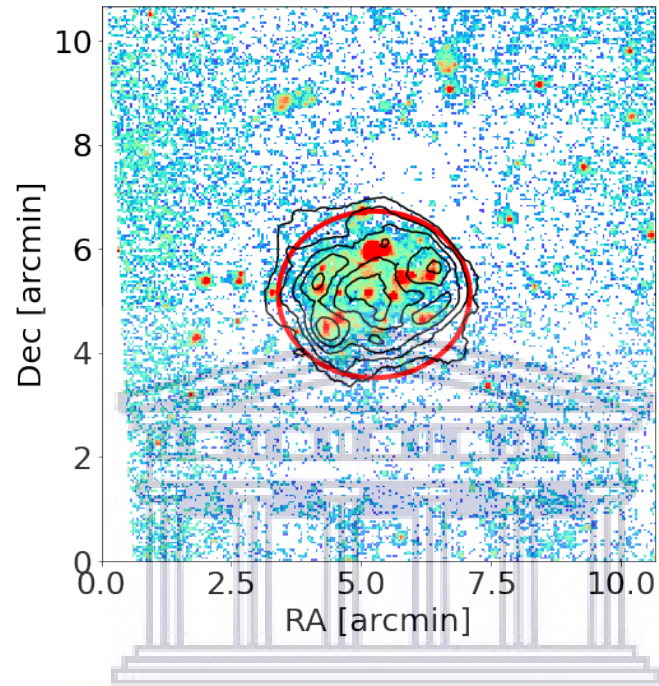


Figure 9: Infrared image of IC 4710 produced from *Spitzer* 3.6  $\mu\text{m}$  imaging. The HI flux density contours are presented in black at levels of 2 to  $10 M_{\odot} \text{pc}^{-2}$  in steps of  $2 M_{\odot} \text{pc}^{-2}$ . The red ellipse has the semi major axis length of 96.5 arcsec and the semi minor axis length of 76.5 arcsec.

The total HI mass ( $M_{\text{HI}}$ ) was calculated through Eqn. 2 (Karachentsev et al., 2016):

$$M_{\text{HI}}[M_{\odot}] = 2.36 \times 10^5 D^2 \times \Sigma_i S_i \times \Delta v, \quad (2)$$

where D is the the Tip of the Red Giant Branch (TRGB) distance ( $7.38 \pm 0.1$  Mpc) adopted from Tully et al. (2013a), and  $\Sigma_i(S_i \times \Delta v)$  is the sum of all the emission in every channel of the masked data cube in units of Jy km s<sup>-1</sup>.  $M_{\text{HI}}$  was found to be  $2.98 \pm 0.01 \times 10^8 M_{\odot}$ .

## 2.4 HI intensity-weighted-mean velocity field map

The HI intensity-weighted-mean velocity field map is presented in Fig. 10 and it was generated through Eqn. 3:

$$\langle V \rangle = \frac{\Sigma_i S_i \times v_i}{\Sigma_i S_i}, \quad (3)$$

where i is the i-th channel,  $S_i$  is the flux in the i-th channel in units of Jy beam<sup>-1</sup> and  $v_i$  is the velocity of each channel in units of km s<sup>-1</sup>. The HI intensity-weighted-mean velocity field map is in units of km s<sup>-1</sup>.

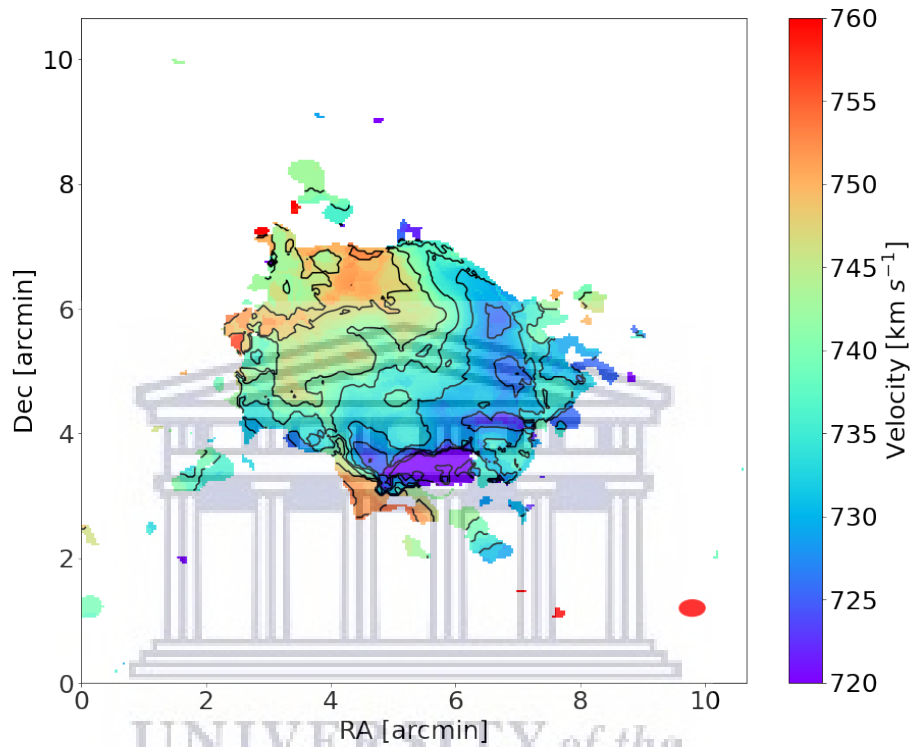


Figure 10: The HI intensity-weighted-mean velocity field map obtained from masked ATCA data cube. The contours are presented in black at levels of 717 to 757  $\text{km s}^{-1}$  in steps of 5  $\text{km s}^{-1}$ . The colour bar shows the colour scale in units of  $\text{km s}^{-1}$ . The synthesized beam of 26.9 arcsec  $\times$  25.7 arcsec is shown in red at the bottom right corner.

The HI intensity-weighted-mean velocity field map does have a coherent velocity gradient across it. The south-eastern portion of the galaxy is moving towards us, and the north-western portion is the receding side of the galaxy. A clear gradient of velocity from the south-west to the north-east is indicative of a dominant circular component to the gas dynamics. Therefore, the galaxy is rotating. The HI intensity-weighted-mean velocity contours are roughly parallel



to each other, indicating that the galaxy's rotation curve must steadily rise with radius.

Later in Chapter 4, we investigate in more detail the kinematics of this galaxy to understand the structure of the HI intensity-weighted-mean velocity field map that we have here.

## 2.5 Velocity dispersion map

The velocity dispersion map is presented in Fig. 11. The velocity dispersion map is a measure of spread about the intensity-weighted mean. Our velocity dispersion map was obtained through Eqn. 4:

$$\sigma = \sqrt{\frac{\sum_i S_i \times (v_i - \langle v \rangle)^2}{\sum_i S_i}}, \quad (4)$$

where  $i$  is the  $i$ -th channel,  $S_i$  is the flux in the  $i$ -th channel in units of Jy beam<sup>-1</sup> and  $v_i$  is the velocity of each channel in units of km s<sup>-1</sup>. The velocity dispersion map is in units of km s<sup>-1</sup>.

UNIVERSITY of the  
WESTERN CAPE

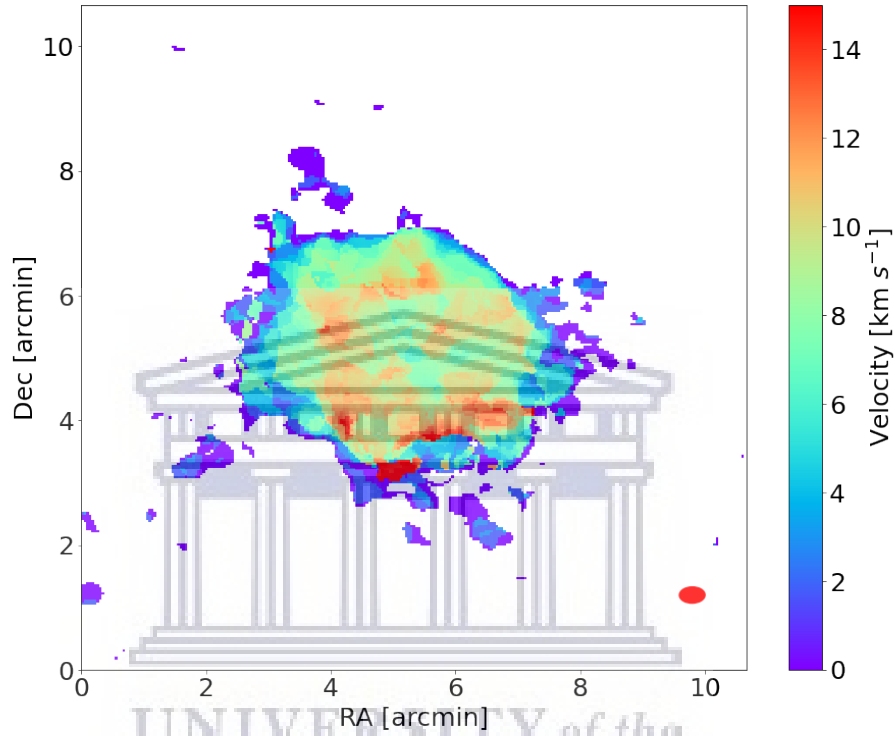


Figure 11: The velocity dispersion map obtained from the masked ATCA data cube. The colour bar shows the colour scale in units of  $\text{km s}^{-1}$ . The synthesized beam of  $26.9 \text{ arcsec} \times 25.7 \text{ arcsec}$  is shown in red at the bottom right corner.

At the center of the galaxy where we see a HI depression, velocity dispersion is approximately  $7 \text{ km s}^{-1}$ . At larger radial where we see the annulus of higher HI surface density, the velocity dispersions are higher on average by approximately  $10 \text{ km s}^{-1}$ .

## 2.6 HI global profile

An integrated HI spectrum for IC 4710 was generated by summing the flux above  $\sigma = 0.909 \text{ mJy beam}^{-1}$  in each channel. The spectrum is shown in Fig. 12.

A defining feature of the profile is its Gaussian shape. Despite the channel maps of IC 4710 clearly showing the galaxy to have a circular rotation component, the HI profile of IC 4710 is not double-horned, and more likely due to the galaxy's rotation curve varying as  $V \propto R$  - as suggested by the HI intensity-weighted-mean velocity contours .

The widths of the HI spectrum at the level of 50% and 20% of the peak flux density were measured. In Fig. 12,  $W_{50}$  and  $W_{20}$  are indicated by the cyan and black-dashed lines, respectively. In order to generate reliable uncertainty estimates for  $W_{50}$  and  $W_{20}$ , we measured the quantities several times, each time using a different flux level from the 80th to 100th percentile of the flux by interpolating using the *scipy* package and took the standard deviation for the 1-sigma error.

Having generated reliable measures of  $W_{20} = 45 \pm 0.05 \text{ km s}^{-1}$  and  $W_{50} = 30 \pm 0.12 \text{ km s}^{-1}$ , we used them to calculate the systemic velocity of the galaxy using equation:

$$V_{\text{sys}} = 0.25 \times (V_{\text{high}20\%} + V_{\text{low}20\%} + V_{\text{high}50\%} + V_{\text{low}50\%}) \quad (5)$$

Propagating the errors on  $W_{50}$  and  $W_{20}$  yields  $V_{\text{sys}} = 737 \pm 2.9 \text{ km s}^{-1}$ . Our measures of  $V_{\text{sys}}$  can be used with the Cosmic Flows Distance Calculator (Kourkchi et al., 2020) to produce a distance estimate that is corrected for bulk

flows. The distance estimated is 9.39 Mpc, which is much greater than the Tip of the Red Giant Branch (TRGB) distance of  $7.38 \pm 0.1$  Mpc (Tully et al., 2013a). The TRGB distance is determined from the luminosity of Red Giant Branch (RGB) stars at the beginning of the central helium burning (Tully et al., 2013a). In this work, we adopt the TRGB distance estimate, since Tully et al. (2013b) mentioned that the TRGB method is the best for determining distances for nearby galaxies.

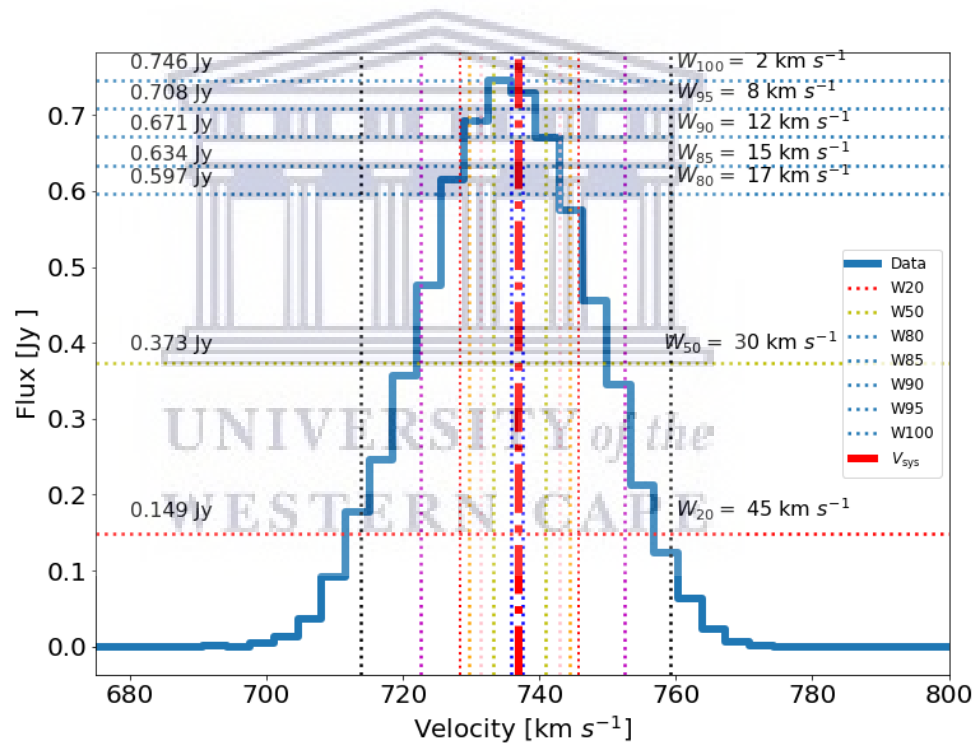


Figure 12: The HI global profile of IC 4710 based on the ATCA data cube with the  $W_{50}$  and  $W_{20}$  indicated by the cyan- and black-dashed lines. The red dash-dotted line shows the systemic velocity ( $V_{\text{sys}}$  of  $737 \pm 2.9$  km s $^{-1}$ ).

## 2.7 Mass estimates

To determine the maximum speed at which the galaxy is rotating ( $V_{\max}$ ), we used the following equation from [Teodoro et al. \(2015\)](#):

$$V_{\max} = \frac{W_{50}}{2\sin(i)}, \quad (6)$$

where  $i$  is the inclination angle of IC 4710. This gives an estimate of  $V_{\max} = 24.6 \pm 0.1 \text{ km s}^{-1}$ .  $V_{\max}$  (of  $W_{50}$ ) was then used in the following equation:

$$M_{\text{total}} = \frac{RV_{\max}^2}{G}, \quad (7)$$

where  $R$  is the HI radius of the galaxy and  $G$  is the gravitational constant. This gives the dynamical mass ( $M_{\text{total}}$ ) estimate of  $M_{\text{total}} = 6.1 \pm 0.02 \times 10^8 M_{\odot}$ . In order to determine the stellar mass, we adopted a total far-infrared luminosity of  $L_{*} = 10^{8.16} L_{\odot}$  from [Smith et al. \(2007\)](#) and assumed mass-to-light ratio of  $0.1 M_{\odot}/L_{\odot}$ . We could not find any NIR measurements, but FIR also traces stellar mass. We could not find the mass-to-light ratio of IC 4710, but mass-to-light ratios of  $0.1 M_{\odot}/L_{\odot}$  to  $0.5 M_{\odot}/L_{\odot}$  were often seen in literature for dwarf galaxies. We obtained the stellar mass estimate of  $M_{*} = 1.45 \times 10^7 M_{\odot}$ . The dynamical mass, HI mass, and the stellar mass were used to determine the dark matter mass ( $M_{\text{DM}}$ ) as shown in the following Eqn:

$$M_{\text{DM}} = M_{\text{total}} - M_{\text{HI}} - M_{*}, \quad (8)$$

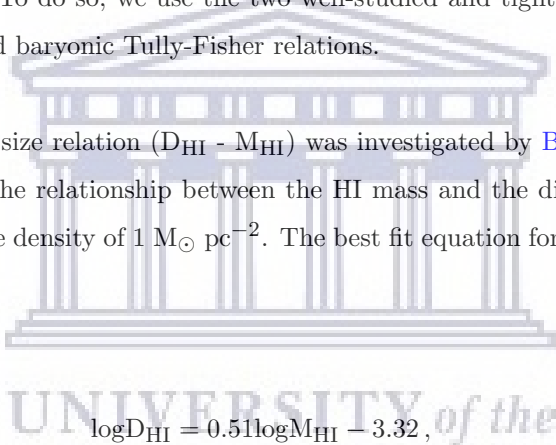
yielding the estimate of  $M_{\text{DM}} = 2.96 \pm 0.01 \times 10^8 M_{\odot}$ . If we assume the stellar mass-to-light ratio as high as  $0.5 M_{\odot}/L_{\odot}$ ,  $M_{\text{DM}} = 2.4 \pm 0.01 \times 10^8 M_{\odot}$ .  $M_{\text{DM}}$  is therefore in the range  $2 - 3 \times 10^8 M_{\odot}$ . Dwarf galaxies tend to be deficient in molecular hydrogen ( $\text{H}_2$ ) ([Higdon et al., 2006](#)), we therefore do not consider an  $\text{H}_2$  contribution to the galaxy's potential. Comparing the  $M_{\text{DM}}$ ,  $M_{*}$  and  $M_{\text{HI}}$  to the dynamical mass, we find that  $M_{\text{DM}} \sim 48.7\%$ ,  $M_{*} \sim 2.4\%$  and

$M_{\text{HI}} \sim 48.9\%$ . Therefore, the galaxy has roughly an equal amount of dark and baryonic matter, and this is not typical for dwarf galaxies as they are expected to be dark matter dominated. We further investigate by doing mass modeling in Chapter 4.

## 2.8 Mass-size and baryonic Tully-Fisher relations

In this section, we compare our galaxy IC 4710 to other galaxies to see if it is peculiar or not. To do so, we use the two well-studied and tight relations, the HI mass-size, and baryonic Tully-Fisher relations.

The HI mass-size relation ( $D_{\text{HI}} - M_{\text{HI}}$ ) was investigated by [Broeils & Rhee \(1997\)](#). This is the relationship between the HI mass and the diameter of the HI disk at surface density of  $1 M_{\odot} \text{pc}^{-2}$ . The best fit equation for the mass-size relation is:



$$\log D_{\text{HI}} = 0.51 \log M_{\text{HI}} - 3.32, \quad (9)$$

where  $D_{\text{HI}}$  is the diameter of the HI disk in units of kpc and  $M_{\text{HI}}$  is the HI mass in units of  $M_{\odot}$ . It was further studied by [Broeils & Rhee \(1997\)](#) that the average surface density is almost the same for different galaxies since the slope is  $\sim 0.5$ .

We present the  $D_{\text{HI}} - M_{\text{HI}}$  relation in Fig. 13. We used the Westerbork HI Survey of Spiral and Irregular Galaxies (WHISP) data from [Wang et al. \(2016\)](#) and the measured  $M_{\text{HI}}$  and  $D_{\text{HI}}$  of IC 4710 as presented in section 2.7. The WHISP data is a sample of 542 galaxies, we then chose only the first 13 dwarf galaxies. The WHISP data lie very close to the  $D_{\text{HI}} - M_{\text{HI}}$  relation, and IC 4710 does not deviate significantly from the HI mass-size relation, suggesting that its HI distribution is typical for a galaxy of its mass.

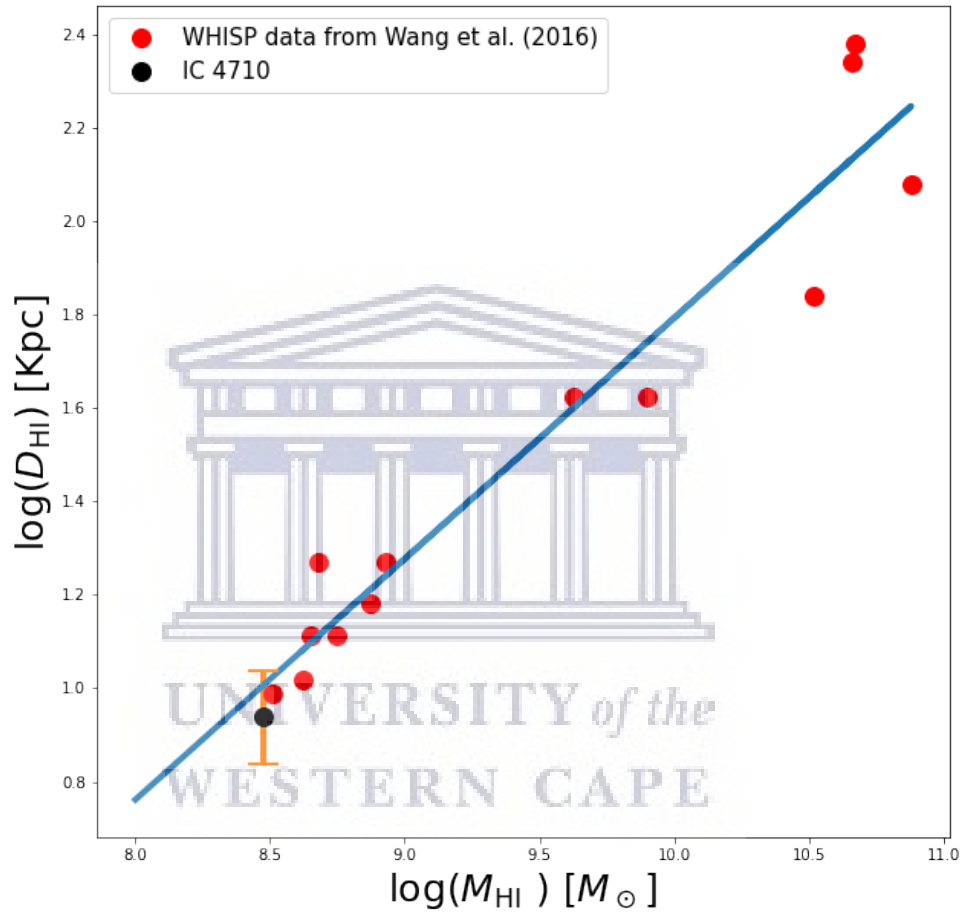


Figure 13: The plot of HI mass ( $M_{\text{HI}}$ ) and HI diameter ( $D_{\text{HI}}$ ) which is called the mass-size relation. The red dots represent the WHISP data adopted from Wang et al. (2016) and the black dot represent the measured  $M_{\text{HI}}$  and  $D_{\text{HI}}$  of IC 4710. The blue solid line represent the best fit mass-size relation.

The baryonic Tully-Fisher relation is the relationship between the baryonic mass and the circular velocity of spiral galaxies. It is important because it

gives detailed information on the galaxy formation and evolution models (Lelli et al., 2019). The baryonic Tully-Fisher relation helps in understanding how the rotation velocities differ with the galaxy properties (Glowacki et al., 2020). The baryonic mass is estimated as:

$$M_b = M_{\text{HI}} + \Upsilon_* L, \quad (10)$$

where  $M_{\text{HI}}$  is the HI mass in units of  $M_\odot$ ,  $\Upsilon_*$  is the mass-to-light ratio, and  $L$  is the luminosity. The circular velocity from Bottinelli et al. (1983) is estimated as:

$$V_c = \frac{W_{50}}{2\sin(i)}, \quad (11)$$

where  $i$  is the galaxy's inclination angle, and  $W_{50}$  is the width of the HI spectrum at a level of 50% of the peak flux density. We present the baryonic Tully-Fisher relations in Fig. 14, where we used the data of 41 dwarf galaxies from Woo et al. (2008), data of 118 disk galaxies from Lelli et al. (2016), and the measured  $V_{\text{max}} = 24.6 \text{ km s}^{-1}$  obtained from  $W_{50}$  and baryonic mass obtained in section 2.7. The baryonic mass from Lelli et al. (2016) spans a larger range ( $10^8 \lesssim M_b/M_\odot \lesssim 10^{11}$ ). The position of IC 4710 is contained well within the scatter of the Woo et al. (2008), and Lelli et al. (2016) data. The dynamics of IC 4710 are consistent with those typically measured for dwarf galaxies.



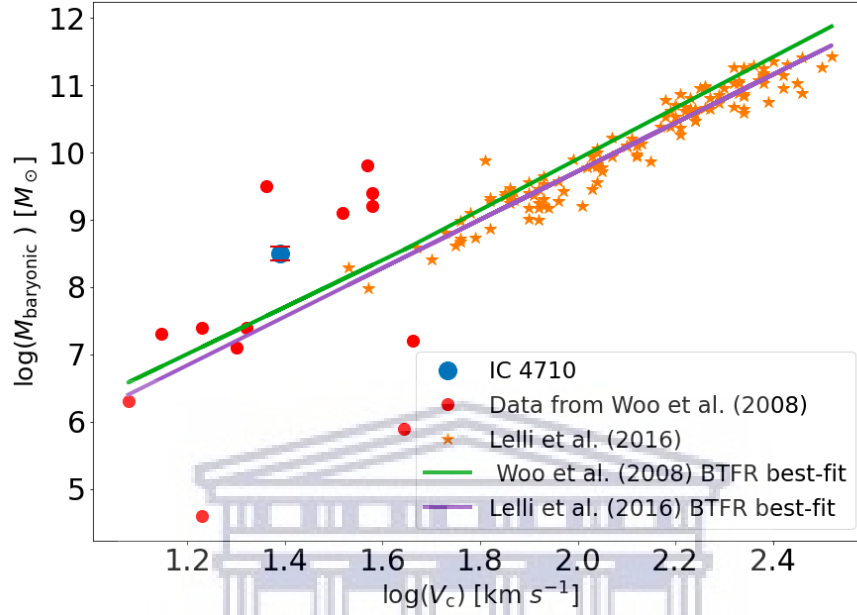


Figure 14: The plot of circular velocity ( $V_c$ ) and baryonic mass ( $M_{\text{baryonic}}$ ) which is called the baryonic Tully-Fisher relation. The red dots represent the data adopted from [Woo et al. \(2008\)](#), the orange stars represent the data adopted from [Lelli et al. \(2016\)](#), IC 4710 is represented by the blue dot. The solid green line represents the best fit baryonic Tully-Fisher relation of the data of [Woo et al. \(2008\)](#), and the solid purple line represents the best fit baryonic Tully-Fisher relation of the data of [Lelli et al. \(2016\)](#).

## Chapter 3

### 3 Energetics of the neutral interstellar medium

Our HI total intensity map of IC 4710 clearly reveals the presence of a central deficiency of HI. In this chapter, we quantify the energetics of the stars and interstellar medium in IC 4710 in order to investigate two separate scenarios that could have led to the central HI depression. Firstly, we consider the possibility of mechanical feedback from the galaxy's centralized stellar population having excavated the HI from the centre of the galaxy. Secondly, we check whether the central HI could simply have been consumed by star formation. We also consider results from previous studies in order to draw our conclusions.

#### 3.1 The role that HI plays in star formation

The cycle of gas in galaxies is a major driver of their evolution. Star formation consumes HI. The typical SFR for dwarf galaxy is  $< 0.1 M_{\odot} \text{ year}^{-1}$  (Lee et al., 2009), while the typical HI mass is  $\sim 10^8 - 10^9 M_{\odot}$  (Weinberg et al., 1991). Therefore, without the HI supply being replenished in some way, most dwarf galaxies will stop significantly forming stars (Hunt et al., 2020; Saha et al., 2006).

Today, we know two main modes by which galaxies acquire fresh supplies of HI to sustain their star formation. Sancisi et al. (2008) showed cold accretion to be the main mechanism by which low-mass galaxies acquire their gas. They mentioned that the accretion mechanism occurs in two ways, either by gas-rich galaxies merging or gas falling from the IGM. This added gas either goes to the galactic halo or the outer parts of the galaxy, and it fuels star formation. For the star formation process to be continuous, the gas should be supplied because it plays a huge role in the evolution of galaxies. However, the amount of new gas that feeds the star formation is not known. The SFR differs across galaxies and across an individual galactic disk.

### 3.2 Galactic fountain scheme

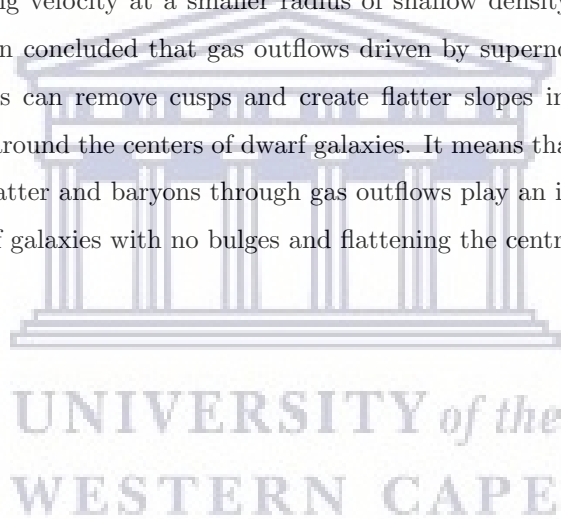
Star formation in a galaxy can significantly impact the distribution and kinematics of its gas. [Shapiro & Field \(1976\)](#) presented and described the Galactic Fountain model in which the mechanical energy deposited by stars in a galaxy into its ISM can eject material into the halo. This removal of material (specifically neutral hydrogen in both atomic and molecular forms) can lead to a fast decline in the star formation rate of the galaxy.

In the galactic fountain scenario, mechanical energy from stars deposited into the ISM is responsible for transferring gas from a galaxy's disk into its halo. [Fraternali & Binney \(2006\)](#) also presented their galactic fountain model, and they stated that the fountain needs energy for it to be continuous, and the amount of energy coming from supernova supports the fountain. They mentioned that most particles at small radii are most likely to return to the disk. They assumed the outflow rate of gas to be proportional to the SFR since the stellar winds and supernova explosions are what cause the gas outflow. They discovered that the time it takes for the gas to travel to the halo and back to the disc is different at every radius, and the kick velocity (velocity at which particles travel) is also different for every particle.

Figure 15 shows the galactic fountain process from [Spitoni \(2010\)](#). They described it in short that the supernovae found in areas of star formation produce bubbles of hot gas. When the hot gas bubbles become thicker than the disk, they blow out of the galactic disk and form a galactic fountain. Then the hot gas will cool off and create clouds which will return to the galactic disk.

### 3.2.1 Gas outflows in dwarf galaxies

Several studies have explored different baryonic processes such as the gas outflows driven by supernova explosions (Governato et al., 2010; Oh et al., 2015). Dark matter and baryons in dwarf galaxies can interact through gas outflows to form new dwarf galaxies with no bulge (Oh et al., 2008). Oh et al. (2011) analysed the baryonic and dark matter mass distributions of simulated dwarf galaxies, and they found that their rotation curves and dark matter density profiles are in good agreement with the THINGS dwarf galaxies. Their results also show a linearly increasing velocity at a smaller radius of shallow density profiles. Oh et al. (2015) then concluded that gas outflows driven by supernova explosions in dwarf galaxies can remove cusps and create flatter slopes in dark matter density profiles around the centers of dwarf galaxies. It means that interactions between dark matter and baryons through gas outflows play an important role in forming dwarf galaxies with no bulges and flattening the central cusp.



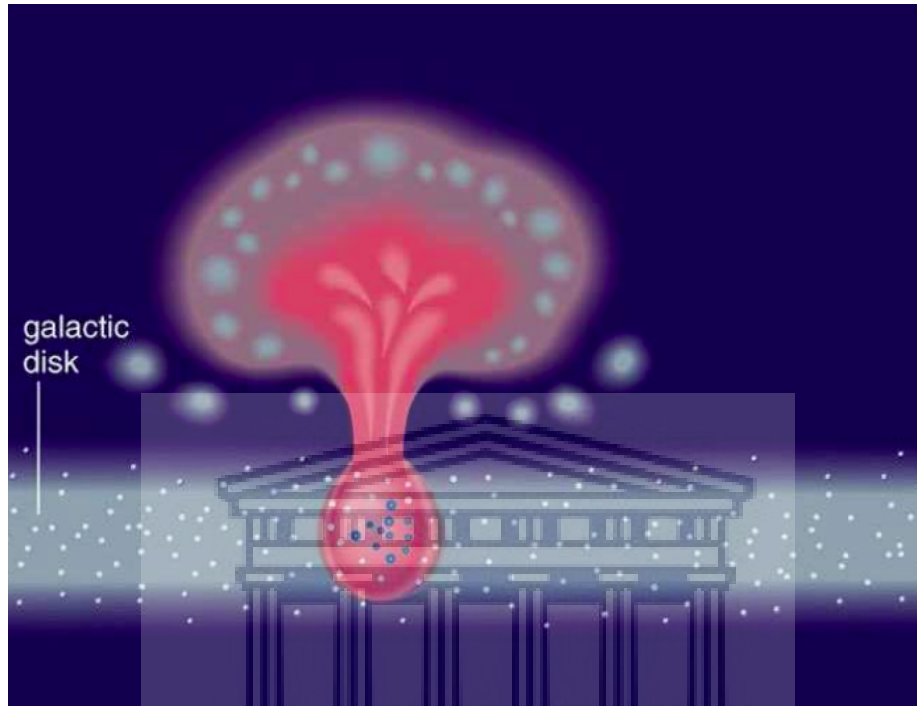


Figure 15: The galactic fountain scenario from [Spitoni \(2010\)](#). The grey surface with white dots is the galactic disk. The red bottom circle with the blue dots in the galactic disk is the young stellar cluster, in which supernova explosions in the stellar cluster blow a superbubble in the galactic disk. The outgoing white ovals represent the hot gas blowing out to the halo after the superbubbles become thicker than the disk. The blue outer bubbles surrounding the halo are the clouds formed after the hot gas has cooled down. The outer white circles are the clouds going back to the galactic disk.

There are both gas-rich and gas-poor dwarf galaxies. For a dwarf galaxy to be gas-poor, it means there was a gas removal mechanism, such as galactic winds, ram pressure stripping, etc (Steyrleithner et al., 2020). Theoretical studies proved that supernovae-driven winds are important in the evolution of dwarf galaxies because of their smaller  $V_{\text{esc}}$  (Martin et al., 1998; Dekel et al., 1986). However, galactic winds are scarce in dwarf galaxies (Martin et al., 1998).

There are different mechanical energy sources in dwarf galaxies, such as supernova explosions, stellar winds, photoionization, etc. These sources contribute energy to the ISM.



UNIVERSITY *of the*  
WESTERN CAPE

### 3.3 The central depression of HI in IC 4710

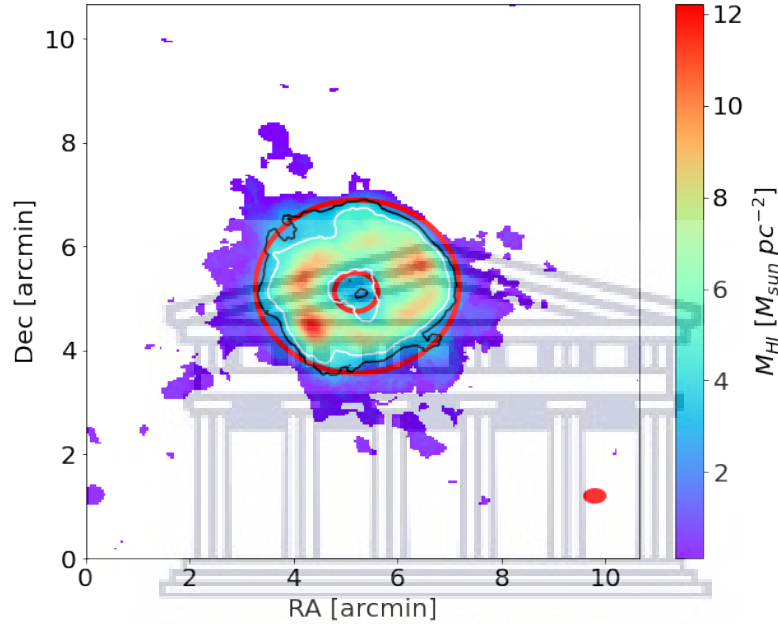


Figure 16: The HI total intensity map was obtained from the masked ATCA data cube of IC 4710. The HI flux density contours are overlaid in black at levels of  $3 M_{\odot} \text{ pc}^{-2}$  and in white at levels of  $4.5 M_{\odot} \text{ pc}^{-2}$ . The red outer ellipse has a semi-major axis length of 98 arcsec and the semi-minor axis length of 84 arcsec. The red inner ellipse has a semi-major axis length of 24.5 arcsec and the semi-minor axis length of 21 arcsec. The synthesized beam of  $26.9 \text{ arcsec} \times 25.7 \text{ arcsec}$  is shown in red at the bottom right corner.

We did a few calculations to find out the cause of the HI depression at the center of the galaxy. The overlaid HI surface density contours at levels of  $3 M_{\odot} \text{ pc}^{-2}$  and  $4.5 M_{\odot} \text{ pc}^{-2}$  in Fig. 16 were used because they clearly show where the HI of the surrounding annulus starts and ends. The flux contours also show the size of the central region where there is a HI depression. The results will help us in

knowing the HI radius. The outer black contours of level  $3 \text{ M}_{\odot} \text{ pc}^{-2}$  give us the actual size of the HI emission. We fitted an ellipse to that flux level, from which a radius of 3.5 kpc was obtained. The obtained radius was used to calculate the area of a disk, and we found it to be  $3.9 \times 10^7 \text{ pc}^2$ . We then divided the HI mass within 3.5 kpc by the area of the disk to calculate an average HI mass surface density of  $\sim 7.6 \text{ M}_{\odot} \text{ pc}^{-2}$ . In order to calculate the amount of HI mass that could have been transferred away from the portion of the galaxy that we see as the central HI depression, we use our estimate of the average HI mass surface density to calculate how much mass was within the central cavity. Given the cavity's measured diameter of 0.88 kpc, we estimate a mass of  $1.86 \times 10^7 \text{ M}_{\odot}$ . Our estimate of  $1.86 \times 10^7 \text{ M}_{\odot}$  must be compared to the actual observed total HI mass within the central cavity,  $1.94 \times 10^6 \text{ M}_{\odot}$ . The difference of  $1.67 \times 10^7 \text{ M}_{\odot}$  between the two masses serves as our estimate of the amount of HI mass that was removed from the central portion of the galaxy in order to produce the observed depression.

Assuming that the depression is caused by the stars driving the gas out, we use the following equation from [Meurer et al. \(1996\)](#) to quantify the total energy:

$$K_E = \frac{1}{8} \times M_g \times V_{\text{exp}}^2, \quad (12)$$

where  $M_g$  is the mass of the expanding gas and  $V_{\text{exp}}$  is the expansion velocity.

[Elson et al. \(2011a\)](#) studied the kinematics of the dwarf galaxy NGC 2915 to investigate the cause of the double-peaked HI line profile present near the center of the galaxy. They measured an expansion velocity for the gas to be  $30 \text{ km s}^{-1}$ . Their values yielded the kinetic energy ( $E_K$ )  $\sim 5.6 \times 10^{44} \text{ J}$  for the galaxy's expanding HI gas component. NGC 2915 is of similar mass to IC 4710, and has similar SFR ([Meurer et al., 1996](#)). Therefore, we assume the same expansion velocity and we estimate a total kinetic energy of  $3.7 \times 10^{45} \text{ J}$ .



The energy needed to drive the expansion could be coming from the mechanical energy generated by stars through supernova explosions. [Chu \(2005\)](#) states the typical energy output by a type-II supernova to be  $1 \times 10^{44}$  J. If we assume all of the kinetic energy of the HI comes from supernova feedback, we require 29 supernovae. However, it is not expected that all of a supernova's energy is deposited into the ISM as mechanical energy. [Mori et al. \(2002\)](#) mentioned that only 30% of energy of the supernovae is deposited as mechanical energy. This means that we require  $\sim 95$  supernovae to account for the kinetic energy of the HI that could have been excavated from the centre of IC 4710.

In order to estimate a time interval associated with the production of 95 supernovae, we require an estimate of the SFR of IC 4710. [Calzetti et al. \(2010\)](#) estimate the average SFR surface density of IC 4710 to be  $10^{-2.823} \text{ M}_{\odot} \text{ year}^{-1} \text{ kpc}^{-2}$ , and measure the size of the star forming disk to be 3.5 kpc. These estimate and measurement yields a global SFR of  $0.06 \text{ M}_{\odot} \text{ year}^{-1}$  for IC 4710. The supernova rate is expected to be 1% of the total SFR, so it was calculated to be  $0.0006 \text{ M}_{\odot} \text{ year}^{-1}$ . Given that each type II supernova is associated with a star of mass at least  $8 \text{ M}_{\odot}$ , the minimum total mass associated with the 95 supernovae is  $760 \text{ M}_{\odot}$ . The ratio of this mass to the above-mentioned SN rate yields a time scale of  $1.31 \times 10^6$  years.

Given that O and B type stars have lifetimes ranging from  $10^5 - 10^7$  years, our calculated timescale implicates them as the stellar population potentially responsible for removing the HI from the centre of IC 4710. To further check the formation of stars could have consumed the gas at the center of the galaxy, we take the ratio of the mass removed from the center and the total SFR, which yields the time-scale of  $2.89 \times 10^8$  years.

Figure 17 shows the B band optical image of IC 4710 taken by the CTIO 1.5 m telescope. Compared to the HI intensity map, which shows the HI depression at the center of the galaxy, Fig. 17 shows that there are young stars located at the center of the galaxy, and this could mean that the stars have somehow removed the gas, either through stellar winds, and the mass that could have been removed is  $1.67 \times 10^7 M_{\odot}$ . The investigations suggest that both scenarios are a possibility.

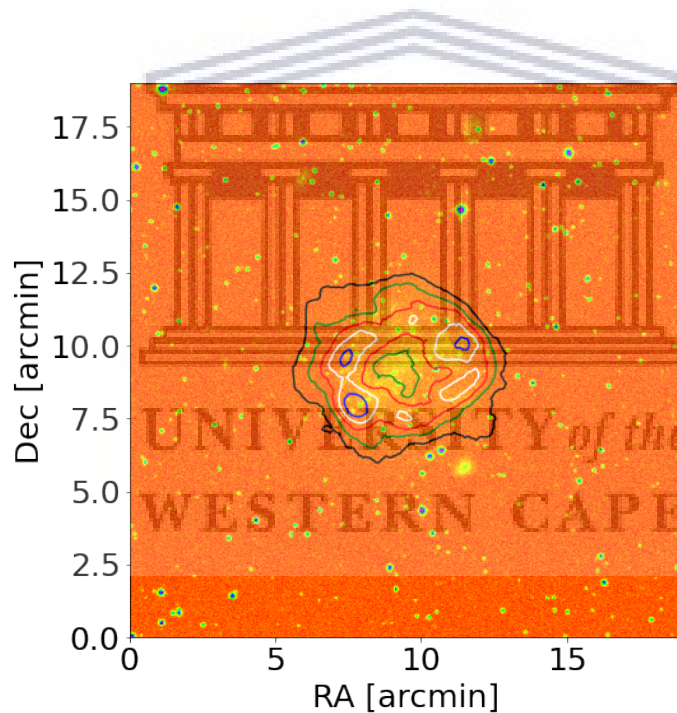


Figure 17: Optical image in B-band that comes from the CTIO 1.5 m telescope, with the overlaid HI contours in levels of  $2 M_{\odot} \text{ pc}^{-2}$  (black),  $4 M_{\odot} \text{ pc}^{-2}$  (green),  $6 M_{\odot} \text{ pc}^{-2}$  (red),  $8 M_{\odot} \text{ pc}^{-2}$  (white), and  $10 M_{\odot} \text{ pc}^{-2}$  (blue).

### 3.4 Escape velocity

We need to know the fate of the gas we assume to have been pushed out of the centre of the galaxy. Will it escape into the intergalactic medium, or will it go back into the disk? This section determines whether the gas will escape from the gravitational potential by calculating the escape velocity. Escape velocity is the speed needed for a particle to completely escape the gravitational potential of the galaxy.

Dwarf galaxies have low gravitational potential, so it does not take high velocities for the ISM to escape the dwarf galaxy. [Mac Low et al. \(1999\)](#) studied the kinematics of dwarf galaxies to understand the effect of recurring supernova explosions from starburst on ISM by also looking at the gravitational potential of their dark matter halos. They concluded that for dwarf galaxies with  $M_{\text{HI}} \lesssim 10^9 M_{\odot}$ , their gravitational potential is dominated by dark matter halo.

[Elson et al. \(2011a\)](#) studied the kinematics of NGC 2915 and found that the dark matter halo dominates its gravitational potential. They treated the density profile of the dark matter halo as a pseudo iso-thermal sphere, and calculated the escape velocity using the following Eqn:

$$V_{\text{esc}} = \sqrt{2V_{\text{max}}^2 \left(1 + \ln\left(\frac{R_{\text{max}}}{R}\right)\right)}, \quad (13)$$

where  $V_{\text{max}}$  in their case is the asymptotic value of the circular rotation velocity at a large radius ( $V_c$ ) and  $R_{\text{max}}$  is the maximum radius of the pseudo-isothermal sphere. They used  $V_c \sim 86 \text{ km s}^{-1}$  and  $R_{\text{max}} \sim 8.7 \text{ kpc}$  and they found  $V_{\text{esc}} \gtrsim 175 \text{ km s}^{-1}$  at all radii, which was higher than their expansion velocity of  $30 \text{ km s}^{-1}$ . They then concluded that the gas at the center of galaxy NGC 2915 would not escape into the intergalactic medium.

In our case,  $V_{\text{max}} \sim 24.6 \text{ km s}^{-1}$  is the maximum velocity obtained from the integrated HI spectrum of IC 4710,  $R \sim 4.34 \text{ kpc}$  is the HI radius obtained

in Chapter 2, and  $R_{\max}$  is the maximum radius of the pseudo-isothermal sphere which we adopted from [Elson et al. \(2011b\)](#) as 8.7 kpc ( since NGC 2915 and IC 4710 has similar mass). The escape velocity was found to be  $\sim 45 \text{ km s}^{-1}$ . The escape velocity obtained is larger than our assumed expansion speed of  $30 \text{ km s}^{-1}$ , meaning that the central gas will not escape into the intergalactic medium.

[Van Eymeren et al. \(2009\)](#) studied the HI kinematics of NGC 2366 using the data cube from “The HI Nearby Galaxy Survey” (THINGS, [Walter et al. \(2008\)](#)). They calculated the escape velocity for a pseudo-isothermal halo while considering two different possible radii of  $R_{\max} = 7.5 \text{ kpc}$  and  $15 \text{ kpc}$ , with  $V_c = 50 \text{ km s}^{-1}$  obtained from the rotation curve. The escape velocities for both the cases were found to be  $\sim 141 \text{ km s}^{-1}$  and  $\sim 147 \text{ km s}^{-1}$ . They used expansion velocities of  $30 \text{ km s}^{-1}$  and  $50 \text{ km s}^{-1}$ , both of which are lower than their escape velocities. They concluded that the gas is bound by gravity and will not escape unless external forces are applied. Their findings are similar to what we obtained.

[Martin et al. \(1996\)](#) studied the HI kinematics of a dwarf galaxy I Zw 18. They used an expansion speed of  $35 \text{ km s}^{-1}$ , a fixed rotation velocity at  $\sim 40 \text{ km s}^{-1}$ , and  $R_{\max} = 1 - 10 \text{ kpc}$ . They obtained the escape velocity of range  $91 - 103 \text{ km s}^{-1}$ , the expansion speed was found to be lower than the escape velocity, so these results give same conclusion that the gas will not escape into the intergalactic medium.

Our finding that the expanding HI component of IC 4710 is unlikely to escape the galaxy’s gravitational potential is consistent with the results of other studies. For the case of IC 4710, it is likely that the central population of early-type stars expelled the HI from the centre of the galaxy over a time scale of  $1.31 \times 10^6$  years.

## Chapter 4

### 4 Dynamical modeling

In Chapter 2, we produced the HI data products such as channel maps, moment maps, and the global profile. The HI properties were also used to analyze the central energetics of the galaxy. This chapter aims to understand the global kinematics of this dwarf galaxy IC 4710 through the ATCA imaging to generate a model for the rotation curve of the system. A 3D tilted ring model was fitted directly to the HI data cube. Such a model is able to constrain the radial dependence of various kinematic and geometric parameters. The rotation curve of galaxy IC 4710 has never been obtained before; this work is being done for the first time. This chapter also focuses on mass modeling to understand the distribution of masses.

Studying the gas kinematics of the galaxy is vital as it leads to understanding the dynamical structure and distribution of matter in disk galaxies. Given that late-type galaxies often have HI disks that are typically 2 or more times larger than their optical disks, HI emission line imaging serves as a particularly useful data set with which to probe a galaxy's gravitational potential out to several kpc. Once the total rotation curve has been reliably constrained using the data, it can be broken down in order to quantify the contributions to the total rotational velocity from the baryonic and dark matter components of the galaxy.

#### 4.1 Tilted ring model

[Rogstad et al. \(1974\)](#) was the first to develop the tilted-ring modeling technique. The method is based on modeling the disk of the galaxy as a set of concentric rings. Each ring is defined by a set of 4 geometrical parameters ( $X_c$ ,  $Y_c$ ,  $i$  and PA) and 2 kinematic parameters ( $V_{\text{sys}}$  and  $V_{\text{rot}}$ ) ([De Blok et al., 2008](#)):

- $X_c, Y_c$  - the central position of the galaxy
- $i$  - inclination angle, which tells how much the galaxy is inclined relative to us.
- PA - Position Angle of the major axis of the portion of the galaxy that is moving away from us, starting from the north in an anticlockwise direction on the sky.
- $V_{\text{sys}}$  - systemic velocity, which is the speed at which the galaxy is moving away from us.
- $V_{\text{rot}}$  - rotation velocity per concentric ring, which is the speed at which the galaxy is rotating.

From De Blok et al. (2008), the line-of-sight velocity with the non-circular motions ignored, is given by:

$$V_{\text{los}}(x, y) = V_{\text{sys}} + V_{\text{rot}} \sin(i) \cos(\theta), \quad (14)$$

where  $V_{\text{los}}$  is the line-of-sight velocity of each ring at radius  $R$ ,  $\theta$  is the angle measured from the major axis in the plane of the galaxy,  $x$  and  $y$  are rectangular coordinates on the sky. Angle  $\theta$  is related to PA of the galaxy by:

$$\cos(\theta) = \frac{-(x - X_c) \sin(\text{PA}) + (y - Y_c) \cos(\text{PA})}{R}, \quad (15)$$

$$\sin(\theta) = \frac{-(x - X_c) \cos(\text{PA}) + (y - Y_c) \sin(\text{PA})}{R}. \quad (16)$$

The various parameters are adjusted until an acceptably good agreement between tilted ring model and observations is achieved.

From the HI total intensity map (Fig. 8), we determined the radius of the galaxy by placing an ellipse ( $96.5 \text{ arcsec} \times 76.5 \text{ arcsec}$ ) at the HI surface density

of  $1 M_{\odot} \text{ pc}^{-2}$  (as often seen in literature), and it was found to be 4.34 kpc. The kinematics of the galaxy were modeled out to this radius. A number of 12 rings were used, where the width of each ring was 12.5 arcseconds, which is the beam major axis obtained from the header of the data cube. A weighing function ( $|\cos(\theta)|$ ) reduces the contribution to the model of points close to the minor axis of the galaxy since they have a small line-of-sight velocity component.

## 4.2 <sup>3D</sup>BAROLO

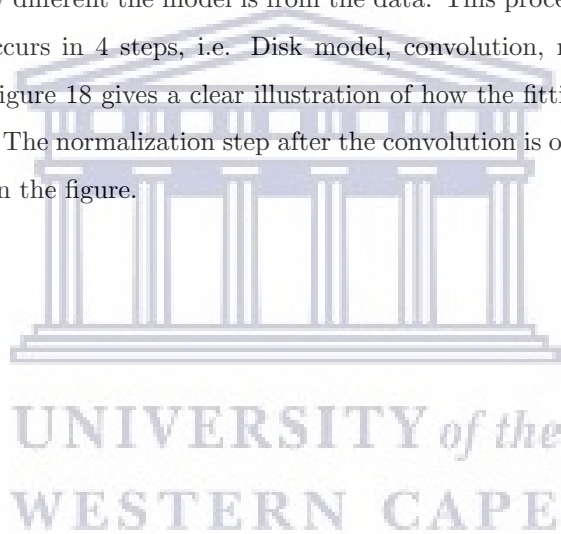
<sup>3D</sup>BAROLO is a code that generates rotation curves from using emission line data cubes as an input. This code takes in the emission line data cube and fits the tilted-ring models to it. Different kinds of observations can be used in this software, and it is not limited to HI line observations only (Teodoro et al., 2015).

This software is regarded as a natural problem solver when compared to other algorithms like the 2D algorithm ROTCUR. One of the problems that affect ROTCUR is beam smearing, which comes from the poor telescope resolution (Teodoro et al., 2015). Beam smearing thus results in the rotation curve rising too slowly at smaller radii. The effects of beam smearing are incorporated into <sup>3D</sup>BAROLO's modeling technique. Typically, the 2D algorithm fits the rings faster than the 3D algorithm, which is computationally slow. Corbelli & Schneider (1997) was the first to attempt to explore a 3D approach to study the warp of M33.

Teodoro et al. (2015) mentioned that only 3D FITS images are suitable for <sup>3D</sup>BAROLO code; the image must have two spatial dimensions and one spectral dimension. They mentioned that <sup>3D</sup>BAROLO creates models that are compared to the data cube that is used as an input, and this comparison gives the geometrical and kinematical parameters that explain the input data cube. <sup>3D</sup>BAROLO is also made for low-resolution data. The major work of <sup>3D</sup>BAROLO is to compare the model of a disk to the real data cube. This disk

is rotating and is composed of concentric rings. The rings contain gas seen in emission, and it is created in 6 dimensions (half of the dimensions are elements of velocity, and the other half dimensions are spatial dimensions). The comparison of the model to data is performed for every ring up until the best fit is achieved. The first 6 parameters of <sup>3D</sup>BAROLO are similar to the parameters of a 2D model like ROTCUR (Teodoro et al., 2015).

They further explained the minimization function between a model and data, which shows how different the model is from the data. This process of checking the difference occurs in 4 steps, i.e. Disk model, convolution, normalization, and residuals. Figure 18 gives a clear illustration of how the fitting of rings to the data occurs. The normalization step after the convolution is optional; hence it is not shown in the figure.





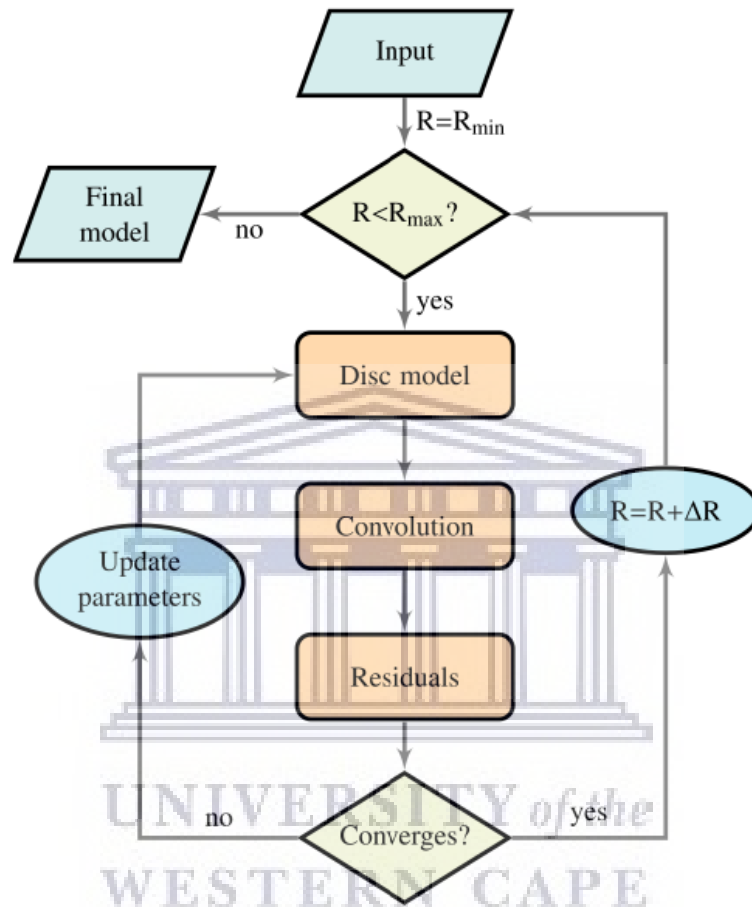


Figure 18: The flowchart taken from Teodoro et al. (2015) which shows how <sup>3D</sup>Barolo operates in fitting the rings to the data and making sure that the end results is the best match of the model and the input data.

R in Fig. 18 represents the rings. These fundamental steps in the flowchart are for building a 3D model which will be compared to the input data. Constructing the 3D model takes steps; firstly, the disk model is produced and then undergoes convolution, i.e., it is degenerated to make it have a similar spatial resolution as the data. After convolution, there is an optional step of normalizing the model to the moment 0 map of the data cube. Then the model is compared to the

input data pixel-by-pixel through residuals step, and these residuals are then summed up and put back to the minimization algorithm to check whether the model is suitable.

There are also some other features of <sup>3D</sup>BAROLO mentioned by [Teodoro et al. \(2015\)](#) (which we did not use for our work), such as:

- Source detection - It can locate and fit sources found in input data.
- Masking - <sup>3D</sup>BAROLO creates a mask to identify parts that are associated with the galaxy from the input data, and this helps in achieving a good fit.
- Automatic initial guesses - <sup>3D</sup>BAROLO can estimate the initial parameters.
- Regularization of the parameters - After fitting the six parameters, the rotation curve generated may not be physically possible, and the inclination and position angle profile could show some unrealistic scattering. This problem is solved by fitting only the rotation velocity and fixing the geometric parameters.
- Errors - <sup>3D</sup>BAROLO uses the Monte Carlo method to estimate the errors. Monte Carlo method is a method of approaching differential equations statistically ([Metropolis & Ulam, 1949](#)).

[Teodoro et al. \(2015\)](#) used <sup>3D</sup>BAROLO to derive rotation curves of galaxies in three different cases which are: high-resolution data, mid-low resolution data, and very low-resolution data. These three cases are discussed in the sections below.

#### 4.2.1 High resolution data

[Teodoro et al. \(2015\)](#) used <sup>3D</sup>BAROLO to model the rotation curves of approximately 100 nearby galaxies observed at high spatial resolution in the HI emission

line. They derived rotation curves of galaxies from different HI surveys, i.e., The HI Nearby Galaxy Survey (THINGS; Walter et al., 2008), the Very Large Array – ACS Nearby Galaxy Survey Treasury (VLA-ANGST; Ott et al., 2012), and the Hydro- gen Accretion in LOcal GALaxies Survey (HALOGAS; Heald et al., 2011). The rotation curves that they obtained are similar to the already existing rotation curves that were obtained using a 2D algorithm. They used the THINGS data cube of galaxy NGC 5055 to run <sup>3D</sup>BAROLO, where they estimated the initial values for only the inclination angle and position angle. They had only two iterations: in the first step all parameters were set to be free, and in the second step, only the rotation velocity and the dispersion velocity were set to be free. The channel maps were used for comparing their model to the input data cube as presented in Fig. 19. In Fig. 20, they presented the rotation curves for both the iterations and compared them to the rotation curves obtained by De Blok et al. (2008) with a 2D algorithm. They point out the major difference between the 2D tilted-ring model and <sup>3D</sup>BAROLO is that the 2D tilted-ring model, when applied to the whole asymmetric galaxy, returns a rotation curve that is the average of the approaching and the receding side of the galaxy. <sup>3D</sup>BAROLO, meanwhile, it takes the model with the lowest residuals and returns the rotation curve while focusing on one side of the galaxy rather than both sides of the galaxy.

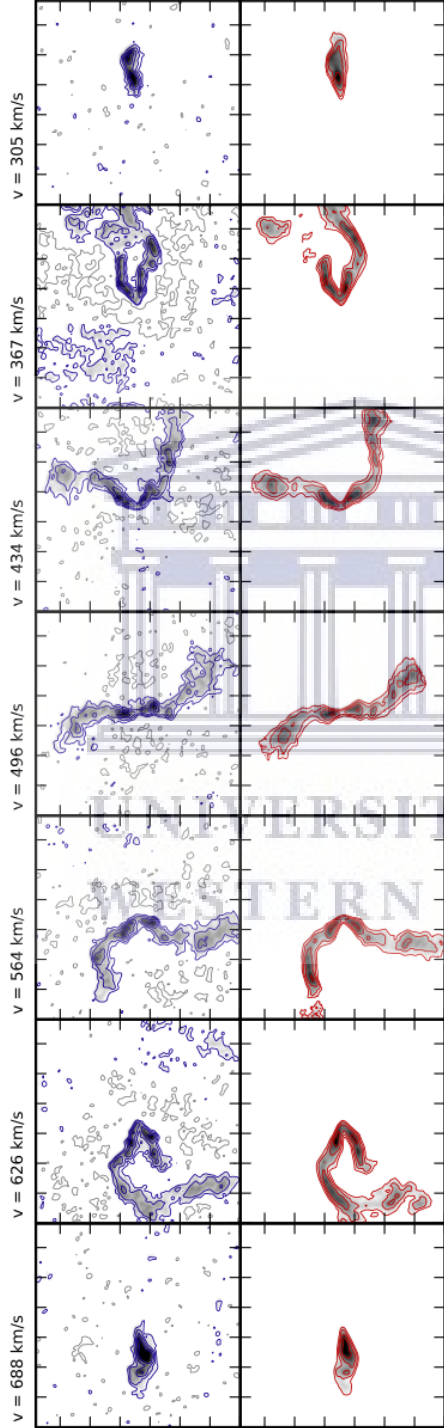


Figure 19: The channel maps from Teodoro et al. (2015). The top panels in blue are presenting the HI data cube, and the bottom panels in red are presenting the model, both the top and bottom panels are for the THINGS survey galaxy NGC 5055. The field size is  $25 \text{ arcmin} \times 25 \text{ arcmin}$ , and the contours are in levels of  $2.5\sigma$ . The grey contours are negative. The 4th and 11th channel maps correspond to the  $V_{\text{sys}}$  of  $496 \text{ km s}^{-1}$ .

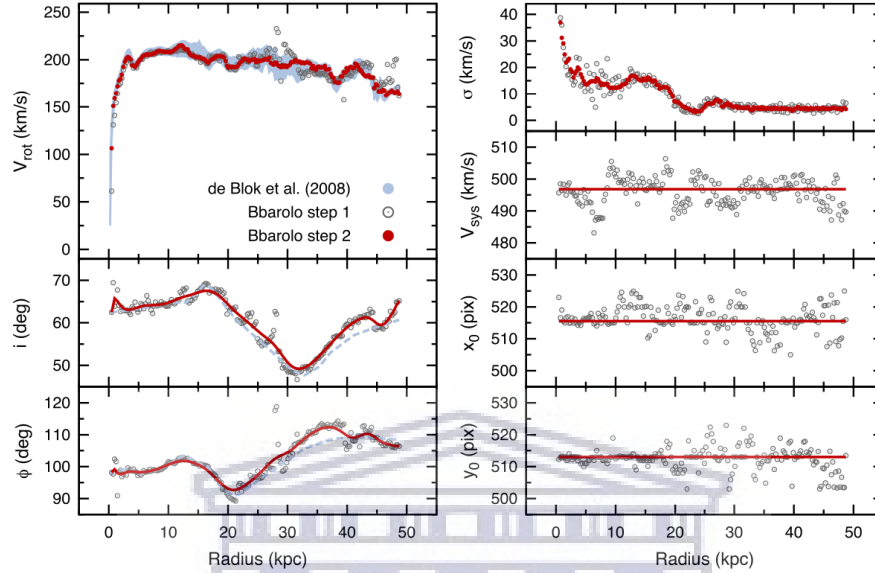


Figure 20: These are the parameters determined by  $3^{\text{D}}$ BAROLO with the input data cube of galaxy NGC 5055 from the THINGS survey. The right-hand panels starting from the top: velocity dispersion, systemic velocity, and the dynamical central points. The left-hand panels starting from the top: rotation curve, inclination, and position angle. Data in grey dots presents the results for the first iteration where all parameters were set to be free. The red lines and dots present the results for when only the rotation velocity and dispersion velocity were set to be free. The cyan lines and shadows present rotation curves derived with a 2D algorithm by De Blok et al. (2008).

#### 4.2.2 Mid-low resolution data

A 2D algorithm is highly affected by beam smearing in the case of low-resolution data, which is not an issue for  $3^{\text{D}}$ BAROLO. An example of this is the Westerbork HI survey of Irregular and Spiral galaxies Project (WHISP; Van der Hulst et al., 2001). Teodoro et al. (2015) chose 32 galaxies that already had the existing rotation curves derived by Swaters et al. (1999). Swaters determined the initial rotation curves for each galaxy by fitting the rotation velocity, inclination,

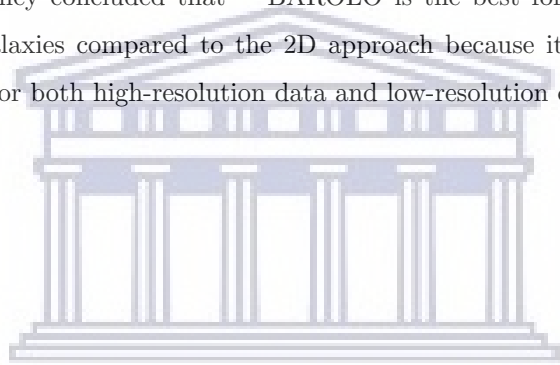
and position angle to six position velocity profiles with different angles. For their work, they used the INSPECTOR routine which is a Groningen Image Processing System (GIPSY; Ruiz et al., 2009) package. GIPSY is a software used to analyze 3D data and study the HI in galaxies. They fixed their central points to the optical values, and then they fitted the tilted-ring model to obtain the systemic velocity. Swaters further derived a 3D model using GALMOD in GIPSY and compared it to the observations.

Teodoro et al. (2015) used the same sample of 32 galaxies. The systemic velocity and the central points were estimated by the algorithm, which were used as the fixed <sup>3D</sup>BAROLO parameters. Their parameters values were almost equal to the ones obtained by Swaters, with only a slight deviation. Their inclination angle and position angle were adopted from Swaters. The first iteration of <sup>3D</sup>BAROLO was done by fitting the rotation velocity, dispersion velocity, inclination angle, and position angle. The second iteration was done by fitting only the rotation velocity and dispersion velocity while fixing the inclination and position angle. Figure 21 shows the rotation curves they obtained and the rotation curves obtained by Swaters. When comparing their rotation curves to Swaters rotation curves, they noticed that some galaxies at small radii had their rotation curves rise more steeply than Swaters rotation curves. This mid-low resolution case shows that <sup>3D</sup>BAROLO can work with low-resolution data cubes and also noisy data cubes.

#### 4.2.3 Very low resolution data

For the very-low resolution data case, Teodoro et al. (2015) shows how beam smearing affects derivations of rotation curves when using both the 2D and 3D algorithms. They used HI data of nearby galaxies observed with single-dish telescopes to derive rotation curves using ROTCUR for 2D analysis and <sup>3D</sup>BAROLO for 3D analysis. They used a very small sample of 4 galaxies observed with single-dish telescopes and had the same sample in high resolution.

The low-resolution rotation velocities and dispersion velocities were derived from 2D and 3D algorithms and compared to the high-resolution rotation velocities and dispersion velocities derived with <sup>3D</sup>BAROLO. For the 2D technique, the rotation curves were obtained by setting only the rotation velocity to be free and fixed other parameters. For <sup>3D</sup>BAROLO, they let the rotation velocity and the dispersion velocity be free and fixed other parameters. They concluded that the 2D algorithm is not meant for low-resolution data because of beam smearing effects when deriving 2D maps. <sup>3D</sup>BAROLO takes beam smearing into account. They concluded that <sup>3D</sup>BAROLO is the best for studying the kinematics of galaxies compared to the 2D approach because it gives correct rotation curves for both high-resolution data and low-resolution data.



UNIVERSITY *of the*  
WESTERN CAPE

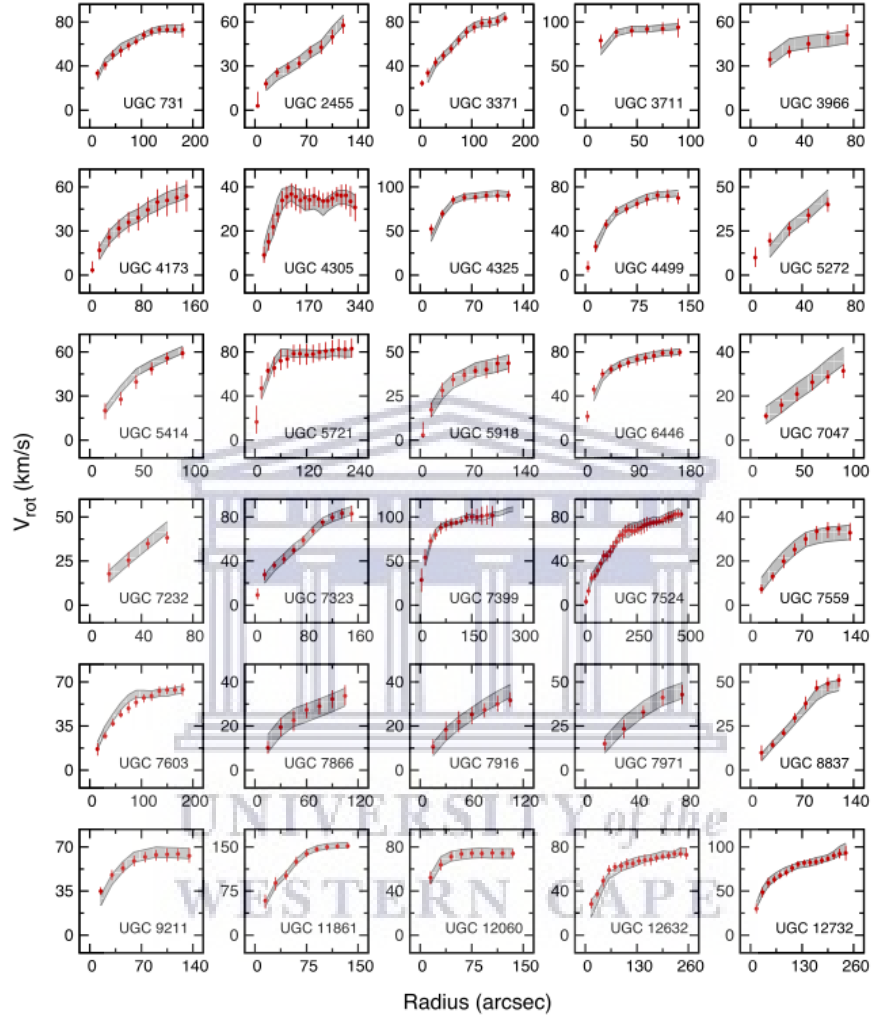


Figure 21: Rotation curves of the 30 dwarf late-type galaxies selected from the WHISP sample (other 2 galaxies did not produce good models). Rotation curves derived by Swaters et al. (1999) are presented with grey shadows. Rotation curves derived with  $3^{\text{D}}$ BAROLO are presented in red dots.



### 4.3 Fitting procedure for IC 4710

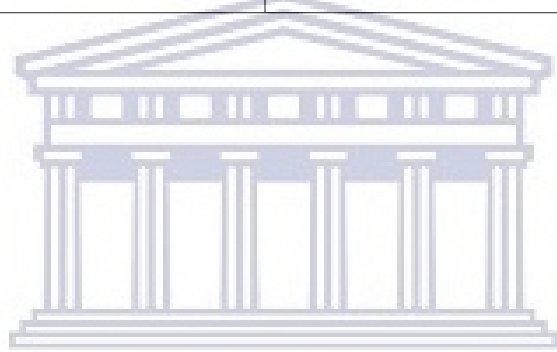
The steps below were followed in order to use <sup>3D</sup>BAROLO to fit a tilted ring model to the ATCA HI data cube of IC 4710. The initial values for the parameters mentioned below must be given to obtain a well-fitted model. Table 1 mentions the initial values used for all the mentioned parameters. The estimated initial dynamical central points ( $X_o$ ,  $Y_o$ ) were obtained from displaying the data cube in kvis software (Gooch, 1995). Kvis is a software that views images and movies. It can take in many datasets at the same time and return many profiles, it can overlay contours and many other functions. The initial estimate of the systemic velocity was obtained from the HI global profile of the galaxy presented in Chapter 2. The inclination and position angles were determined by overlaying the ellipse on the HI total intensity map and using Eqn. 1 in Chapter 2 to obtain the initial estimate for the inclination angle. This inclination angle was used to determine the rotation velocity through  $V_{rot} = W_{50}/2\sin(i)$ , where  $W_{50}$  is the width of the HI spectrum at a flux level of 50% obtained in chapter 2. This rotation velocity was also used as an initial estimate. Six iterations were done to fit the tilted-ring model:

- Step 1 - We started by setting all parameters to be free, and the results are shown in Fig. 22. Observing the 5th and 8th panels of Fig. 22, the straight horizontal lines indicate the values for  $X_o$  and  $Y_o$ , and their values are consistent with the estimated values which were obtained from kvis software.
- Step 2 - This iteration focuses on fixing the central dynamical points ( $X_o$  and  $Y_o$ ). The points were fixed to the estimated initial points shown in Table 1, and the results are shown in Fig. 23. Analysing the last panel in Fig. 23 which shows the systemic velocity profile, we notice the systemic velocity to be approximately equal to the systemic velocity that was obtained in Chapter 2.

- Step 3 - This iteration focuses on fixing the systemic velocity ( $V_{\text{sys}}$ ), which was obtained from Eqn. 5, with the results shown in Fig. 24. A good model is not yet achieved. analysing the 6th panel, which is the radial velocity profile, we notice the radial velocity to be varying around  $3 \text{ km s}^{-1}$ . So for the next iteration, the radial velocity is fixed to that value. The position angle, inclination angle,  $V_{\text{rot}}$  and  $V_{\text{rad}}$  were still set as free parameters.
- Step 4 - The radial velocity is now fixed to  $3 \text{ km s}^{-1}$  which was obtained from the previous step. Figure 25 shows results where the radial velocity is fixed. Position angle, inclination angle, and rotation velocity vary with radius. The 4th and 7th panels were analysed and it was noticed that the position angle varies around 45 degrees and the inclination angle varies around 30 degrees.
- Step 5 - We set the position angle to 45 degrees, with results shown in Fig. 26. The inclination angle at this point varies with radius, and it ranges around 30 degrees.
- Step 6 - The inclination angle from the previous step is similar to the estimated initial value. So the last step focuses on fixing the inclination angle to get a good model. Figure 27 shows the final results after all the iterations. The rotation velocity, dispersion velocity, and gas column density were set free throughout all the iterations. Figure 27 shows our final tilted ring model.

Table 1: Initial <sup>3D</sup>BAROLO parameters for IC 4710.

<b><sup>3D</sup>BAROLO parameters</b>	<b>Initial estimates</b>
X <sub>o</sub>	126 pixels
Y <sub>o</sub>	123 pixels
V <sub>sys</sub>	737 km s <sup>-1</sup>
Inclination angle	30 degrees
PA	45 degrees
V <sub>rot</sub>	45 km s <sup>-1</sup>



UNIVERSITY *of the*  
WESTERN CAPE

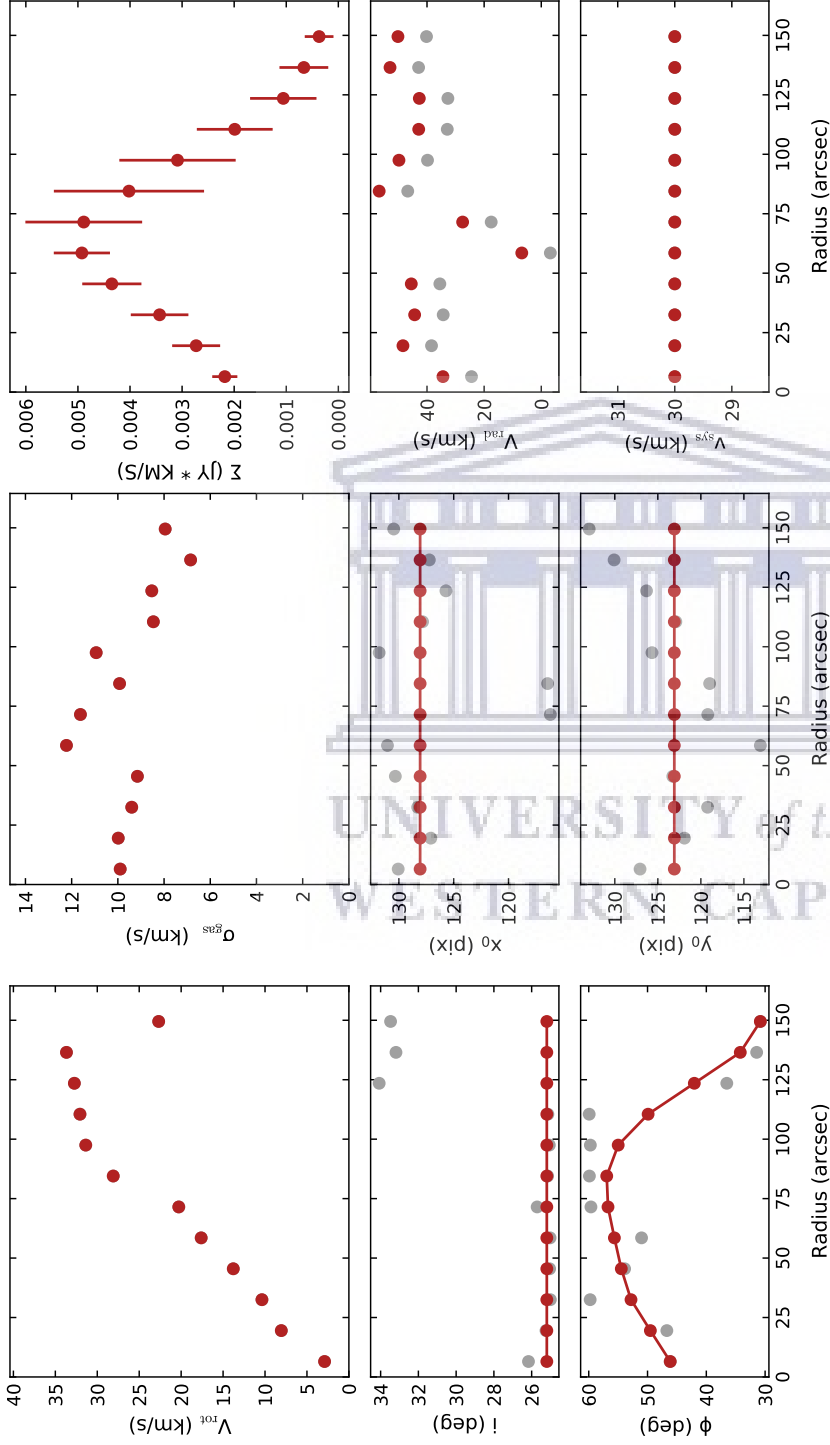


Figure 22: The figure presents the results for the first step where all the parameters were set to be free. The first row presents the rotation velocities, dispersion velocities, and gas column densities. The second row shows the inclination angles, X central points, and radial velocities. The last row shows the position angles, Y central points, and systemic velocities. The straight lines shown in the inclination angle, central dynamical points, and systemic velocity profiles are the values that <sup>3D</sup>BAROLO fixed the parameters to. The rotation velocities, dispersion velocities, column densities, radial velocities, and position angles vary freely with radius. The grey dots represent the results with errors, and the red dots represents the true results.

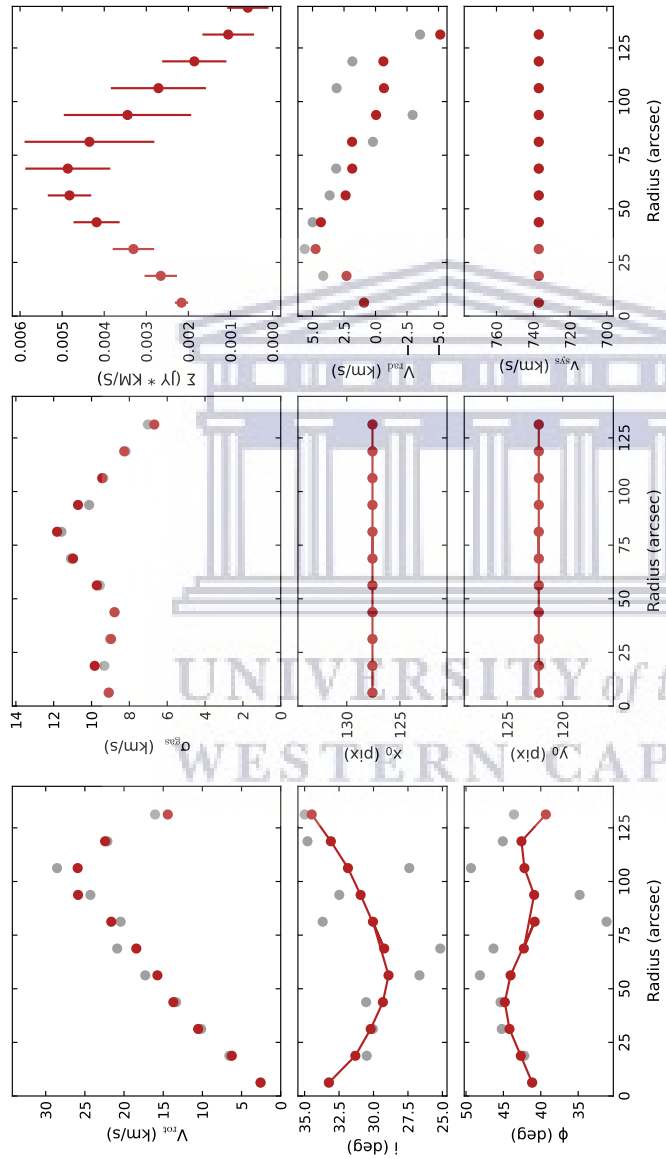


Figure 23: Step 2 results where  $X_0$  and  $Y_0$  are fixed. The panels are arranged the same way as Fig. 11. The straight lines in the dynamical central points profile are due to fixing the parameters to the initial estimate values. The other parameters are varying freely with the radius. The grey dots represent the results with errors and the red dots represents the true results.

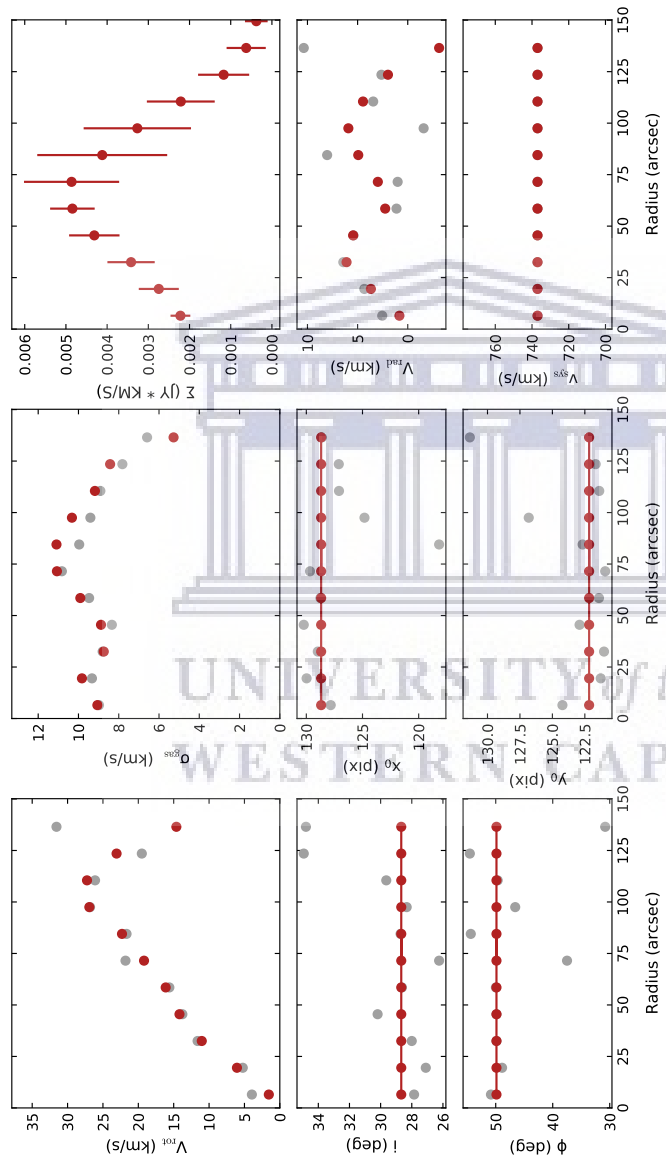


Figure 24: Step 3 results where the systemic velocity is fixed. The panels are arranged the same way as Fig. 11. The straight lines are due to the fixed initial estimates, whereas the other parameters are varying freely with radius. The grey dots represent the results with errors and the red dots represents the true results.

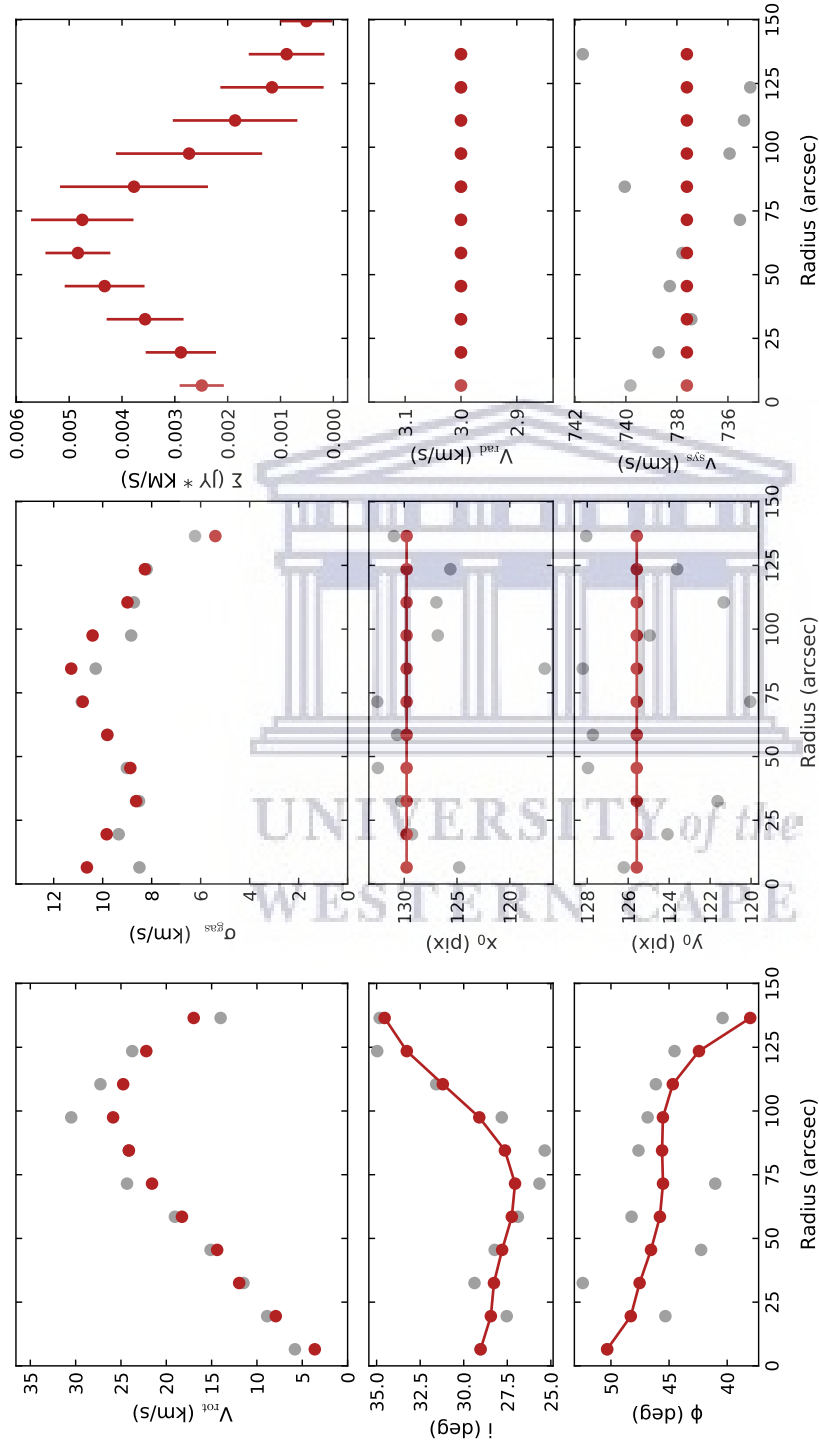


Figure 25: Step 4 results where  $V_{rad}$  is fixed. The panels are arranged the same way as Fig. 11. The straight lines are due to the fixed initial estimates, whereas the other parameters are varying freely with radius. The grey dots represent the results with errors and the red dots represents the true results.

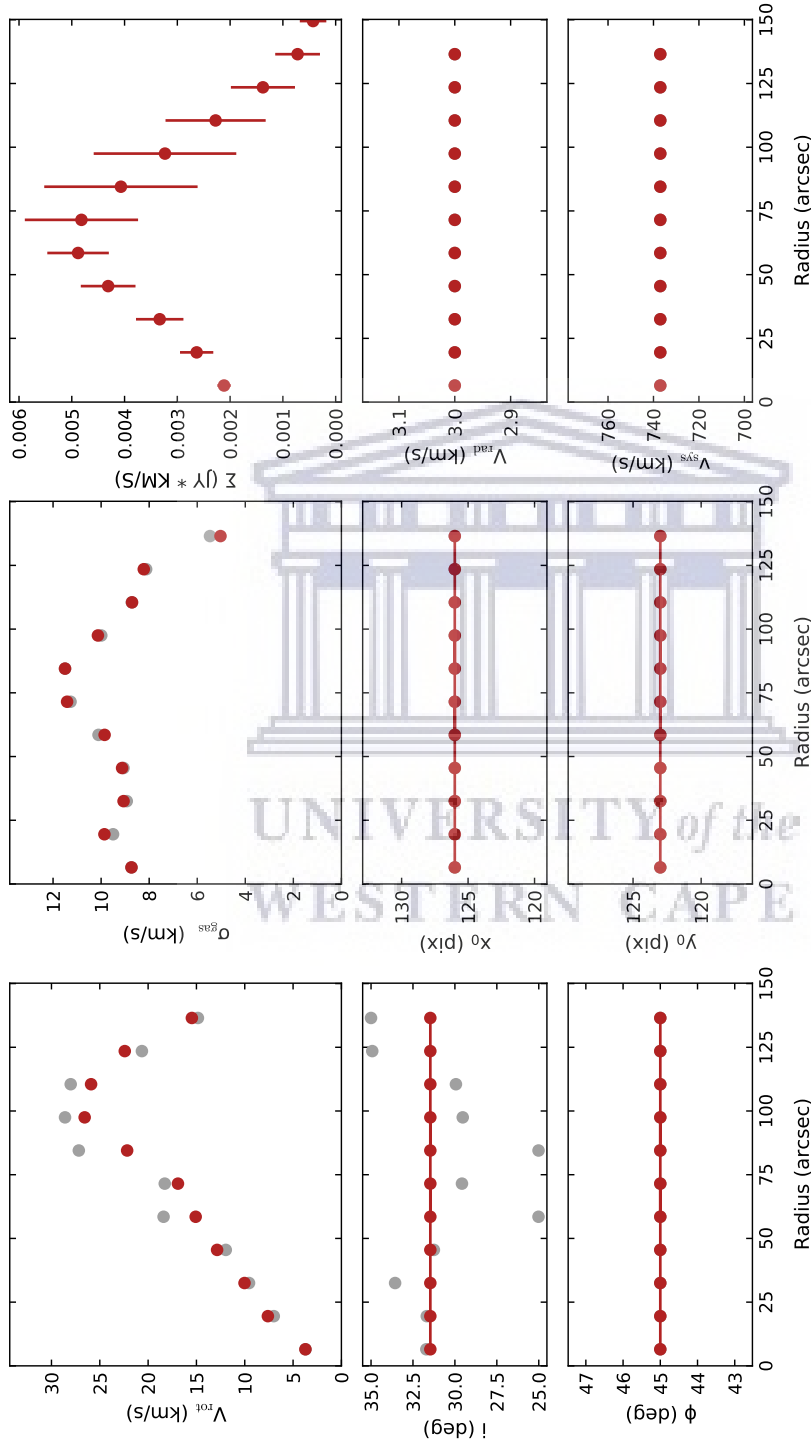


Figure 26: Step 5 results where PA is fixed. The panels are arranged the same way as Fig. 11. The straight lines are due to the fixed initial estimates, whereas the other parameters are varying freely with radius. The grey dots represent the results with errors and the red dots represents the true results.



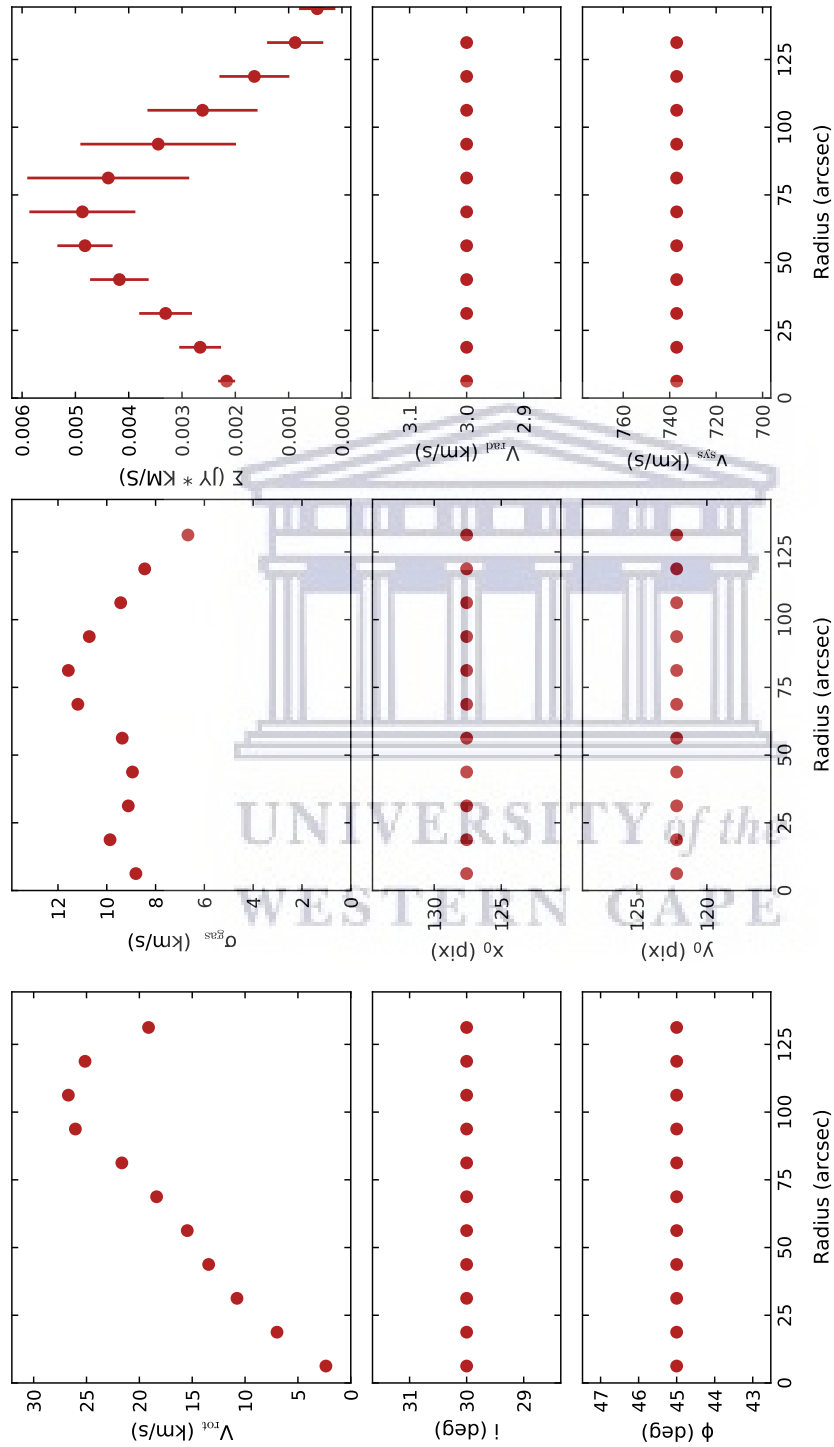


Figure 27: Step 6 results where the inclination angle is fixed. The panels are arranged the same way as Fig. 11. The straight lines are due to the fixed initial estimates, whereas the other parameters are varying freely with radius.

#### 4.4 Rotation curve

The top-left panel in Fig. 27 shows the final rotation curve from <sup>3D</sup>BAROLO. This rotation curve was obtained after the 6th iteration of the 3D algorithm technique. The inclination angle from <sup>3D</sup>BAROLO is 30 degrees, which is similar to the inclination angle obtained by overlaying the ellipse on the HI intensity map in Chapter 2. The rotation curve is rising steeply until it reaches the maximum rotation velocity of 24.6 km s<sup>-1</sup> and at a radius of 100 arcsec. This maximum rotation velocity is greater than the maximum velocity (24.6 km s<sup>-1</sup>) that was estimated from W<sub>50</sub> in Chapter 2. After the maximum point, the rotation velocities decrease.

Oh et al. (2015) presents rotation curves of 26 nearby dwarf galaxies obtained from Very Large Array (VLA) and *Spitzer* IRAC 3.6  $\mu\text{m}$  images. They discovered that the rotation curves of their galaxies are rising linearly at small radii, which shows that the mass distribution at small radii is nearly constant. They further mentioned that their discovery is common for most nearby dwarf galaxies. Relating their work to our rotation curve shown in the first panel in Fig. 27, the rotation curve of IC 4710 takes the general shape of the rotation curves of other nearby dwarf galaxies.

#### 4.5 Model and data comparison

This section focuses on checking if the obtained dynamical model in Fig. 27 is correct. This process of checking accuracy is done by comparing the model data to the input data. The comparison was performed by superimposing the model data contours and the ATCA data contours on the <sup>3D</sup>BAROLO model channel maps. If there is a match between the model data and the original data, the model data contours should detect emissions from the data cube. The comparison of the model data and ATCA data is shown in Fig. 28. The level of agreement between the model and the data is high.

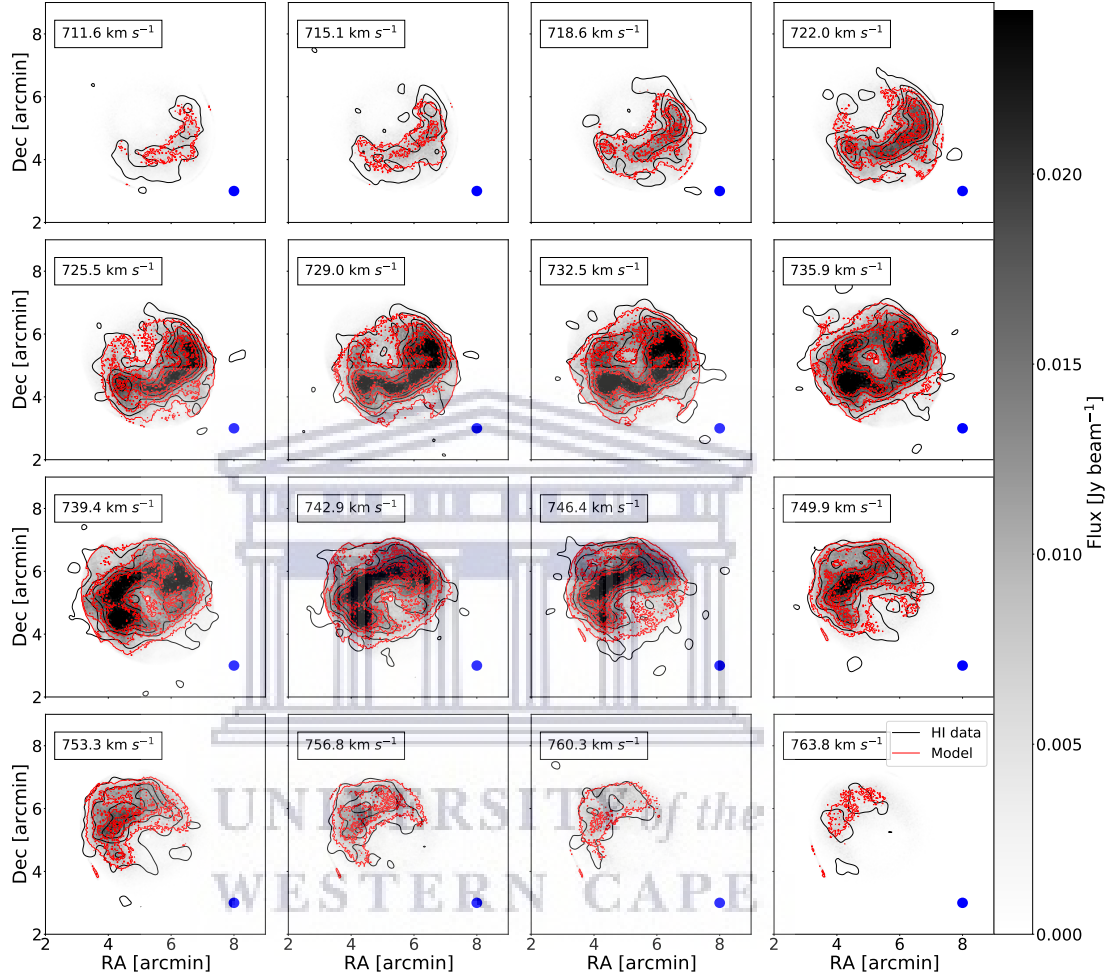


Figure 28: Model channel maps from  $3^{\text{D}}\text{BAROLO}$  (Greyscale ranges from 0 to  $27\sigma$ , where  $\sigma = 0.909 \text{ mJy beam}^{-1}$ ). This  $\sigma$  was obtained from the line-free channel in Chapter 2. The velocity width of each channel is  $3.5 \text{ km s}^{-1}$  and the velocity for each channel is at the top left corner of each panel. The model contours are shown in red at levels of 5 to  $20 \text{ mJy beam}^{-1}$  in steps of  $5 \text{ mJy beam}^{-1}$ . The HI data contours are shown in black at levels of 5 to  $20 \text{ mJy beam}^{-1}$  in steps of  $5 \text{ mJy beam}^{-1}$ . The synthesized beam of  $26.9 \text{ arcsec} \times 25.7 \text{ arcsec}$  is shown in blue at the bottom right corner of each panel.

To quantify the degree of agreement of the <sup>3D</sup>BAROLO model and the ATCA data cube, we compared the two products on a channel by channel basis. For each channel, the model was subtracted from the data, and the residuals were histogrammed. The histograms are shown in the right-hand panels of Fig. 29. The distributions of residuals are approximately Gaussian distributed, centered on zero. For each distribution, we calculated the standard deviation in units of mJy/beam, and then converted the result to units of  $M_{\odot} \text{ pc}^{-2}$ . The average of all the calculated standard deviations is  $0.073 M_{\odot} \text{ pc}^{-2}$ , suggesting that the <sup>3D</sup>BAROLO model is a good representation of the ATCA data cube.



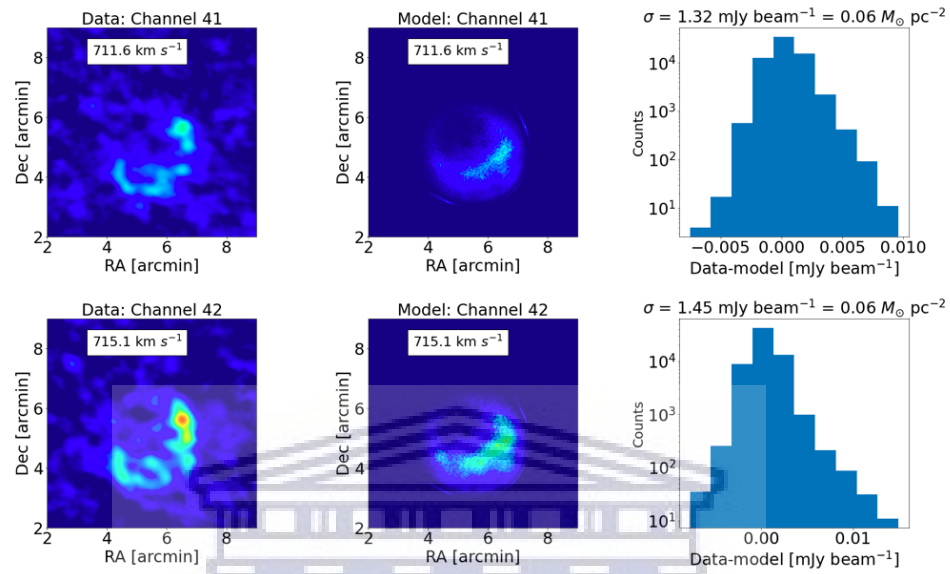


Figure 29: HI data channel maps on the left-hand side of the figure, model channel maps at the middle and residuals in the form of histograms on the right-hand side. The model and data channel maps are in jet scale, ranging from 0 to  $27\sigma$ , where  $\sigma = 0.909 \text{ mJy beam}^{-1}$ . This  $\sigma$  was obtained from the line-free channel in Chapter 2. The velocity for each channel is at the top left corners of each panel. Standard deviations of each residual is shown on top of each histogram.

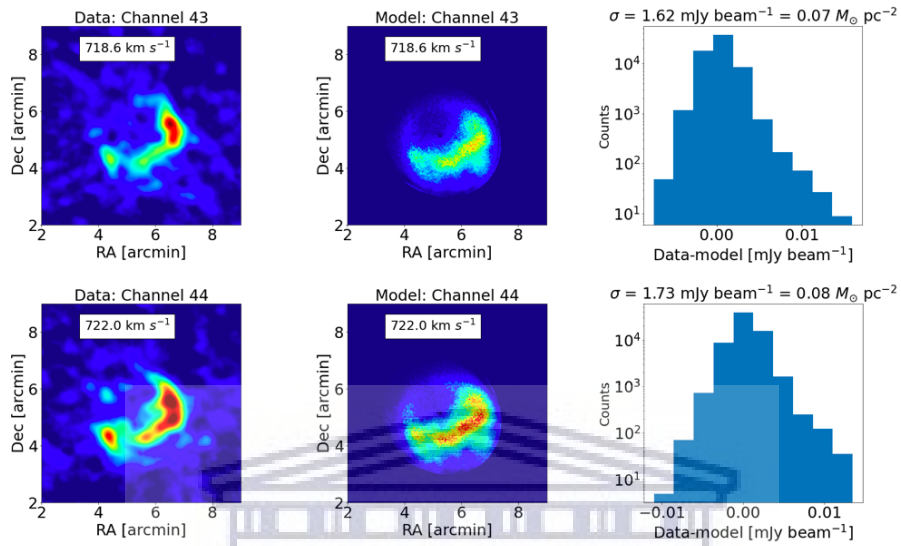


Figure 30: Fig. 28 continued.

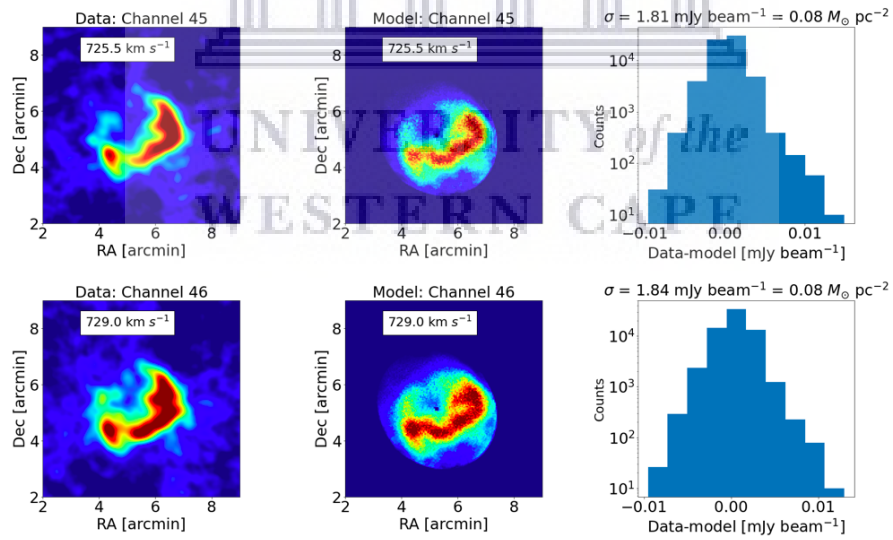


Figure 31: Fig. 28 continued.

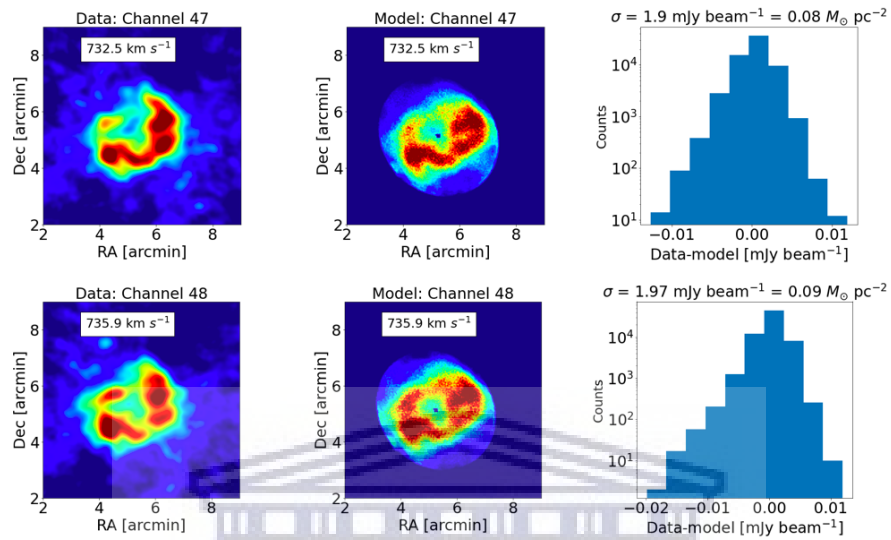


Figure 32: Fig. 28 continued.

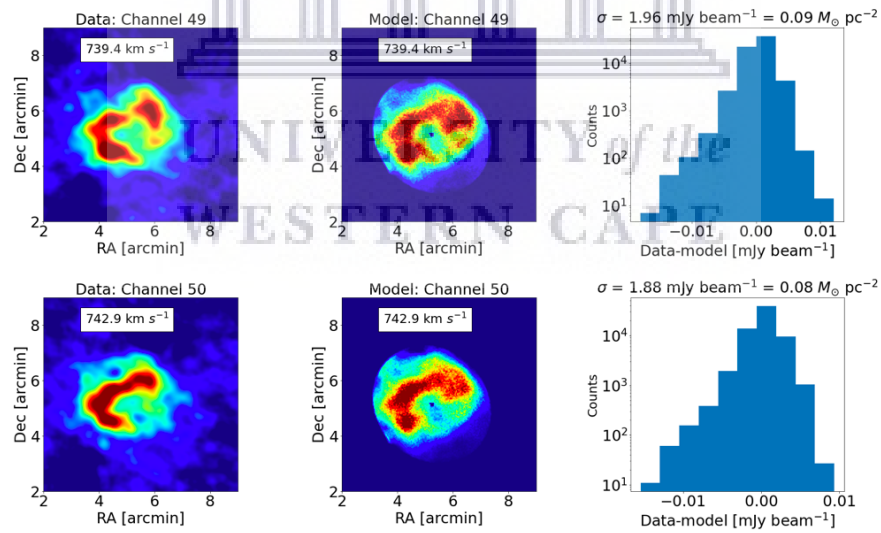


Figure 33: Fig. 28 continued.

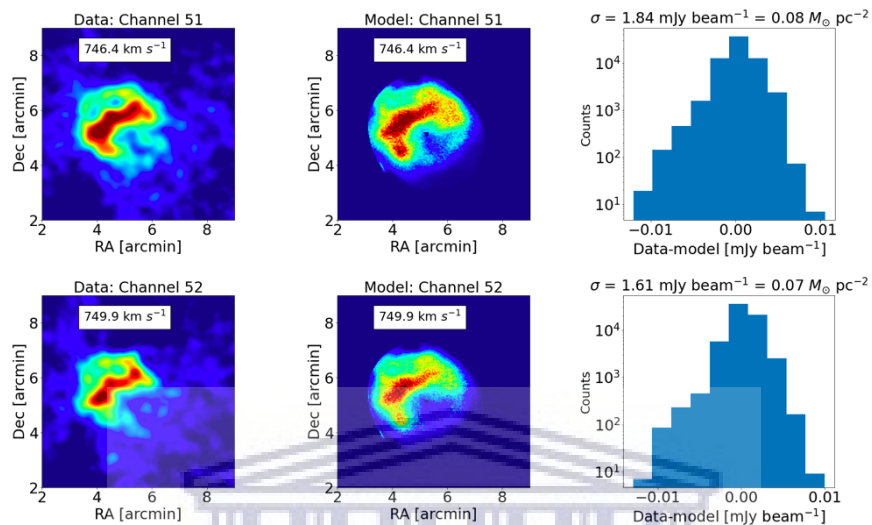


Figure 34: Fig. 28 continued.

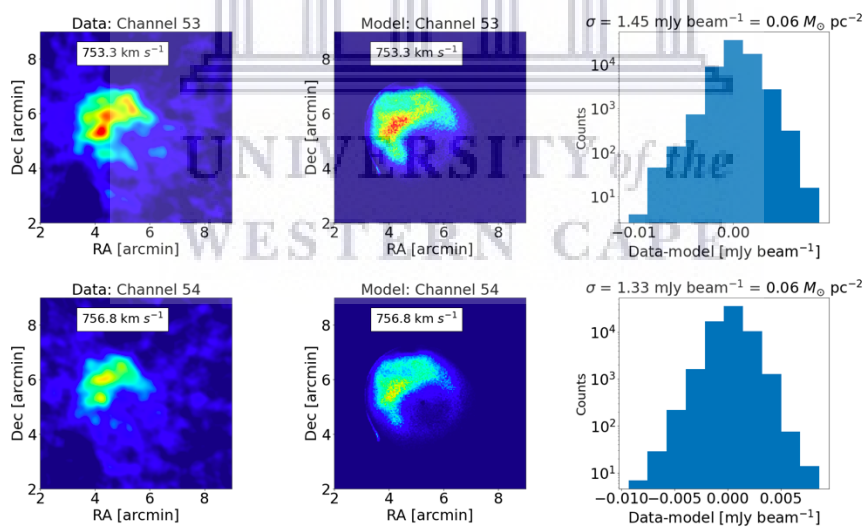


Figure 35: Fig. 28 continued.



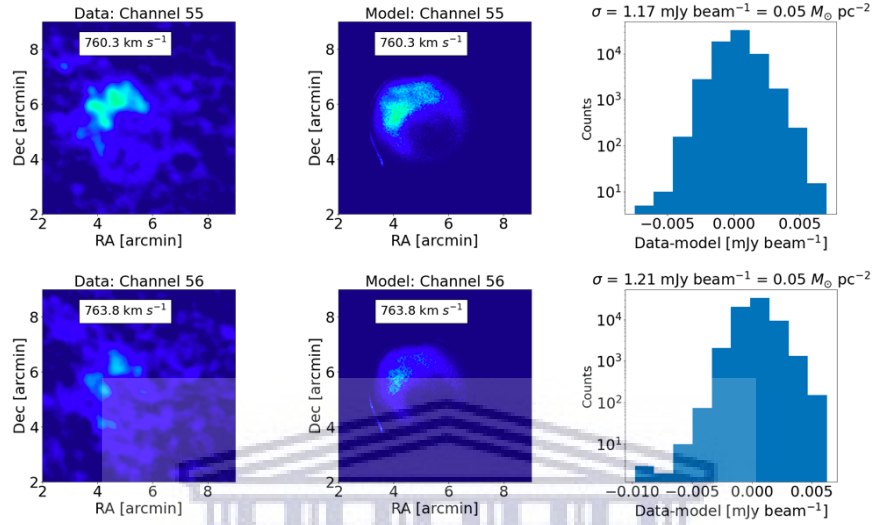


Figure 36: Fig. 28 continued.

In Fig. 37 we give the standard deviation of each channel as a function of the corresponding velocity of each channel. The standard deviations and velocities are also given on the plots in Fig. 29-36. Figure 37 allows us to check the model accuracy and compare it to the data. The shape of the figure shows that the standard deviation is roughly constant, which implies that the model and data are in good agreement. However, there is a slight increase in standard deviation at channel velocity around  $740 \text{ km s}^{-1}$  which is almost equal to the systemic velocity ( $V_{\text{sys}} = 737 \text{ km s}^{-1}$ ), this is expected since channels with more emission should have a higher deviation (observed on channel maps in Fig. 29).

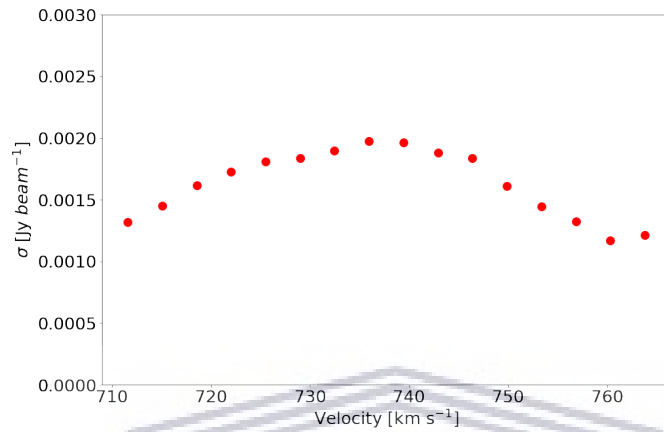


Figure 37: A plot of standard deviation of the residuals obtained from subtracting the <sup>3D</sup>BAROLO model from ATCA cube.

UNIVERSITY of the  
WESTERN CAPE

## 4.6 Asymmetric drift correction

Asymmetric drift ( $V_A$ ) is the difference between the circular velocity and the mean rotational velocity of a stellar population.  $V_A$  correlate with the observed rotational velocities corrected by the reflex motion of the sun (Golubov et al., 2013). Steps followed to derive circular velocities from observed rotation velocities are mentioned in this section.

The momentum equation below gives the radial component which relates the rotation velocity to the galactic gravitational potential ( $\Phi$ ), whereby gas is assumed to be at equilibrium (Iorio et al., 2016):

$$\frac{1}{\rho} \frac{\partial \rho \sigma_v^2}{\partial R} = -\frac{\partial \Phi}{\partial R} + \frac{V_{\text{rot}}^2}{R}, \quad (17)$$

where  $\sigma_v$  is the velocity dispersion and  $\rho$  is the volumetric density of the gas. Then by re-writing Eqn. 17, we get:

$$V_c^2 - V_{\text{rot}}^2 = -\frac{R}{\rho} \frac{\partial \rho \sigma_v^2}{\partial R} = -R \sigma_v^2 \frac{\partial \ln(\rho \sigma_v^2)}{\partial R} = V_A^2, \quad (18)$$

where  $V_c = \sqrt{\frac{R \partial \Phi}{\partial R}}$  is the circular velocity, and  $V_A$  is the asymmetric drift. The asymmetric drift is much more significant at a larger radius because the larger the radius, the larger the asymmetric drift (refer to Eqn. 18), and it depends on the velocity dispersion (Golubov et al., 2013). In spiral galaxies, asymmetric drift correction is negligible (De Blok et al., 2008). Asymmetric drift correction is not essential in most dwarf irregular galaxies because the rotation velocity and dispersion velocity are approximately equal.

The volumetric density (where  $z = 0$ ) and the ratio of the intrinsic surface density and the scale height are proportional to each other. Then it gives the asymmetric drift as:

$$V_A^2 = R \sigma_v^2 \frac{\partial \ln(\sigma_v^2 \Sigma_{\text{int}} z_d^{-1})}{\partial R}, \quad (19)$$

where  $z_d$  is the scale height. The radial derivative of  $z_d$  is then ignored, as the thickness of the gaseous layer is assumed to not depend on the radius. The HI disc is also assumed to be thin, and the ratio of the intrinsic surface density and the observed surface density is given by the cosine of the inclination angle ( $i$ ). These conditions give the classical formula for the asymmetric drift correction as given below:

$$V_A^2 = -R\sigma_v^2 \frac{\partial \ln(\sigma_v^2 \Sigma_{\text{obs}} \cos(i))}{\partial R}. \quad (20)$$

Iorio et al. (2016) studied the HI kinematics of 17 dwarf irregular galaxies from LITTLE THINGS and used <sup>3D</sup>BAROLO to fit the tilted-ring models. They ignored  $\cos(i)$  for galaxies with a constant inclination angle. They used  $\cos(i)$  only for DDO 168, NGC 1569, and UGC 8508.

<sup>3D</sup>BAROLO can correct for asymmetric drift, so in this work we used it. We applied the asymmetric drift correction to the observed rotation velocities to derive the circular velocities assuming the dispersion velocity to be 8 km s<sup>-1</sup>, and the results are shown in Fig. 38. Figure 38 presents the comparison between the observed rotation curve from <sup>3D</sup>BAROLO and the derived circular velocities. The observed velocities are higher (excluding at radius  $\sim 35$  arcsec) as compared to the circular velocities, but the circular velocities give a smooth increasing curve, whereas the observed rotation velocities are inconsistent.

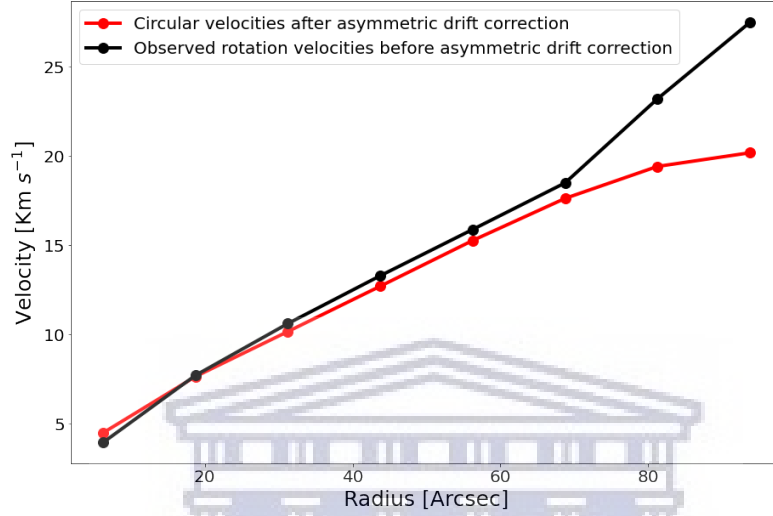


Figure 38: Comparison between the observed rotation curve from <sup>3D</sup>BAROLO and the derived circular velocities

#### 4.7 Mass modeling

Dwarf galaxies are dark matter dominated, although the impact of baryons can still be significant. To derive the distribution of dark matter, we need to take into account the mass contributions from the gas component and stellar component (De Naray et al., 2008).

In this section, we model the distribution of dark matter in IC 4710 as an isothermal sphere in order to constrain its parameters. We derive our best model for the total rotation velocities by adding the dynamical components in quadrature as follows (De Blok et al., 2008):

$$V_{\text{tot}}^2 = \Upsilon_{\text{star}} V_{\text{star}}^2 + V_{\text{gas}}^2 + V_{\text{DM}}^2, \quad (21)$$

where  $V_{\text{gas}}$  is the rotation curve of the gas component,  $V_{\text{DM}}$  is the rotation curve of the dark matter component that will be modeled as an isothermal

sphere.  $V_{\text{star}}$  is the rotation curve of the stellar component and  $\Upsilon_{\text{star}}$  is the stellar mass-to-light ratio. In this work, three different stellar mass-to-light ratios were assumed.

#### 4.7.1 Gas distribution

<sup>3D</sup>BAROLO's measure of the azimuthally-averaged gas surface densities in IC 4710 were used to calculate the contribution of HI to the galaxy's total rotation curve. In order to do this, the profile was used to calculate the cumulative mass as a function of radius through Eqn. 22, where  $\Sigma_R$  is the HI surface density profile,  $R$  is the radius,  $R_{\text{min}}$  (0 kpc) is the minimum radius, and  $R_{\text{max}}$  (3.5 kpc) is the maximum radius. The gas surface density profile is presented in Fig. 39 and the HI cumulative mass curve is presented in Fig. 40. Knowing the mass within a particular radius, Newton's laws (Eqn. 23) were used to calculate the rotation velocity of the gas at that radius, where  $G$  is the gravitational constant,  $R$  is the radius and  $M(<R)$  is the cumulative mass. The resulting rotation curve is shown in Fig. 41.

$$M(<R) = \int_{R_{\text{min}}}^{R < R_{\text{max}}} 2\pi \Sigma_R \cdot R \cdot dR \quad (22)$$

$$V(R) = \sqrt{\frac{GM(<R)}{R}} \quad (23)$$

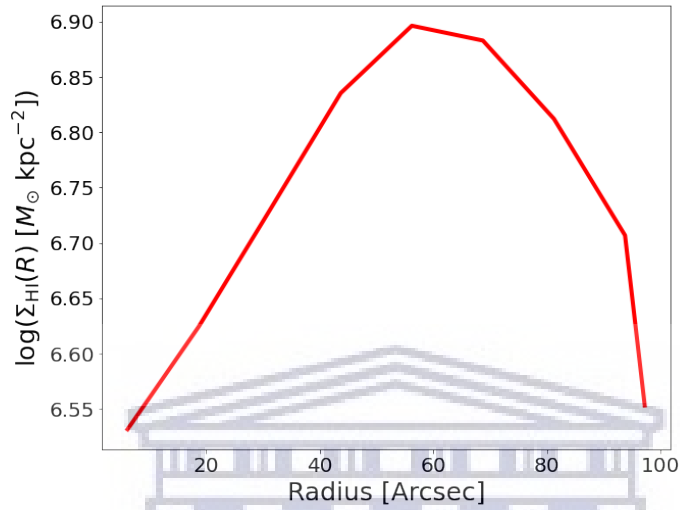


Figure 39: The azimuthally-averaged HI surface density as a function of radius.

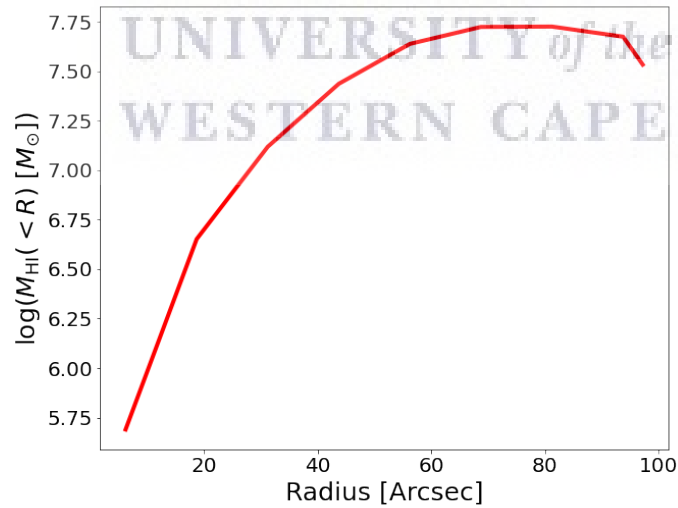


Figure 40: The HI cumulative mass curve of IC 4710 derived from the HI surface densities.

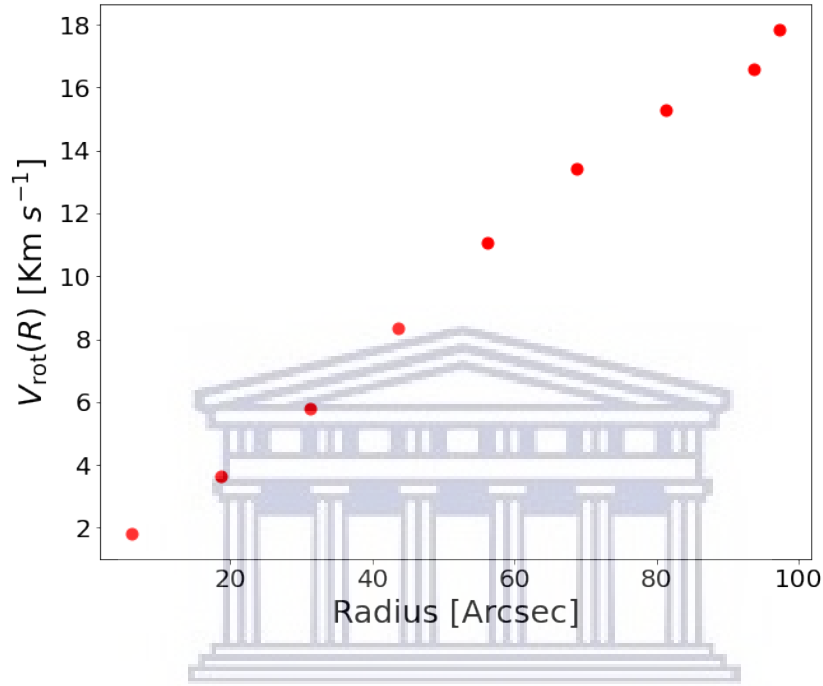


Figure 41: The rotation velocities of HI components in IC 4710. This rotation curve was derived from Fig. 39. Each red dot presents the rotation velocity at a certain radius, and they are derived from using Eqn. 23.

Relating our work to literature, [Oh et al. \(2015\)](#) determined the gas rotation velocities by using the total integrated HI intensity maps (moment 0) of the dwarf galaxies from Local Irregulars That Trace Luminosity Extremes, The HI Nearby Galaxy Survey (LITTLE THINGS). The total integrated HI intensity maps were used to obtain the mass models for the gas contributions. They then obtained the gas surface density profiles by fitting the 2D tilted-ring models to the total integrated HI intensity maps, with a scaling factor of 1.4 which accounts for helium and metals. The gas surface density profiles were then converted into gas rotation velocities while assuming that most of the gas is distributed in a thin disc. The derived gas surface density profile and the gas rotation curve of the dwarf galaxy CVnIdwA from LITTLE THINGS can be



seen in bottom two panels of Fig. 42.

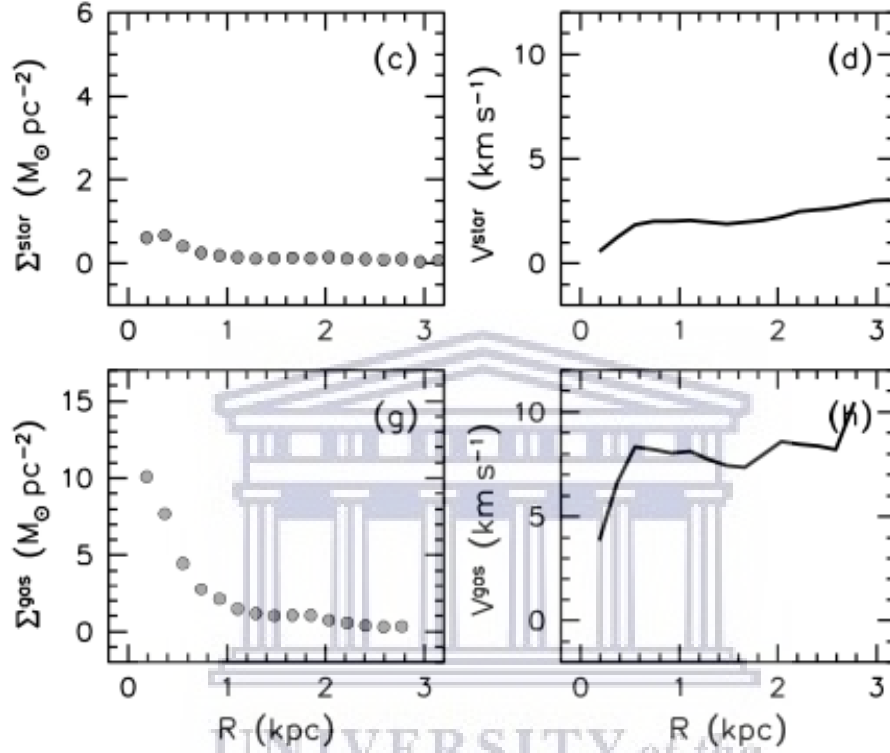


Figure 42: The gas surface density profile (left) and the gas rotation curve(right) of dwarf galaxy CVnIdwA from LITTLE THINGS derived by Oh et al. (2015).

The shape of our gas surface density profile is different from the gas surface density profile derived by Oh et al. (2015). The differ because IC 4710 has a prominent central depression of HI. The HI rotation velocities of our galaxy are higher than those derived by Oh et al. (2015) for dwarf galaxy CVnIdwA, and this means that our galaxy contains more HI than CVnIdwA. The rotation curves are also not similar but they are both steeply increasing at lower radii, and they both indicate that there is more gas at larger radii than it is at lower radii.

### 4.7.2 Stellar distribution

In order to quantify the gravitational contribution of stars to the measured rotation curve of IC 4710, we adopted the far-infrared total luminosity ( $L_* = 10^{8.16} L_\odot$ ) of the galaxy from [Smith et al. \(2007\)](#) and assumed three stellar mass-to-light ratios to derive the stellar rotation velocities. We looked at the literature for typical mass-to-light ratios ([Oh et al., 2008](#)), where values of  $\sim 0.3 M_\odot/L_\odot$  were often seen for dwarf galaxies, and we also tried the lower values than  $0.3 M_\odot/L_\odot$  as well. The mass profile was obtained through the following equation:

$$M_{\text{star}} = \Upsilon_{\text{star}} L_{\text{star}}, \quad (24)$$

where  $\Upsilon_{\text{star}}$  is the mass-to-light ratio. For this work, 3 different mass-to-light ratios were assumed ( $0.1 M_\odot/L_\odot$ ,  $0.2 M_\odot/L_\odot$ , and  $0.3 M_\odot/L_\odot$ ). Three corresponding stellar masses were calculated.

Assuming an exponential stellar disk, the total masses were used to calculate the central surface brightness using the following equation:

$$\Sigma_o = \frac{M_{\text{star}}}{2\pi h^2}, \quad (25)$$

where  $M_{\text{star}}$  is the stellar mass, and  $h = 1.5$  kpc is the scale length in i-band adopted from [Ryder et al. \(1994\)](#). The three central surface brightness measures are in units of  $M_\odot \text{ kpc}^{-2}$ . Then the stellar surface density profiles which are in the units of  $M_\odot \text{ pc}^{-2}$ , are calculated as:

$$\Sigma_* = \Sigma_o \exp\left(\frac{-R}{h}\right), \quad (26)$$

where  $h$  is still the same adopted scale length, and  $R$  is the radius. These stellar surface densities were also calculated three times and plotted against the radius as shown in Fig. 43.

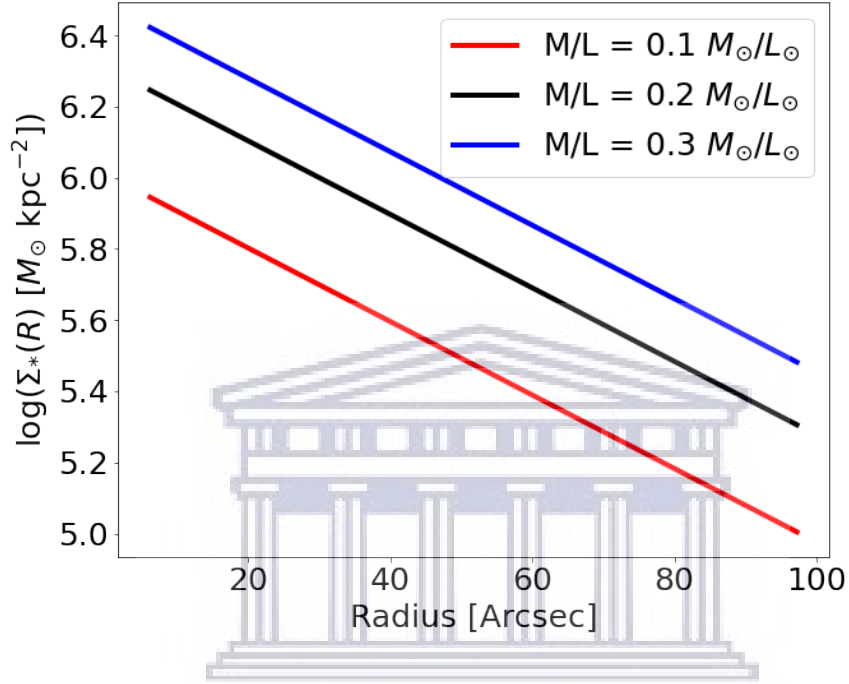


Figure 43: The stellar surface density profiles of IC 4710 generated from the infrared-band surface brightness profiles of Dale et al. (2017) assuming stellar mass-to-light ratios of  $0.1 M_\odot/L_\odot$ ,  $0.2 M_\odot/L_\odot$ , and  $0.3 M_\odot/L_\odot$ .

Having generated reliable stellar surface density profiles of IC 4710 from the infrared-band surface brightness profile of Dale et al. (2017) assuming the above-mentioned stellar mass-to-light ratios, we use them to derive the cumulative mass within a radius  $R$ . This was done through Eqn. 22 and the resulting cumulative stellar mass curves are presented in Fig. 44. These cumulative stellar mass curves were then converted into rotation velocities using Eqn. 23, and the corresponding rotation curves are shown in Fig. 45.

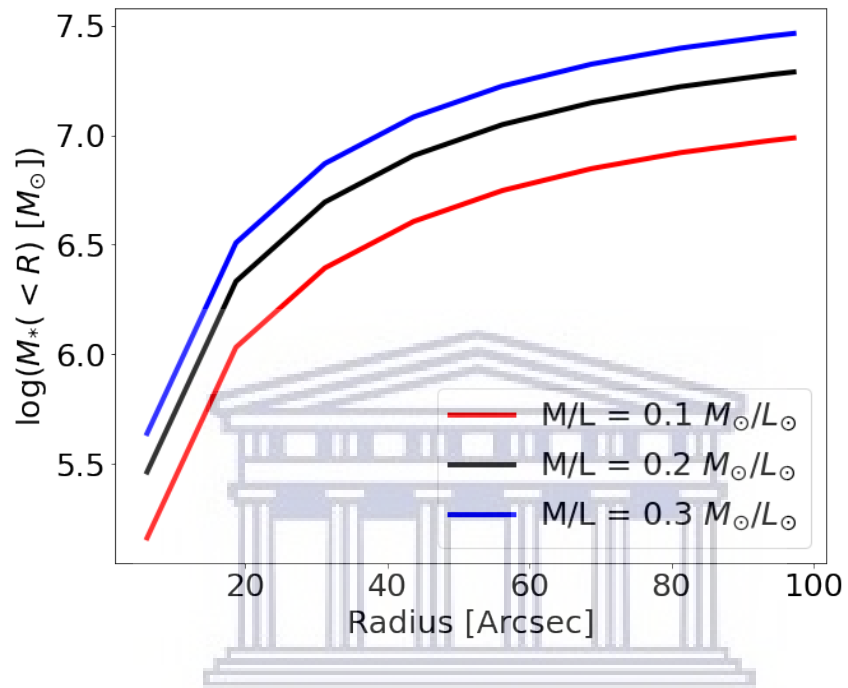


Figure 44: The cumulative stellar mass curves of IC 4710 assuming stellar mass-to-light ratios of  $0.1 M_\odot/L_\odot$ ,  $0.2 M_\odot/L_\odot$ , and  $0.3 M_\odot/L_\odot$ .

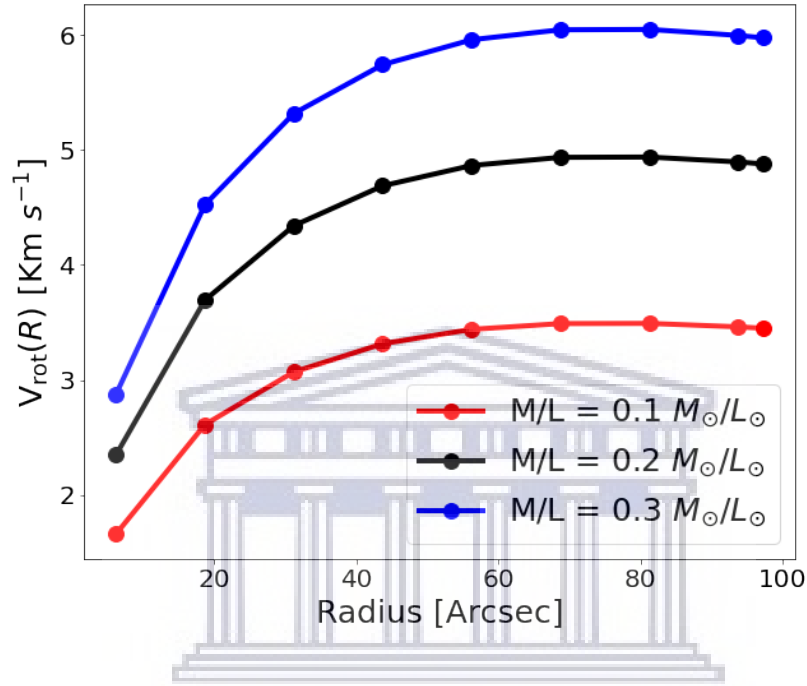


Figure 45: The stellar rotation curves of IC 4710 assuming stellar mass-to-light ratios of  $0.1 M_{\odot}/L_{\odot}$ ,  $0.2 M_{\odot}/L_{\odot}$ , and  $0.3 M_{\odot}/L_{\odot}$ .

Relating our stellar component results to literature, Oh et al. (2015) used the *Spitzer* IRAC  $3.6 \mu\text{m}$  images to calculate the circular velocities induced by the stellar mass distributions. They preferred using the *Spitzer* IRAC  $3.6 \mu\text{m}$  images due to the ways in which IR images are less affected (attenuated) by dust than optical images are. Another reason for choosing to work with the *Spitzer* IRAC  $3.6 \mu\text{m}$  images is that the NIR imaging traces the older stellar population, which constitutes the majority of the stellar mass. They derived the surface brightness profiles, and they further used the mass-to-light ratio values given by Oh et al. (2008) to convert the stellar surface brightness profiles to the stellar surface density profiles, which were then converted into the stellar rotation velocities. The derived stellar surface density profile and gas rotation curve of one of the dwarf galaxy CVnIdwA from LITTLE THINGS are shown

in the first and second panels of Fig. 42. Their results seem to be similar to the results of our dwarf galaxy IC 4710.

### 4.7.3 Dark matter distribution

Now that we have modeled the contributions from the HI and stars to the total gravitational potential, we are left with the dark matter contribution to the total rotation curve. It is important to derive the total rotation curve - that is, the sum of all three contributions - and compare it to the observed rotation curve. How well the two agree will determine the dark matter contribution. Many known models can be used for the analysis of dark matter distributions. Examples of the models are the Navarro-Frank-White (NFW; Navarro et al., 1996) and the pseudo-isothermal (ISO; Begeman et al., 1991) halo.

The NFW model was determined from the Cold Dark Matter (CDM) simulations. A cuspy density dominates these simulations and they are described by the following universal density profile:

$$\rho_{\text{NFW}}(R) = \frac{\rho_i}{(R/R_s)(1 + R/R_s)^2}, \quad (27)$$

where  $\rho_i = \frac{3H^2}{8\pi G}$  is the critical density,  $G$  is the gravitational constant, and  $H$  is the Hubble constant.  $R_s$  is the characteristic radius (sometimes called the scale radius) of the halo, when the radius becomes approximately equal to the characteristic radius, the profile becomes nearly isothermal (Navarro et al., 1996). This universal density profile is mostly used in accounting for dark matter distributions that show a steep rise towards the central halo region. The steepness is described by  $\rho \sim R^\alpha$ , where  $\alpha \propto -1$ . The mass distribution is derived from the universal density profile, which is then converted into the dark matter halo rotation velocities. The rotation velocities are derived by:

$$V_{\text{NFW}}(R) = V_{200} \sqrt{\frac{\ln(1+cx) - cx/(1+cx)}{x[\ln(1+c) - c/(1+c)]}}, \quad (28)$$

where  $c = R_{200}/R_s$ , is the concentration parameter.  $V_{200}$  is the rotation velocity at radius  $R_{200}$  and  $x = R/R_{200}$ . At radius  $R_{200}$ , the halo density is 200 times the critical density of the Universe.

Another way of describing the dark matter distribution is through the ISO halo model, which contains the constant density at the core of the galaxy (Oh et al., 2008). The distribution can be derived by  $\rho \sim R^\alpha$ , where  $\alpha < 0$ . The ISO density profile is given by:

$$\rho_{\text{ISO}}(R) = \rho_o \left[1 + \left(\frac{R}{R_c}\right)^2\right]^{-1}, \quad (29)$$

where  $\rho_o$  is the halo central density, and  $R_c$  is the core radius of the halo. The corresponding ISO halo rotation velocity is given by:

$$V_{\text{ISO}}(R) = \sqrt{4\pi G \rho_o R_c^2 \left[1 - (R_c/R) \text{atan}(R/R_c)\right]}, \quad (30)$$

These two halo models have been previously used in different analyses. De Blok et al. (2008) used the NFW and ISO halo models in their analysis to check the distribution of dark matter in the THINGS galaxies. The ISO halo model is used in most cases than the NFW halo model because it gives quality results of the fit, meaning that it gives lower chi-square ( $\chi^2$ ) values as compared to the NFW halo model (Oh et al., 2015). Based on this reason and other reasons in the literature, we preferred to use the ISO halo model to model the dark matter distribution of IC 4710.

## 4.8 Mass models

To derive the ISO halo density profile using Eqn. 29, values for  $\rho_o$  and  $R_c$  are required. We firstly assumed a set of 200 equally spaced values for  $\rho_o$  starting from  $10^{-3} M_\odot \text{pc}^{-3}$  to  $1 M_\odot \text{pc}^{-3}$ . Also a set of 200 equally spaced values for  $R_c$  starting from 0.1 kpc to 3.5 kpc was assumed. We looked at different studies

(Oh et al., 2015; De Blok et al., 2008) to get an idea of the range of values to use for  $\rho_o$ .

We used the assumed 200 sets of values for  $\rho_o$  and  $R_c$  to construct the dark matter velocity curves through Eqn. 30. Then we calculated the corresponding rotation curves by adding the stellar and gas rotation curves together. For each total rotation curve, we then subtracted it from the rotation curve given by 3D BAROLO, in order to calculate the residual ( $\chi^2$ ) and use that to determine the most likely values for  $\rho_o$  and  $R_c$  which are given in Table 2.

We used three different stellar mass-to-light ratios, as mentioned in section 4.7.2. As we can see, this galaxy lacks gas in the centre, which may have been due to supernovae that would heat up the surrounding gas and prevent star formation, from the previous chapter exploring the energetics. The assumed mass-to-light ratios are given in Table 2. We constructed the ISO density profiles using Eqn. 29, and the profiles are presented in Fig. 46.

Table 2: Parameters of dark matter in IC 4710.

M/L ( $M_\odot/L_\odot$ )	$\rho_o$ ( $M_\odot$ $pc^{-3}$ )	$R_c$ (kpc)	$\chi^2$ ( $km\ s^{-1}$ )
0.1	0.21	0.043	0.76
0.2	0.20	0.040	0.78
0.3	0.19	0.037	0.79



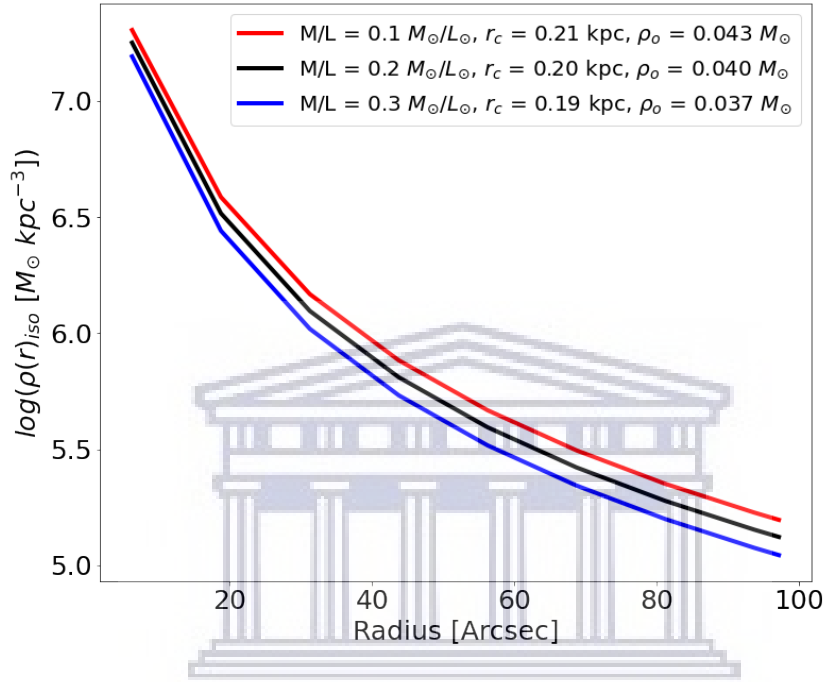


Figure 46: The pseudo isothermal sphere density profile of IC 4710 assuming stellar mass-to-light ratios of  $0.1 M_{\odot}/L_{\odot}$ ,  $0.2 M_{\odot}/L_{\odot}$ , and  $0.3 M_{\odot}/L_{\odot}$ . The halo central density and core radius are shown on the plots.

The three ISO density profiles (presented above) have a shallow shape. Oh et al. (2015) mentioned that most dwarf galaxies have shallower dark matter density profiles, especially at lower radii. They further mentioned that the shallower dark matter density profiles usually result from gas outflows driven by supernovae. We used the ISO density profiles to derive the ISO rotation curves through Eqn. 30, presented in Fig. 47, Fig. 48, and Fig. 49. The three figures present all the rotation curves of the mass components derived, i.e., the stellar rotation curve, gas rotation curve, dark matter rotation curve, total rotation curve, and the observed rotation curve.

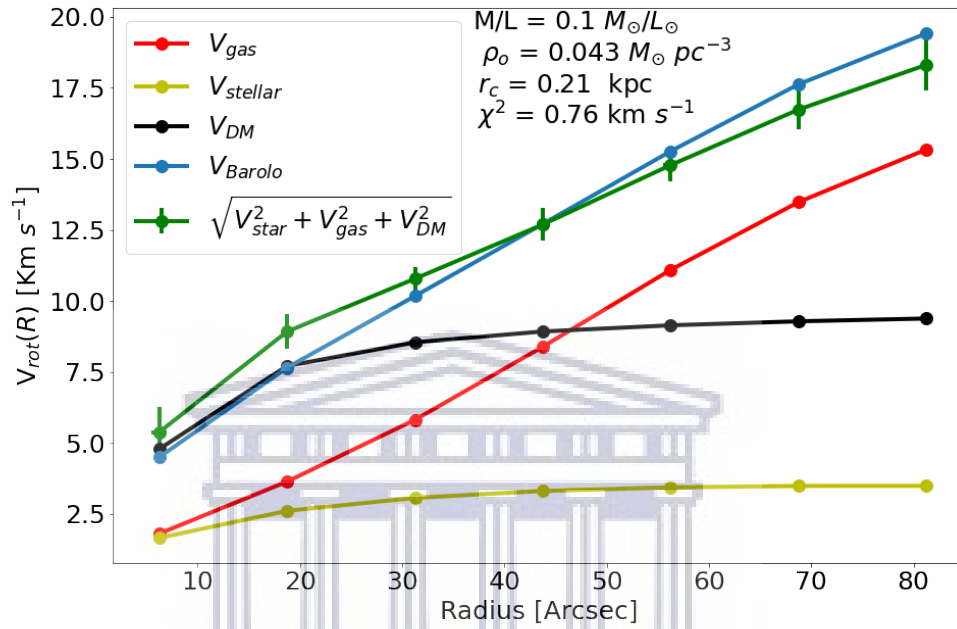


Figure 47: The rotation curves for IC 4710 assuming stellar  $M/L = 0.1 M_{\odot}/L_{\odot}$ . All the rotation curves are labelled at the top right corner. The parameters are also given on the figure. At innermost radii there is more dark matter than baryons, while at larger radii gas is more than the stellar component and dark matter component. Dark matter dominates the stars at all radii. The observed rotation curves match with the total rotation curve.

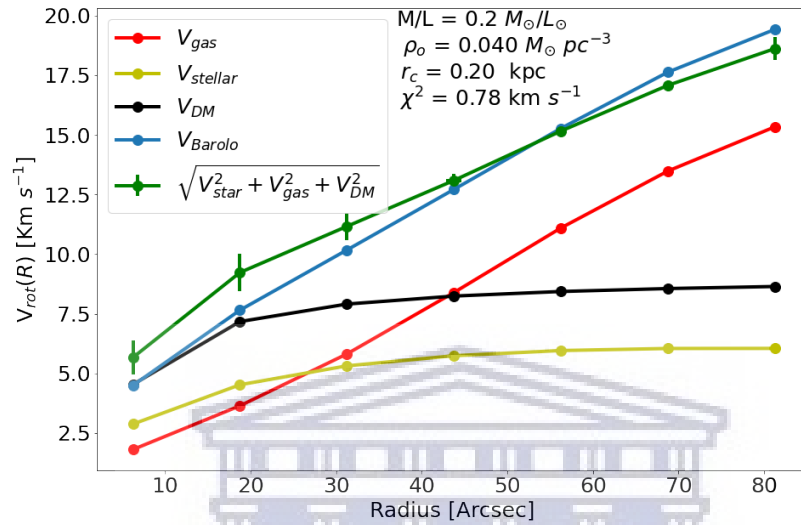


Figure 48: The rotation curves for IC 4710 assuming stellar  $M/L = 0.2 M_{\odot}/L_{\odot}$ . All the rotation curves are labelled at the top right corner. The parameters are also given on the figure. At innermost radii there are more stars than gas, while at larger radii gas is more than the stellar component and dark matter component. Dark matter dominates the stars at all radii. The observed rotation curves match with the total rotation curve.

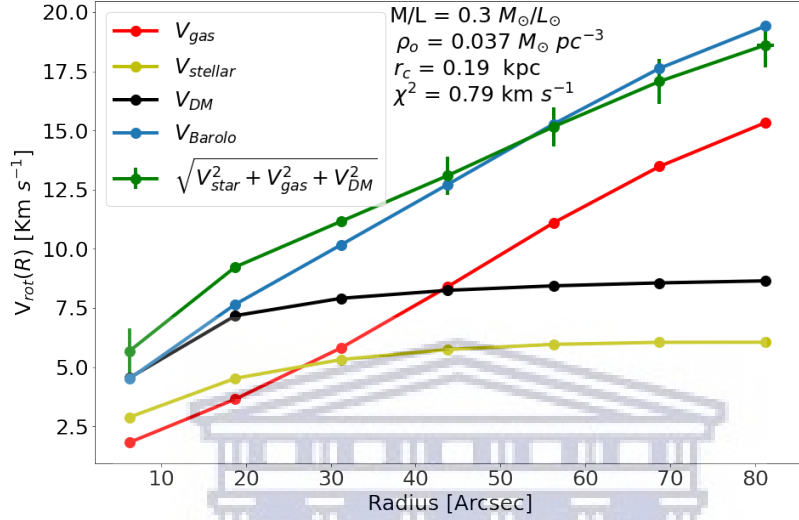


Figure 49: The rotation curves for IC 4710 assuming stellar  $M/L = 0.3 M_{\odot}/L_{\odot}$ . All the rotation curves are labelled at the top right corner. The parameters are also given in the figure. At innermost radii, there are more stars than gas, while at larger radii the gas component dominates compared to the stellar and dark matter components. Dark matter dominates the stars at all radii. The observed rotation curves match the total rotation curve.

The presented rotation curves in Fig. 47, Fig. 48, and Fig. 49 are the best fit cases. The observed rotation curve matches very well with the total rotation curve for each mass-to-light ratio. At the innermost radii, the summed curve is too high due to the stellar contributions; therefore, this means that stars dominate the gravitational potential at inner radii.

Comparing the three best fits with each other, the model assuming a stellar mass-to-light ratio of  $0.3 M_{\odot}/L_{\odot}$  in Fig. 49 does not produce as good a match to the modeled rotation curve as those with lower mass-to-light ratios. This means that this model assumes too much stellar mass in the galaxy, so this

galaxy seems to have a lower mass-to-light ratio than other dwarf galaxies. While we note that the parameter values used to obtain Fig. 47 and Fig. 48 are not equal (values given on each mentioned figure), their results seem to be almost the same. The difference between Fig. 47 and Fig. 48 is that in Fig. 48 we have more stars than gas at innermost radii while in Fig. 47 we have more gas than stars at all radii. But mass-to-light ratio of  $0.1 M_{\odot}/L_{\odot}$  (Fig. 47) gives the best results since the  $\chi^2$  is very small ( $0.76 \text{ km s}^{-1}$ ) as compared to Fig. 48 ( $\chi^2 = 0.78 \text{ km s}^{-1}$ ). But the mass-to-light ratio of  $0.2 M_{\odot}/L_{\odot}$  (Fig. 48) also appears to be viable, and does a better job with the innermost radii as well.

Analysing Fig. 48, we see the stars to be more dominant than gas at lower radii up to a radius of  $\sim 25$  arcsec and then become less dominant than gas for the rest of the radius. The stars are less dominant than the dark matter at all radii. Gas increases from innermost radii to outermost radii, which implies that there is more gas at larger radii than at smaller radii. This is in good agreement with Fig. 16 (HI total intensity map), which shows that there is HI depression at smaller radii and a peak of HI content at a radius of 3.5 kpc. Dark matter is more dominant than baryons from the centre of the galaxy up to the radius of  $\sim 43$  arcsec, where it becomes higher than the stars but lesser than the gas. This agrees well with Fig. 16 which shows greater HI content at larger radii. Dark matter is also the second biggest contributor to the summed rotation curve.

Analysing Fig. 47, we see the stars to be less dominant than gas and dark matter at all radii. Gas increases from innermost radii to outermost radii, which implies that there is more gas at larger radii than at smaller radii. Dark matter is more dominant than baryons from the centre of the galaxy up to the radius of  $\sim 43$  arcsec where it becomes higher than the stars but lesser than the gas.

We used our best-fitting dark matter density profiles to calculate the total amount of dark matter for each of the mass-to-light ratio cases:

- When mass-to-light ratio is  $0.1 M_{\odot}/L_{\odot}$ , dark matter mass is  $1.03 \times 10^8 M_{\odot}$ .
- When mass-to-light ratio is  $0.2 M_{\odot}/L_{\odot}$ , dark matter mass is  $8.73 \times 10^7 M_{\odot}$ .
- When mass-to-light ratio is  $0.3 M_{\odot}/L_{\odot}$ , dark matter mass is  $7.28 \times 10^7 M_{\odot}$ .

We find higher dark matter mass for lower stellar mass-to-light ratio assumptions. In Chapter 2, we obtained a total dark matter mass of  $M_{\text{DM}} = 2.96 \times 10^8 M_{\odot}$ , which was lower than the baryonic mass. In this chapter, we performed much more detailed mass modelling and found that the dark matter mass is even further diminished, although it is still a significant part of the galaxy (see following discussion).

It is known that dwarf galaxies are dark matter dominated than other types of galaxies (Roberts et al., 1994), but it appears that baryons dominate our galaxy. We determined the ratio of the dark matter mass to the baryonic mass for comparison. The following equation from De Blok et al. (2008) when subtracted from 1, it gives the ratio of the dark matter mass to the baryonic mass:

$$\frac{M_{\text{baryons}}}{M_{\text{tot}}} = \frac{V_{\text{gas}}^2 + \Upsilon_{\text{stellar}} V_{\text{stellar}}^2}{V_{\text{obs}}^2}. \quad (31)$$

where  $M_{\text{baryons}}/M_{\text{tot}}$  shows the degree of how much dark matter is dominating,  $\Upsilon V_{\text{stellar}}$  presents the stellar rotation velocities,  $V_{\text{gas}}$  presents the gas rotation velocities, and  $V_{\text{obs}}$  presents the observed velocities from <sup>3D</sup>BAROLO. This ratio calculation is done for the three mass-to-light ratios used for the stellar component, and the results are shown below:

- When the stellar mass-to-light ratio is  $0.1 M_{\odot}/L_{\odot}$ , the ratio of the dark matter to the baryons is 0.33.

- When the stellar mass-to-light ratio is  $0.2 M_{\odot}/L_{\odot}$ , the ratio of the dark matter to the baryons is 0.28.
- When the stellar mass-to-light ratio is  $0.3 M_{\odot}/L_{\odot}$ , the ratio of the dark matter to the baryons is 0.23.

Since  $M_{\text{baryons}}/M_{\text{tot}}$  shows the degree of how much dark matter is dominating, then from these results, we see the ratio decreases with increasing stellar mass-to-light ratio. This means that at a low mass-to-light ratio, we have more dark matter than baryons, and at a high mass-to-light ratio, we have more baryons than dark matter. In all cases, our galaxy is dominated by baryons.

#### 4.9 Comparison to literature

The core radius ( $r_c$ ) and the central density ( $\rho_o$ ) used to determine the ISO halo model were compared to the values from the literature in Fig. 50 for all three stellar mass-to-light ratios assumed.

These results were compared to the results from [Oh et al. \(2015\)](#), [De Blok et al. \(2008\)](#), and [Swaters et al. \(2011\)](#). [Oh et al. \(2015\)](#) used a sample of 26 dwarf galaxies from LITTLE THINGS. [De Blok et al. \(2008\)](#) used a sample of 19 galaxies from THINGS, which consists of dwarf galaxies and spiral galaxies but we compared our results to their results of dwarf galaxies. [Swaters et al. \(2011\)](#) used a Westerbork HI Survey of Spiral and Irregular Galaxies (WHISP) sample of 18 late-type dwarf and low surface brightness galaxies.

By analysing Fig. 50 which presents the comparisons, this galaxy IC 4710 seems to fall within a similar range of  $\rho_o$  and  $r_c$  of other dwarf galaxies in literature. Our galaxy is in good agreement with other dwarf galaxies from the literature.

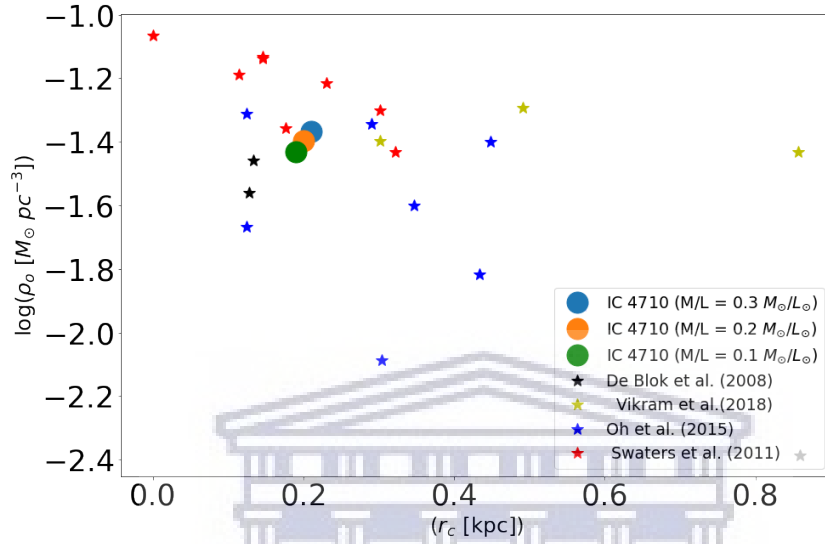


Figure 50: The comparison of the best fit values of  $\rho_0$  and  $r_c$  for mass-to-light ratio of (0.1, 0.2, 0.3)  $M_\odot/L_\odot$ . Every star symbol represents a dwarf galaxy from labelled literatures (De Blok et al., 2008; Vikram et al., 2018; Oh et al., 2015; Swaters et al., 2011). Our galaxy IC 4710 is presented in green, orange, and blue dots.



## Chapter 5

### Summary

This work aimed to model the dynamics of the nearby (7.38 Mpc) dwarf galaxy IC 4710. We used the HI line data cube from ATCA. The resolution of the data cube is  $26.9 \text{ arcsec} \times 25.7 \text{ arcsec}$  with a pixel scale of  $2.5 \text{ arcsec}$  and the velocity width of  $3.5 \text{ km s}^{-1}$ .

We derived the HI data products such as the channel maps, HI total intensity map, HI intensity weighted mean velocity field map, velocity dispersion map, and the HI global profile. Data was masked using the standard deviation ( $\sigma = 0.909 \text{ mJy beam}^{-1}$ ) of the noise in the line-free channel. The noise from the line-free channel was found to be Gaussian distributed. The inclination angle of  $i = 37.6$  degrees was obtained from the HI total intensity map. We adopted the distance of  $D = 7.38 \pm 0.1 \text{ Mpc}$  from [Tully et al. \(2013a\)](#) and used it together with the HI total intensity map to calculate the total HI mass of  $M_{\text{HI}} = 2.98 \pm 0.01 \times 10^8 M_{\odot}$ . We observed a clear HI depression at the center of IC 4710 from the total HI intensity map, where the surface density is around  $3 M_{\odot} \text{ pc}^{-2}$ . We noted the galaxy to be rotating from analysing the HI intensity weighted mean velocity field map. From the velocity dispersion map, we were able to see that the HI depression has a velocity dispersion of about  $7 \text{ km s}^{-1}$ .

We obtained the widths of the HI spectrum at the levels of 20% and 50% of the peak flux density from the HI global profile to be  $W_{20} = 45 \text{ km s}^{-1}$  and  $W_{50} = 30 \text{ km s}^{-1}$ . We obtained the systemic velocity of  $V_{\text{sys}} = 737 \pm 2.9 \text{ km s}^{-1}$  from the HI global profile. By using  $W_{50}$  and the inclination angle we were able to calculate the maximum velocity of  $V_{\text{max}} = 24.6 \pm 0.1 \text{ km s}^{-1}$ .  $V_{\text{max}}$  was then used in Newton's laws to calculate the dynamical mass of  $M_{\text{total}} = 6.1 \pm 0.02 \times 10^8 M_{\odot}$ .

We adopted a far-infrared surface brightness of  $L_* = 10^{8.16} L_\odot$  from [Smith et al. \(2007\)](#) and assumed the mass-to-light ratio of  $0.1 M_\odot/L_\odot$  to obtain the stellar mass of  $M_* = 1.45 \pm 0.02 \times 10^7 M_\odot$ . We could not find any NIR measurements, but FIR also traces stellar mass. We subtracted the HI mass and the stellar mass from the dynamical mass to obtain the dark matter mass of  $M_{\text{DM}} = 2.96 \pm 0.01 \times 10^8 M_\odot$ . We compared the dark matter mass and the baryonic mass to the dynamical mass. We found that  $M_{\text{DM}} = 48.7\%$  of the total mass of the system,  $M_* = 2.4\%$  of the total mass of the system, and  $M_{\text{HI}} = 48.9\%$  of the total mass of the system, this means that the galaxy contains almost equal amounts of baryons and dark matter. We compared IC 4710 to literature through HI mass-size and baryonic Tully-Fisher relations and found that IC 4710 is in good agreement with other dwarf galaxies.

We studied the central energetics of the galaxy IC 4710 using the HI observations to further investigate the observed clear HI depression at the centre of the galaxy. We used the HI total intensity map to obtain the mass that would have been removed from the inner region, and we found it to be  $M_{\text{inner}} = 1.67 \times 10^7 M_\odot$ . We used the inner mass together with the assumed expansion velocity of  $30 \text{ km s}^{-1}$  and obtained the kinetic energy of the expanding gas to be  $E_K = 3.7 \times 10^{45} \text{ J}$ . Using this kinetic energy and the guidelines from [Chu \(2005\)](#) and [Mori et al. \(2002\)](#), we found that IC 4710 requires  $\sim 95$  supernovae to account for the kinetic energy of the HI that could have been removed from the centre.

We adopted the mean star formation rate surface density of  $10^{-2.823} M_\odot \text{ year}^{-1} \text{ kpc}^{-2}$  from [Calzetti et al. \(2010\)](#) and used it to derive the total SFR of  $0.06 M_\odot \text{ year}^{-1}$  and the supernovae rate of  $0.0006 M_\odot \text{ year}^{-1}$ . We assumed that every SN-II has a mass of  $8 M_\odot$ , then 95 supernovae will have a mass of  $760 M_\odot$ . The mass and the supernova rate gave us a timescale of  $t = 1.31 \times 10^6$  years. This timescale means stars were likely responsible for the HI kinematics at the center of the galaxy as they act as the source of mechanical energy. We also analysed the B-band optical image of IC 4710 taken by the CTIO 1.5m

telescope and observed the young stars at the galaxy's center. It then meant that stars have removed the gas at the center. We used the  $V_{\max}$  to calculate the escape velocity of  $\sim 45 \text{ km s}^{-1}$  where the maximum radius of  $R_{\max} = 8.7$  kpc was adopted from [Elson et al. \(2011b\)](#).

The global kinematics of the dwarf galaxy IC 4710 were studied by using ATCA imaging to generate a model for the rotation curve of the system. The study of gas kinematics helps in understanding the dynamical structure and distribution of matter in disk galaxies. To obtain the rotation curve of IC 4710, we fitted the tilted ring model to the velocity field. The technique of fitting the tilted ring model was performed using <sup>3D</sup>BAROLO. The estimated initial dynamical central points ( $X_o, Y_o$ ) were obtained from displaying the data cube in kvis software, where  $X_o = 126$  pixels and  $Y_o = 123$  pixels. The initial estimate of the systemic velocity ( $V_{\text{sys}} = 737 \text{ km s}^{-1}$ ) was obtained from the HI global profile of the galaxy presented in Chapter 2. The inclination angle  $i$  was estimated to be 30 degrees from fitting an ellipse to the HI total intensity map, and used to determine the rotation velocity  $V_{\text{rot}} = 45 \text{ km s}^{-1}$ , where  $W_{50}$  is the width of the HI spectrum at a level of 50% obtained in Chapter 2. This rotation velocity ( $45 \text{ km s}^{-1}$ ) was also used as an initial estimate. The position angle ( $PA = 45$  degrees) was assumed from displaying the data cube in kvis software.

Six iterations were done to fit the tilted-ring model. The initial iteration had all parameters left as free, and the following five iterations additionally fixed the central dynamical points, the systemic velocity, the radial velocity, the position angle, and the inclination angle, respectively. The final tilted-ring model was then obtained. The obtained rotation curve rises steeply until it reaches the maximum rotation velocity of  $24.6 \text{ km s}^{-1}$  and at a radius of 100 arcsec. This maximum rotation velocity is greater than the maximum velocity ( $24.6 \text{ km s}^{-1}$ ) that was estimated from  $W_{50}$  in Chapter 2. After the maximum point, the rotation velocities decrease.

To check for the accuracy of the obtained dynamical model, we compared the model data to the input data. The comparison was performed by superimposing the model data contours and the ATCA data contours on the <sup>3D</sup>BAROLO model channel maps. We observed a good agreement between the model and the data. We then compared the dynamical model to the data through the derivation of residuals presented in histograms. When analysing the histograms, we noticed that each case is slightly skewed to the positive values, which would mean that the model slightly understands the HI content or they are in good agreement (as residual is data-model) but not to a significant degree. This means that the obtained comparison results are reliable. We further checked the accuracy by plotting the standard deviation of noise in each channel as a function of channel number. We found that the shape of this relation indicates a roughly constant standard deviation, which implies that the model and data are in good agreement. We applied the asymmetric drift correction to the observed rotation velocities to derive the circular velocities assuming the dispersion velocity to be  $8 \text{ km s}^{-1}$ , which improved our rotation curve.

Mass modeling of IC 4710 was performed. To derive the distributions of dark matter, we needed to take into account the contributions from the gas component and the stellar component. To model the gas contributions, we used the <sup>3D</sup>BAROLO's measure of the azimuthally averaged gas surface densities in IC 4710 to calculate the cumulated mass as a function of radius ( $R_{\text{min}} = 0$  and  $R_{\text{max}} = 3.5 \text{ kpc}$ ). The gas surface density profile and the cumulative gas mass profile were obtained. Knowing the mass within a particular radius, Newton's laws were used to calculate the rotation velocities of the gas, and the gas rotation curve was obtained. To model the stellar contributions, we adopted the far-infrared surface brightness ( $L_* = 10^{8.16} L_{\odot}$ ) of the galaxy from [Smith et al. \(2007\)](#) and assumed three stellar mass-to-light ratios (0.1, 0.2 and 0.3  $M_{\odot}/L_{\odot}$ ) to derive the stellar rotation velocities. We obtained the mass profiles through Eqn. 24, the stellar masses were then used to calculate the three central

surface brightness profiles using Eqn. 25 where we adopted the scale length in i-band from [Ryder et al. \(1994\)](#). The central surface brightness profiles were used to derive the three stellar surface density profiles. We used the stellar surface density profiles to derive the cumulative mass within a radius R. These cumulative stellar mass curves were then converted into rotation velocities using Eqn. 23, and the corresponding rotation curves are plotted.

We derived the total rotation curve - the sum of all three contributions - and compared it to the observed rotation curve to model the dark matter contribution. In this work, we used the ISO halo model to model the dark distribution of IC 4710. To derive the ISO halo density profile using Eqn. 29, values for  $\rho_0$  and  $R_c$  are required. We looked at different studies ([Oh et al. \(2015\)](#); [De Blok et al. \(2008\)](#)) to get an idea of the range of values to use for  $\rho_0$ , and  $R_c$  is related to the HI radius for this galaxy. We calculated the corresponding rotation curves by adding the stellar and gas rotation curves together. For each total rotation curve, we then subtracted it from the rotation curve given by <sup>3D</sup>BAROLO to calculate the residual ( $\chi^2$ ) and use that to determine the most likely values for  $\rho_0$  and  $R_c$  which are given in Table 2. We used three assumed mass-to-light ratios and constructed the ISO density profiles using Eqn. 29. We used the ISO density profiles to derive the ISO rotation curves and corresponding best-fit total rotation curves. The observed rotation curve matches very well with the total rotation curve for each mass-to-light ratio. At the innermost radii, the summed total curve is too high due to the stellar contributions; therefore, this means that there are too many stars at the center for our model. This confirms our findings in the energetics section. The assumed mass-to-light ratio of  $0.1 M_\odot/L_\odot$  gives the best results since the  $\chi^2$  is very small ( $1.55 \text{ km s}^{-1}$ ). The mass-to-light ratio of  $0.2 M_\odot/L_\odot$  also appears to be viable and does a better job with the innermost radii as well.

We calculated the dark matter mass for each mass-to-light ratio and found that the lower the mass-to-light ratio, the higher the dark matter mass. Comparing

these results to the results obtained in Chapter 2, we found that the dark matter mass is lower in IC 4710, although it is still a significant part of the galaxy. We determined the ratio of the dark matter mass to the baryonic mass (see Eqn. 31) for comparison. This was done to check whether our galaxy is dark matter-dominated or is dominated by baryons. From the results, the ratio decreases with the increasing mass-to-light ratio. So these results show that we have less dark matter than baryons for each mass-to-light ratio, which means baryons dominate IC 4710, unusual for dwarf galaxies. We compared our results to literature using the core radius ( $R_c$ ), and the central density ( $\rho_o$ ) used to determine the ISO halo model. These results were compared to the results from [Oh et al. \(2015\)](#), [De Blok et al. \(2008\)](#), and [Swaters et al. \(2011\)](#). Galaxy IC 4710 seems to fall within a similar range of  $\rho_o$  and  $R_c$  of other dwarf galaxies in literature. So this means that our galaxy modeling is in good agreement with that performed for other dwarf galaxies from the literature.



## Future Work and Conclusion

Neutral hydrogen (HI) is a gas found everywhere that helps in tracing large-scale structures in the Universe, and it helps in studying the physical and dynamical processes occurring in galaxies (Duffy et al., 2012). There are different HI surveys, and currently, there is a new Australian Square Kilometre Array Pathfinder (ASKAP) HI survey known as Widefield ASKAP L-band Legacy All-sky Blind survey (WALLABY), which is a shallow HI All-sky survey (Taylor et al., 2008). ASKAP is a next-generation radio telescope being built in Western Australia (Koribalski et al., 2020).

WALLABY is an extragalactic HI survey which will observe  $\sim 75\%$  of the sky at a redshift of  $z = 0.26$  (Duffy et al., 2012). WALLABY will observe all of the southern sky and part of the northern sky ( $\delta < +30^\circ$ ; Koribalski et al., 2020). WALLABY aims to analyze the properties, large-scale distribution of gas-rich galaxies, formation and evolution of galaxies, star formation in galaxies, mergers, and interactions between galaxies, etc. WALLABY will also assist in studying cosmological parameters (Taylor et al., 2008).

Staveley-Smith (2009) mentioned that about 500 000 galaxies would be detected at an assured angular resolution of 30 arcsec. Duffy et al. (2012) presented the predictions about WALLABY that it will manage to find  $\sim 6 \times 10^5$  galaxies which is about two orders of magnitude greater than the HI survey all-sky surveys that are already being used. They also found that WALLABY will be able to detect galaxies with HI mass  $\gtrsim 10^{8.5} M_\odot$  and stellar mass from  $10^5 M_\odot$  to  $10^{12} M_\odot$ , which indicate to be dwarf galaxies. The full ASKAP configuration of 36 antennas with a baseline  $\sim 6$  km is required to obtain a high angular resolution of 10 arcsec (Duffy et al., 2012). The ASKAP baselines are comparable to the maximum ATCA baselines of  $\sim 6$  km (Tingay et al., 2003). Many of the dwarf galaxies detected by WALLABY can be modeled the same way we have modeled IC 4710, and this will allow us to study the properties of

dwarf galaxies statistically.

MIGHTEE is one of the big survey projects of MeerKAT (Jarvis et al., 2017; Delhaize et al., 2021). MeerKAT is the SKA precursor array operated by the South African Radio Astronomy Observatory (SARAO), and it consists of 64 antennae, each dish having a diameter of 13.5 m (Beck et al., 2021). MIGHTEE will cover an area of 20 deg<sup>2</sup>, and it will focus on radio continuum, spectral line, and polarisation (Paul et al., 2021; Delhaize et al., 2021). MIGHTEE will be able to observe the sky at redshift  $z \sim 6$  (Jarvis et al., 2017). MIGHTEE is designed to detect low mass galaxies, and it is expected to detect  $\sim 50$  galaxies with  $M_{\text{HI}} < 10^8 M_{\odot}$ , and  $\sim 250$  galaxies with  $M_{\text{HI}} = 10^8 - 10^9 M_{\odot}$  (Maddox et al., 2021). MIGHTEE is designed to assist in studying the evolution of Active Galactic Nuclei (AGN), the evolution of HI in the Universe, the cosmic magnetic fields, and will be able to measure the star formation rate (Jarvis et al., 2017). MIGHTEE will be the first survey to investigate the distribution of dark matter and luminous matter in massive galaxies (Jarvis et al., 2017). MIGHTEE has the HI emission project called the MIGHTEE-HI (Maddox et al., 2021).

The MIGHTEE-HI will cover an area of 32 deg<sup>2</sup>, but it has higher sensitivity, higher redshift, and better resolution (Maddox et al., 2021). MIGHTEE-HI will be able to observe the sky at redshift  $z = 0$  to  $z = 0.58$  with an angular resolution of 6 arcsec (Jarvis et al., 2017). Maddox et al. (2021) presents results of galaxy NGC 895, which they used data from MIGHTEE-HI and they modeled it using <sup>3D</sup>BAROLO, which is the same way we modeled IC 4710. MIGHTEE-HI will help in studying the statistical properties of the Tully-Fisher relation at different wavelengths (Maddox et al., 2021). This survey will allow us to study the HI content in low-mass galaxies as a function of cosmic time (Maddox et al., 2021). The survey will also help in tracing the dark matter distribution in dwarf galaxies. The resolution of MIGHTEE does not allow it to measure the morphology of galaxies. While WALLABY will find more dwarf galaxies, MIGHTEE will have a greater sensitivity and be able to tell us more detail



about the dwarf galaxies it finds. Both approaches are important for studying this population of galaxies through HI emission, like we did for IC 4710.



UNIVERSITY *of the*  
WESTERN CAPE

## References

- Abraham R. G., van den Bergh S., et al., 2001, *Science*, 293, 1273
- Al-Baidhany I. A., Chiad S. S., Jabbar W. A., Habubi N. F., Abass K. H., 2020, *NeuroQuantology*, 18, 76
- Beck G., Kumar M., Malwa E., Mellado B., Temo R., 2021, arXiv preprint arXiv:2102.10596
- Begeman K., et al., 1989, *Astronomy and Astrophysics*, 223, 47
- Begeman K., Broeils A., Sanders R., et al., 1991, *Monthly Notices of the Royal Astronomical Society*, 249, 523
- Bottinelli L., Gouguenheim L., Paturel G., De Vaucouleurs G., 1983, *Astronomy and Astrophysics*, 118, 4
- Broeils A. H., Rhee M.-H., 1997, *Astronomy and Astrophysics*, 324, 877
- Calzetti D., et al., 2010, *The Astrophysical Journal*, 714, 1256
- Carignan C., Côté S., Freeman K., Quinn P., 1997, arXiv preprint astro-ph/9704032
- Catinella B., Giovanelli R., Haynes M. P., 2006, *The Astrophysical Journal*, 640, 751
- Chavanis P.-H., et al., 2012, *Astronomy & Astrophysics*, 537, A127
- Chu Y.-H., 2005, in *Extra-Planar Gas*. p. 297
- Corbelli E., Schneider S. E., 1997, *The Astrophysical Journal*, 479, 244
- Daigle O., Carignan C., Amram P., Hernandez O., Chemin L., Balkowski C., Kennicutt R., 2006, *Monthly Notices of the Royal Astronomical Society*, 367, 469
- Dale D. A., et al., 2017, *The Astrophysical Journal*, 837, 90

- De Blok W., McGaugh S. S., Rubin V. C., 2001, *The Astronomical Journal*, 122, 2396
- De Blok W., Walter F., Brinks E., Trachternach C., Oh S., Kennicutt Jr R., 2008, *The Astronomical Journal*, 136, 2648
- De Blok W., et al., 2010, *Advances in Astronomy*, 2010
- De Naray R. K., McGaugh S. S., De Blok W., 2008, *The Astrophysical Journal*, 676, 920
- Dekel A., Silk J., et al., 1986, *The Astrophysical Journal*, 303, 39
- Delhaize J., et al., 2021, *Monthly Notices of the Royal Astronomical Society*, 501, 3833
- Duffy A. R., Meyer M. J., Staveley-Smith L., Bernyk M., Croton D. J., Koribalski B. S., Gerstmann D., Westerlund S., 2012, *Monthly Notices of the Royal Astronomical Society*, 426, 3385
- Elson E., De Blok W., Kraan-Korteweg R., 2011a, *Monthly Notices of the Royal Astronomical Society*, 415, 323
- Elson E., De Blok W., Kraan-Korteweg R., et al., 2011b, *Monthly Notices of the Royal Astronomical Society*, 415, 323
- Fraternali F., Binney J., 2006, *Monthly Notices of the Royal Astronomical Society*, 366, 449
- Gallagher J. S., Hunter D. A., et al., 1984, *Annual review of astronomy and astrophysics*, 22, 37
- Geha M., Blanton M., Masjedi M., West A., 2006, *The Astrophysical Journal*, 653, 240
- Gerola H., Seiden P. E., Schulman L. S., 1980, *The Astrophysical Journal*, 242, 517

- Glowacki M., Elson E., Davé R., 2020, Monthly Notices of the Royal Astronomical Society, 498, 3687
- Gnedin O. Y., Zhao H., et al., 2002, Monthly Notices of the Royal Astronomical Society, 333, 299
- Golubov O., et al., 2013, Astronomy & Astrophysics, 557, A92
- Gooch R., 1995, in Astronomical Data Analysis Software and Systems IV. p. 144
- Governato F., et al., 2010, nature, 463, 203
- Grebel E. K., 2001, The Evolution of Galaxies, pp 231–239
- Gutiérrez C., Azzaro M., Prada F., 2002, The Astrophysical Journal Supplement Series, 141, 61
- Heald G., et al., 2011, Astronomy & astrophysics, 526, A118
- Henry J. P., Briel U. G., Böhringer H., 1998, Scientific American, 279, 52
- Higdon S., Higdon J., Marshall J., 2006, The Astrophysical Journal, 640, 768
- Hodge P. W., et al., 1971, Annual Review of Astronomy and Astrophysics, 9, 35
- Hubble E. P., et al., 1926, The Astrophysical Journal, 64
- Hunt L. K., Tortora C., Ginolfi M., Schneider R., 2020, Astronomy & Astrophysics, 643, A180
- Ibata R. A., et al., 2013, Nature, 493, 62
- Iorio G., Fraternali F., Nipoti C., Di Teodoro E., Read J. I., Battaglia G., 2016, Monthly Notices of the Royal Astronomical Society, 466, 4159
- Jarvis M. J., et al., 2017, arXiv preprint arXiv:1709.01901
- Kamada A., Kaplinghat M., Pace A. B., Yu H.-B., 2017, Physical review letters, 119, 111102

- Karachentsev I. D., Kaisina E. I., Kashibadze O. G., 2016, *The Astronomical Journal*, 153, 6
- Karachentsev I., Riepe P., Zilch T., 2020, arXiv preprint arXiv:2001.03005
- Koribalski B. S., et al., 2020, *Astrophysics and Space Science*, 365, 1
- Kormendy J., Bender R., et al., 1996, *The Astrophysical Journal Letters*, 464, L119
- Kourkchi E., Courtois H. M., Graziani R., Hoffman Y., Pomarède D., Shaya E. J., Tully R. B., 2020, *The Astronomical Journal*, 159, 67
- Lee J. C., et al., 2009, *The Astrophysical Journal*, 706, 599
- Lelli F., McGaugh S. S., Schombert J. M., 2016, *The Astrophysical Journal Letters*, 816, L14
- Lelli F., McGaugh S. S., Schombert J. M., Desmond H., Katz H., 2019, *Monthly Notices of the Royal Astronomical Society*, 484, 3267
- Lin D., Faber S., et al., 1983, *The American Astronomical Society*, 266, L21
- Mac Low M.-M., Ferrara A., et al., 1999, *The Astrophysical Journal*, 513, 142
- Maddox N., et al., 2021, *Astronomy & Astrophysics*, 646, A35
- Martin C. L., et al., 1996, arXiv preprint astro-ph/9601107
- Martin C. L., et al., 1998, *The Astrophysical Journal*, 506, 222
- Mateo M., et al., 1998, *Annual Review of Astronomy and Astrophysics*, 36, 435
- Metropolis N., Ulam S., 1949, *Journal of the American statistical association*, 44, 335
- Meurer G. R., Carignan C., Beaulieu S., Freeman K. C., 1996, arXiv preprint astro-ph/9601191
- Moore B., et al., 1994, arXiv preprint astro-ph/9402009

- Mori M., Ferrara A., Madau P., 2002, *The Astrophysical Journal*, 571, 40
- Moustakas J., Kennicutt Jr R. C., Tremonti C. A., Dale D. A., Smith J.-D. T., Calzetti D., 2010, *The Astrophysical Journal Supplement Series*, 190, 233
- Navarro J. F., et al., 1996, in *Symposium-international astronomical union*. pp 255–258
- Oh S.-H., De Blok W., Walter F., Brinks E., Kennicutt Jr R. C., 2008, *The Astronomical Journal*, 136, 2761
- Oh S.-H., De Blok W., Brinks E., Walter F., Kennicutt Jr R. C., 2011, *The Astronomical Journal*, 141, 193
- Oh S.-H., et al., 2015, *The Astronomical Journal*, 149, 180
- Ott J., et al., 2012, *The Astronomical Journal*, 144, 123
- Paudel S., Smith R., Yoon S. J., Calderón-Castillo P., Duc P.-A., 2018, *The Astrophysical Journal Supplement Series*, 237, 36
- Paul S., Santos M. G., Townsend J., Jarvis M. J., Maddox N., Collier J. D., Frank B. S., Taylor R., 2021, *Monthly Notices of the Royal Astronomical Society*, 505, 2039
- Peng C. Y., Ho L. C., Impey C. D., Rix H.-W., 2010, *The Astronomical Journal*, 139, 2097
- Roberts M. S., et al., 1969, *The Astronomical Journal*, 74, 859
- Roberts M. S., Haynes M. P., et al., 1994, *Annual Review of Astronomy and Astrophysics*, 32, 115
- Rogstad D., Lockhart I., Wright M., 1974, *The Astrophysical Journal*, 193, 309
- Rubin V. C., Ford Jr W. K., Thonnard N., 1978, *The Astrophysical Journal*, 225, L107

- Ruiz J. E., Santander-Vela J. d. D., Espigares V., Verdes-Montenegro L.,  
Van der Hulst J., 2009, arXiv preprint arXiv:0901.2341
- Ryder S. D., Dopita M. A., et al., 1993, The Astrophysical Journal Supplement  
Series, 88, 415
- Ryder S. D., Dopita M. A., et al., 1994, The Astrophysical Journal, 430, 142
- Saha P., Coles J., Macciò A. V., Williams L. L., 2006, The Astrophysical Journal  
Letters, 650, L17
- Sancisi R., Fraternali F., Oosterloo T., Van Der Hulst T., 2008, The Astronomy  
and Astrophysics Review, 15, 189
- Shapiro P. R., Field G. B., 1976, The Astrophysical Journal, 205, 762
- Simon J. D., 2019, Annual Review of Astronomy and Astrophysics, 57, 375
- Smith B. J., Struck C., Hancock M., Appleton P. N., Charmandaris V., Reach  
W. T., 2007, The Astronomical Journal, 133, 791
- Spitoni E., 2010, EDP Sciences, 514, A73
- Staveley-Smith L., 2009, Panoramic Radio Astronomy: Wide-field 1-2 GHz  
Research on Galaxy Evolution, p. 14
- Steyrleithner P., Hensler G., Boselli A., 2020, Monthly Notices of the Royal  
Astronomical Society, 494, 1114
- Swaters R., Schoenmakers R., Sancisi R., Albada T. v., 1999, Monthly Notices  
of the Royal Astronomical Society, 304, 330
- Swaters R., Sancisi R., Van Albada T., Van Der Hulst J., 2009, Astronomy &  
Astrophysics, 493, 871
- Swaters R., Sancisi R., Van Albada T., Van der Hulst J., 2011, The  
Astrophysical Journal, 729, 118
- Taylor R., et al., 2008, Experimental Astronomy, 22, 151

- Teodoro E. D., Fraternali F., et al., 2015, *Monthly Notices of the Royal Astronomical Society*, 451, 3021
- Tingay S. J., Jauncey D. L., King E. A., Tzioumis A. K., Lovell J. E., Edwards P. G., 2003, *Publications of the Astronomical Society of Japan*, 55, 351
- Tully R. B., et al., 2013a, *The Astronomical Journal*, 146, 86
- Tully R. B., et al., 2013b, *The Astronomical Journal*, 146, 86
- Van Eymeren J., Marcelin M., Koribalski B., Dettmar R.-J., Bomans D., Gach J.-L., Balard P., 2009, *Astronomy & Astrophysics*, 493, 511
- Van der Hulst J., Van Albada T., Sancisi R., 2001, in *Gas and Galaxy Evolution*. p. 451
- Vikram V., Sakstein J., Davis C., Neil A., 2018, *Physical Review D*, 97, 104055
- Walter F., Brinks E., De Blok W., Bigiel F., Kennicutt Jr R. C., Thornley M. D., Leroy A., 2008, *The Astronomical Journal*, 136, 2563
- Wang J., Koribalski B. S., Serra P., van der Hulst T., Roychowdhury S., Kamphuis P., N. Chengalur J., 2016, *Monthly Notices of the Royal Astronomical Society*, 460, 2143
- Weinberg D. H., Szomoru A., Guhathakurta P., Van Gorkom J., 1991, *The Astrophysical Journal*, 372, L13
- Weisz D. R., et al., 2011, *The Astrophysical Journal*, 743, 8
- Woo J., Courteau S., Dekel A., 2008, *Monthly Notices of the Royal Astronomical Society*, 390, 1453